Politecnico di Milano

Dipartimento di Chimica, Materiali e Ingegneria
Chimica "G. Natta"

Doctoral Program in Materials Engineering
Cycle XXXIV

Mechanical Characterization and Modeling of a Novel Continuous Glass Fibers - Polydimethylsiloxane Soft Composite: from Material Preparation to Load Coupling Effects



Candidate
Tiziana Bardelli

Supervisor
Prof. Francesco Briatico Vangosa
Tutor
Prof. Stefano Ettore Romano Turri

Sept 2022

Acknowledgments

In queste poche righe vorrei ringraziare tutte le persone che sono state presenti nella mia vita in questi anni. Ognuna di loro si riconoscerà in queste parole senza che io abbia bisogno di nominarle singolarmente, dai miei professori, ai miei colleghi, dai miei affetti più intimi ai miei familiari, dai miei amici, a tutte le persone che ho incontrato anche solo per un momento ma che, per esserci state, hanno contribuito alla mia crescita. Grazie!

Abstract

This work is a study of the mechanical behavior of a continuous glass fibers - polydimethylsiloxane soft composite. The combination of properly oriented stiff fibers and a highly deformable elastomer leads to the production of laminates that can exhibit an extremely high level of anisotropy and quite large deformation at break. These properties significantly differ from those of traditional rigid matrix composites and can be exploited in many fields such as soft robotics and biomimetic applications. The work starts from the study of the polydimethylsiloxane crosslinking, which knowledge is fundamental to properly impregnate the fibers and control the final properties of the elastomer. The polydimethylsiloxane crosslinking kinetics is studied by comparing a calorimetric approach to a rheological one. The kinetic model obtained allowed, on one hand, to predict the processability window for fibers impregnation and, on the other, to estimate the curing conditions for matrix crosslinking. Furthermore, the influence of the thermal history applied during crosslinking on the final properties of the elastomer is showed. The methods developed for the production of the laminates are described, and the relevant critical aspects discussed. A traditional approach, based on the study of the behavior of unidirectional laminae is then employed to characterize the laminate. Quasi-static tensile tests on unidirectional and symmetric-balanced laminates are performed to evaluate the four independent elastic constants necessary to describe the behavior of a lamina at small strains and micromechanical models are proposed to predict the elastic constants varying the fiber volume fraction. The results are compared with those of typical traditional rigid matrix composites, and the differences are discussed. The peculiar strongly non-linear behavior of symmetric-balanced laminates up to large strain is then studied. Finally, the response of antisymmetric laminates to a uniaxial

load is investigated, and a large extension-twisting coupling is showed and compared with the predictions of classical lamination theory and simple finite element simulations. This work can be considered a solid foundation for the characterization of the behavior of fiber-reinforced elastomers and support the study of more complex models for predicting their behavior.

Sommario

Questo lavoro è uno studio del comportamento meccanico di un composito a di fibre di vetro continue e polidimetilsilossano. La combinazione di fibre rigide opportunamente orientate e di un elastomero altamente deformabile porta alla produzione di laminati che possono presentare un livello di anisotropia estremamente elevato e una deformazione a rottura piuttosto ampia. Queste proprietà differiscono significativamente da quelle dei tradizionali compositi a matrice rigida e possono essere sfruttate in molti campi, come la robotica flessibile e le applicazioni biomimetiche. Il lavoro parte dallo studio della reticolazione del polidimetilsilossano, la cui conoscenza è fondamentale per impregnare correttamente le fibre e controllare le proprietà finali dell'elastomero. La cinetica di reticolazione del polidimetilsilossano è stata studiata confrontando un approccio calorimetrico con uno reologico. Il modello cinetico ottenuto ha permesso da un lato di prevedere la finestra di processabilità per l'impregnazione delle fibre e dall'altro di stimare le condizioni di polimerizzazione per la reticolazione della matrice. Inoltre, è stata mostrata l'influenza della storia termica applicata durante la reticolazione sulle proprietà finali dell'elastomero. Vengono descritti i metodi sviluppati per la produzione dei laminati e vengono discussi gli aspetti critici rilevanti. Un approccio tradizionale, basato sullo studio del comportamento di lamine unidirezionali, è poi impiegato per caratterizzare il laminato. Vengono eseguite prove di trazione quasi statiche su laminati unidirezionali e simmetrico-bilanciati per valutare le quattro costanti elastiche indipendenti necessarie a descrivere il comportamento di una lamina a piccole deformazioni e vengono proposti modelli micromeccanici per prevedere le costanti elastiche al variare della frazione in volume di fibre. I risultati sono confrontati con quelli dei tipici compositi tradizionali a matrice rigida e le differenze sono discusse. Viene poi

studiato il particolare comportamento fortemente non lineare dei laminati simmetrico-bilanciati fino a grandi deformazioni. Infine, viene studiata la risposta dei laminati antisimmetrici a un carico uniassiale e mostrato un forte accoppiamento estensione-torsione che viene confrontato con le previsioni della teoria classica della laminazione e di semplici simulazioni agli elementi finiti. Questo lavoro può essere considerato una solida base per la caratterizzazione del comportamento di elastomeri fibro-rinforzati e supportare lo studio di modelli più complessi per la previsione del loro comportamento.

Contents

Acknowledgments **ii**

Abstract **iii**

Sommario **v**

List of Figures **x**

List of Tables **xx**

1 Introduction **1**
1.1 Background and motivation 1
1.2 Aim and objectives 3
1.3 Structure of the thesis 3

2 Polydimethylsiloxane characterization **6**
2.1 Introduction 6
2.2 Theoretical background 7
2.2.1 Crosslinking kinetics 7
2.2.2 Crosslinking degree 10
2.3 Methods 12
2.3.1 Material preparation 12
2.3.2 Thermal histories 12
2.3.3 Calorimetric analysis 15
2.3.4 Rheological analysis 15
2.3.5 Swelling analysis 15
2.4 Results and discussion 16
2.4.1 Crosslinking kinetics 16
2.4.2 Crosslinking degree 26

2.5 Summary and conclusive remarks 30

3 Glass fibers characterization **32**
3.1 Introduction 32
3.2 Theoretical background 32
3.3 Methods 34
3.4 Results and discussion 35
3.4.1 Optical analysis 35
3.4.2 Mechanical tests 36
3.5 Summary and conclusive remarks 39

4 GF - PDMS composite **40**
4.1 Introduction 40
4.2 Theoretical background 41
4.2.1 Macromechanical behavior of a lamina 43
4.2.2 Micromechanical behavior of a lamina 48
4.2.3 Classical Lamination Theory 51
4.3 Production of the composite 56
4.3.1 Preparation of unidirectional fiber layers 56
4.3.2 Vacuum-Assisted Resin Infusion 58
4.3.3 Molding 59
4.3.4 Fiber-volume fraction evaluation 61
4.3.5 Microscopy 61
4.4 Lamina's mechanical characterization: small strains 63
4.4.1 Methods 63
4.4.2 Determination of E_1 64
4.4.2.1 Experimental results 66
4.4.2.2 Micromechanical models 67
4.4.3 Determination of E_2 68
4.4.3.1 Experimental results 68
4.4.3.1.1 Local strains 68
4.4.3.1.2 Global strains 70
4.4.3.2 Micromechanical models 72
4.4.4 Determination of Poisson's ratios 75
4.4.5 Determination of G_{12} 79
4.4.5.1 Experimental results 79
4.4.5.2 Micromechanical models 84

4.4.6 Summary and conclusive remarks 84
4.5 Symmetric-balanced laminates: stress-strain behavior at large strains 85
4.5.1 Introduction 85
4.5.2 Quasi-static tensile tests 86
4.5.3 Cyclic load-unload quasi-static tensile tests 97
4.5.4 Summary and conclusive remarks 99
4.6 Antisymmetric laminates: load coupling 100
4.6.1 Introduction 100
4.6.2 Preliminary study: CLT and FEM 101
4.6.3 Experimental 113
4.6.4 Model to experimental curves comparison 119
4.6.5 Summary and conclusive remarks 120
4.7 Summary and conclusive remarks 121

5 Conclusions and future developments **124**

A Quasi-static tensile tests on Sylgard®184 **127**

Bibliography **129**

List of Figures

2.1 Thermal histories imposed to the material for kinetics evaluation in both calorimetric and rheological analyzes (temperature vs. time). In black "isothermal conditions" IT, in blue "dynamic conditions" DT. 13

2.2 Thermal histories imposed to the material in rheological analyzes for the evaluation of the influence of the thermal history on the mechanical properties (temperature vs. time). In black thermal histories for which $\dot{T} = 8°C/min$ and T_c ranges from 65 to 150°C, in gray thermal histories for which $T_c = 100°C$ and $\dot{T}$ ranges from 1 to $8°C/min$. 14

2.3 Specific heat flow, ϕ vs time, t measured applying the thermal histories showed in Figure 2.1. In black "isothermal conditions" IT, in blue "dynamic conditions" DT. Raw data were corrected by baseline subtraction. 17

2.4 Mean conservative component of the shear modulus, G' (continuous lines) and mean dissipative component of the shear modulus, G'' (dashed lines) with the respective error bands, vs time, t in (a) "dynamic conditions" DT and (b) "isothermal conditions" IT. The diamonds indicate the gel points. 18

2.5 Comparison of conversion from calorimetric analysis α_C (dashed lines) and conversion from rheological analysis α_R (continuous lines) vs time, t in (a) "dynamic conditions" DT and (b) "isothermal conditions" IT. 19

2.6 Comparison of conversion rates from calorimetric analysis $d\alpha_C/dt$ (dashed lines) and from rheological analysis $d\alpha_R/dt$ (continuous lines) vs time, t in (a) "dynamic conditions" DT and (b) "isothermal conditions" IT. 19
2.7 Comparison of experimental (continuous lines) and calculated (dashed lines) conversion rates from calorimetric analysis $d\alpha_C/dt$ vs time, t in (a) "dynamic conditions" DT and (b) "isothermal conditions" IT. 22
2.8 Comparison of experimental (continuous lines) and calculated (dashed lines) conversion rates from rheological analysis $d\alpha_R/dt$ vs time, t in (a) "dynamic conditions" DT and (b) "isothermal conditions" IT. 23
2.9 Comparison of experimental (continuous lines) and calculated (dashed lines) conversion from calorimetric analysis α_C vs time, t in (a) "dynamic conditions" DT and (b) "isothermal conditions" IT. 24
2.10 Comparison of experimental (continuous lines) and calculated (dashed lines) conversion from rheological analysis α_R vs time, t in (a) "dynamic conditions" DT and (b) "isothermal conditions" IT. 25
2.11 Temperature, T vs. time, t iso-conversion curves map for $\alpha_R = 0.1, 0.53, 0.9$. The illustrative map refers to isothermal curing conditions differing in the heating ramp. a: $\dot{T} = 2°C/min$, b: $\dot{T} = 8°C/min$, c: ideal step heating. 26
2.12 Conservative and dissipative components G' and G'' measured at $25°C$, at the end of the each thermal history vs. (a) heating rate, $\dot{T}$ and (b) curing temperature T_c applied in the curing process. 27
2.13 (a) Polymer extractable fraction, w_{ext} and (b) Volume fraction of polymer in the swollen network, v_2 vs. curing temperature, T_c. 28

2.14 Mean molecular weight between crosslinks, M_c vs. curing temperature T_c. Black crosses represent data from rheological analysis and colored markers are data from swelling analysis. For the latter data, values obtained according to Equation 2.11 from Flory and Rehner, Equation 2.12 from Rennar and Oppermann and Equation 2.13 from Robert are reported. . 29

3.1 Schematic diagram showing contributions in the gap measurement. L_t is the gap between the clamps, L_0 is the initial length of the fiber, ΔL is the elongation of the single fiber, k is the spring constant and F the force measured by the testing machine. 33
3.2 A schematic of the mounting system for quasi-static tensile test of single glass fibers. 34
3.3 (a) Optical image of a single glass fiber before testing. (b) Optical image of a single fiber after testing. 35
3.4 (a) Distribution of fibers diameter, Φ versus gauge length, L_0. (b) Distribution of fibers area, A versus gauge length, L_0. . . 36
3.5 Force versus cross-head displacement curves. Approximate fiber gauge length: (a) about 15 mm, (b) about 25 mm, (c) about 40 mm, (d) about 60 mm. 37
3.6 Plot of $(L_t - L_0)/F$ versus L_0/A for (a) $F = 0.05\ N$, (b) $F = 0.10\ N$, (c) $F = 0.15\ N$, (d) $F = 0.20\ N$. The dashed lines represent the linear fitting. 38

4.1 (a) A lamina along with its principal material axes 1, 2 and 3. (b) Laminate formed as bonded stack of laminae with various orientations of principal material directions with respect to the laminate principal axis x, y and z. 42
4.2 Predicted modulus bounds for a laminate with $E_1 = 70\ GPa$ and $E_2 = 3\ GPa$. 51
4.3 Geometry of deformation in the $x - z$ plane. 52
4.4 Forces and moments on a laminate. 54
4.5 Illustration of the physical meaning of the ABD matrix. . . 55
4.6 (a) Unidirectional glass fibers tape with cotton stitches. Areal weight 210 g/m^2. (b) Unidirectional glass fibers tape with thermowelded stitches. Areal weight 600 g/m^2. 57

4.7 Dry unidirectional glass fibers tapes without stitches, ready to be embedded in the PDMS matrix. The fibers are held in place by the adhesive tape at the ends. (a) Layer for 0° or 90° fiber angle. (b) Layer for $+45^\circ$ or -45° fiber angle. 57
4.8 Schematic illustration of the vacuum assisted resin infusion process (VARI). 58
4.9 Schematic illustration of the process applied to produce a laminates with a mold. 60
4.10 Micrographs of unidirectional GF-PDMS laminates cut perpendicularly to the fiber direction. Fibers are the light gray circle. (a) Magnification level 50x. (b) Magnification level 100x. (c) Magnification level 200x. 62
4.11 Quasi-static tests performed to measure the four independent elastic constants of the lamina. (a) Tensile test in fibers direction. (b) Tensile test in direction perpendicular to the fibers. (c) Tensile tests on symmetric-balanced laminates $[+45, -45]_{2S}$. 64
4.12 Illustration of the behavior of unidirectional continuous fibers flexible composites clamped without end tabs. Yellow lines are the continuous fibers. From left to right: the specimen before clamping, the specimen with hourglass shape due to the compression of the clamps, the specimen tends to expand (green arrows) when a load in the fiber direction is applied (orange arrows). 65
4.13 Illustration of the gripping system employed to perform quasi-static tensile tests in fibers direction. (a) Specific end tabs to properly clam the specimen. (b) U-shaped" built-in tabs to properly hold the specimen without adding tabs. . . 66
4.14 Stress-strain curves of uniaxial tensile tests in fibers direction. (a) Specimens with end tabs and fiber-volume fraction $v_f = 0.31$. (b) Specimens with U-shaped ends and fiber-volume fraction $v_f = 0.37$. 67
4.15 Tensile modulus, E_1 versus fiber-volume fraction, v_f. 68

4.16 Tensile modulus, E_1 versus fiber-volume fraction, v_f. The light blue line is the *spring-in-parallel* model (Equation 4.24) with $E_f = 72000\ MPa$ and $E_m = 3.3\ MPa$. Circles are experimental results. 69
4.17 (a) Example of strains distribution of a "type A" specimen. The upper image shows the strain distribution after 2.4 s from the beginning of the test, the lower image shows the strain distribution after 29 s from the beginning of the test. The colored dots on the left of the two maps refer to the color of the curve in (b) taken at the same time. (b) Local strain, ε_x, versus the coordinate x of the central line of the specimen (white line in (a)). Curves colored from red to pink indicate the ε_x distribution at different increasing times. 70
4.18 (a) Example of strains distribution of a "type B" specimen. The upper image shows the strain distribution after 11 s from the beginning of the test, the lower image shows the strain distribution after 37 s from the beginning of the test. The colored dots on the left of the two maps refer to the color of the curve in (b) taken at the same time. (b) Local strain, ε_x, versus the coordinate x of the central line of the specimen (white line in (a)). Curves colored from red to pink indicate the ε_x distribution at different increasing times. 71
4.20 Tensile modulus, E_2 versus fiber-volume fraction, v_f. 71
4.19 Stress-strain curves of uniaxial tensile tests with load perpendicular to the fibers direction. In green specimens with $v_f = 0.46$, in gray specimens with $v_f = 0.32$ and in orange specimens with $v_f = 0.21$. 72
4.21 Tensile modulus, E_2 versus fiber-volume fraction, v_f. Comparison of experimental data with *spring-in-series* model (Equation 4.29) and Halpin-Tsai equation (Equation 4.31). ξ is the fibers reinforcement factor. 73
4.22 (a) E_{m_t} calculated according 4.49, normalized respect to the modulus of the pure matrix without fibers ($E_m = 3.3\ MPa$) versus fiber-volume fraction, v_f. (b) $Log(E_{m_t}/E_m - 1)$ versus $Log(v_f)$. Black dots are experimental values. Purple line is the linear fit. 75

4.23 (a) E_{m_t} calculated according Equation 4.49, normalized respect to the modulus of the pure matrix without fibers ($E_m = 3.3\ MPa$) versus fiber-volume fraction. Purple line reproduce Equation 4.50 with $b = 2.5$ and $A = 54$. (b) Tensile modulus, E_2 versus fiber-volume fraction, v_f. Comparison of experimental data (black dots) with Equation 4.52 with $b = 2.5$ and $A = 54$ (purple line). 76
4.24 Strains ε_x and ε_y versus time for (a) quasi-static tensile tests with load applied in the fibers direction (direction 1). (b) Quasi-static tensile test with load in direction perpendicular to the fiber (direction 2). 77
4.25 Theoretical limits of Poisson's ratios and experimental results. (a) The orange line shows the limits of $|\nu_{12}|$ according to Equation 4.54. Validity range for the Poisson's ratio for the fiber-volume fractions considered in this work is highlighted. The filled black dots are the experimental values. The empty dots are the ν_{12} values calculated with Equation 4.4 from the ν_{21} experimentally evaluated. (b) The green line shows the limits of $|\nu_{21}|$ according to Equation 4.54. The area of validity of the Poisson's ratio for the fiber-volume fractions considered in this work is highlighted. The filled black dots are the experimental values. The empty dots are the ν_{21} values calculated with Equation 4.4 from the ν_{12} experimentally evaluated. 78
4.26 Schematic view of the analyzed area of the specimen employed for the measurement of the in-plane shear modulus G_{12}. 80
4.27 Strain Mohr's circle representations. (a) State of plane strain in which $|\varepsilon_x| = |\varepsilon_y|$. (b) State of plane strain in which $|\varepsilon_x| < |\varepsilon_y|$. Small compressive strains exist at 45° to the x-y axis of the specimen. 81
4.28 Schematic representation of fibers reorientation in a lamina of the specimen during loading. 82

4.29 Coordinate of the center of the Mohr's circle $\varepsilon_{c_{Mohr}}$ and fibers angle ϑ versus the test time of specimens with fiber-volume fraction $v_f = 0.31$. The lines in pale colors are the values for which $\Delta\vartheta > 1.5°$. 82
4.30 Shear stress τ_{12} - shear strain γ_{12} curves up to fibers reorientation $\vartheta = 1.5°$ for specimens with fiber-volume fraction $v_f = 0.26$, $v_f = 0.31$ and $v_f = 0.37$. 83
4.31 Shear modulus G_{12} calculated as the slope of the linear fit of the τ_{12} - γ_{12} curves in the range $0 < \gamma_{12} < 0.005$, versus fiber-volume fraction. 83
4.32 Shear modulus, G_{12} versus fiber-volume fraction, v_f. Comparison of experimental data with *spring-in-series* model (Equation 4.30) and Halpin-Tsai Equation (Equation 4.31). ξ is the fibers reinforcement factor. 84
4.33 Illustration of the area employed for measurement of strains ε_x and ε_y (red rectangle) and areas where the specimen is not free to deform because the fibers have one end blocked between the clamps (yellow crosses). 88
4.34 True stress-true strain curves $\sigma_{x\ true} - \varepsilon_{x\ true}$ of symmetric-balanced laminates $[+30, -30]_{2S}$, $[+45, -45]_{2S}$, $[+60, -60]_{2S}$ and $[+75, -75]_{2S}$. 89
4.35 True stress-true strain curves $\sigma_{x\ true} - \varepsilon_{x\ true}$ of a symmetric-balanced laminates $[+45, -45]_{2S}$. Three different zones can be identified: initial region at low ε_x (Zone 1), intermediate "softened" region (Zone 2) and final stiffening region at high ε_x (Zone 3). 89
4.36 (a) Tangent modulus E_t versus $\varepsilon_{x\ true}$ for $[+30, -30]_{2S}$ and $[+45, -45]_{2S}$ laminates. (b) Tangent modulus E_t versus $\varepsilon_{x\ true}$ for $[+60, -60]_{2S}$ and $[+75, -75]_{2S}$ laminates. 90
4.37 (a) True stress - strain curves $\sigma_{true} - \varepsilon_{true}$ of the PDMS Sylgard®184 during quasi-static tensile tests. Tests parameters are reported in A. (b) Stress - strain curve of carbon-black filled rubber under quasi-static uniaxial tensile test. 91
4.38 Variation of the modulus E_x versus the angle ϑ between direction x and direction 1. Note that y axis is in logarithmic scale. 93

4.39 Variation of the modulus $E_{x\ \mathrm{CLT}}$ versus the fiber angle ϑ. . . 93
4.40 (a) True strains in width direction $\varepsilon_{y\ true}$ versus true strain in longitudinal direction $\varepsilon_{x\ true}$. (b) True strains in thickness direction $\varepsilon_{z\ true}$ versus true strain in longitudinal direction $\varepsilon_{x\ true}$. 94
4.41 (a) Variation of fibers angle ϑ versus the strain in loading direction $\varepsilon_{x\ true}$. (b) Variation of $\varepsilon_{z\ true}$ versus ϑ. Note that ϑ varies from 80 to 0, to display the load increase during the test from left to right. 96
4.42 Tangent modulus E_t versus fibers angle ϑ of the different laminates. 97
4.43 Engineering stress - strain curves for loading-unloading tests on $[+45, -45]_{2S}$ specimens. (a) Comparison of the three cyclic tests. (b) Up: Magnification of 1° cycle. Down: magnification of 2° cycle A. 98
4.44 (a) Sketch of the antisymmetric lamination sequence adopted, oriented along the $x-y-z$ coordinates system.(b) Sketch of the expected extension-twist coupling. 102
4.45 (a) Strains along the thickness (z coordinate) of a laminate with stacking sequence $[-75,90,+75]$ subjected to a force per unit width $N_x = 3\ N/mm$. (b) Stresses along the thickness (z coordinate) of a laminate with stacking sequence $[-75,90,+75]$ subjected to a force per unit width $N_x = 3\ N/mm$. (c) Strains along the thickness (z coordinate) of a laminate with stacking sequence $[-15,0,+15]$ subjected to a force per unit width $N_x = 30\ N/mm$. (d) Stresses along the thickness (z coordinate) of a laminate with stacking sequence $[-15,0,+15]$ subjected to a force per unit width $N_x = 30\ N/mm$. 102
4.46 (a) ε_x (b) ε_y (c) $\widehat{\gamma_{xy}}$ versus ϑ for laminates $[-\vartheta,90,+\vartheta]$ subjected to a force per unit width $N_x = 3\ N/mm$. (d) ε_x (e) ε_y (f) $\widehat{\gamma_{xy}}$ versus ϑ for laminates $[-\vartheta,0,+\vartheta]$ subjected to a force per unit width $N_x = 30\ N/mm$. 103
4.47 (a) $\widehat{\gamma_{xy}}/\varepsilon_x$ versus ϑ for laminates $[-\vartheta,90,+\vartheta]$. (b) $\widehat{\gamma_{xy}}/\varepsilon_x$ versus ϑ for laminates $[-\vartheta,0,+\vartheta]$. 104

4.48 Boundary conditions and loads applied in the finite element models. (a) No kinematic constrains, loads acting in x direction applied at the two opposite sides. (b) Encastred on one side, load applied in x direction on the opposite side. (c) Encastred on one side, constrained in y and z direction on the opposite side, load applied in x direction on the side not encastred. 106
4.49 FEM analysis of an antisymmetric laminate $[-15, 90, +15]$ subjected to boundary conditions and loads showed in Figure 4.48a. *Nlg OFF*. Distribution of the displacement in z direction w_o. (a) Frontal view. (b) Isometric view. 107
4.50 FEM analysis of an antisymmetric laminate $[-15, 90, +15]$ subjected to boundary conditions and loads showed in Figure 4.48b. Distribution of the displacement in z direction w_o. (a) *Nlg OFF*. Frontal view. (b) *Nlg OFF*. Isometric view. (c) *Nlg ON*. Frontal view. (d) *Nlg ON*. Isometric view. 108
4.51 Reference system of the laminate. 109
4.52 Expected twisting angle ϕ versus N_x, calculated from CLT with Equation 4.75 and from the numerical simulation with Equations 4.71 (FEM Case A), 4.72 (FEM Case B (*Nlg OFF*) and 4.73 (FEM Case B (*Nlg ON*) for laminates with stacking sequences $[-15, 90, +15]$, $[-30, 90, +30]$, $[-45, 90, +45]$, $[-60, 90, +60]$ and $[-75, 90, +75]$. 110
4.53 FEM analysis of an antisymmetric laminate $[-15, 90, +15]$ subjected to boundary conditions and loads showed in Figure 4.48c. Isometric view. Distribution of the displacements in z direction w_o. (a) *Nlg OFF*. (b) *Nlg ON*. 111
4.54 Torque Γ versus the applied force N_x, calculated from CLT with Equation 4.79 and from the numerical simulation, Case C, for laminates with stacking sequences $[-15, 90, +15]$, $[-30, 90, +30]$, $[-45, 90, +45]$, $[-60, 90, +60]$ and $[-75, 90, +75]$. 112
4.55 Sketch of *free rotation* mode (left) and *no rotation* mode (right) clamp operation. 113

4.56 $N_x - \varepsilon_x$ curves in x direction for $[-15, 90, +15]$, $[-30, 90, +30]$, $[-45, 90, +45]$, $[-60, 90, +60]$ and $[-75, 90, +75]$ laminates tested with clamps in both *no rotation* and *free rotation* mode. N_x is reported with different ranges in order to allow the assessment of the effect of the clamping mode on the specimen mechanical behavior. 115
4.57 Comparison of $N_x - \varepsilon_x$ curves in x direction for $[-15, 90, +15]$, $[-30, 90, +30]$, $[-45, 90, +45]$, $[-60, 90, +60]$ and $[-75, 90, +75]$ laminates. 116
4.58 (a) $-\varepsilon_y$ versus ε_x of specimens tested in *no rotation* mode. (b) Fibers angles ϑ of the external layers of the laminates versus ε_x of specimens tested in *no rotation* mode. 117
4.59 (a) Twisting angle ϕ versus N_x of specimens tested in *free rotation* mode. (b) Torque Γ versus N_x of specimens tested in *no rotation* mode. 118
4.60 (a) Slope of ϕ - N_x curves versus ϑ of laminates $[-\vartheta, 90, +\vartheta]$ tested in *free rotation* mode. (b) Slope of Γ - N_x curves versus ϑ of laminates $[-\vartheta, 90, +\vartheta]$ tested in *no rotation* mode. 118
4.61 N_x - ε_x experimental curves and curves predicted by CLT. . 119
4.62 (a) Comparison of theoretical and experimental slope of ϕ - N_x curves for $[-\vartheta, 90, +\vartheta]$ laminates with $\vartheta = 15, 30, 45, 60, 75°$. Note that y axis is in logarithmic scale. (b) Comparison of theoretical and experimental slope of Γ - N_x curves for $[-\vartheta, 90, +\vartheta]$ laminates with $\vartheta = 15, 30, 45, 60, 75°$. 120

A.1 True stress - strain curves $\sigma_{true} - \varepsilon_{true}$ of the PDMS Sylgard®184 during quasi-static tensile tests. 128

List of Tables

2.1 Time at gel point of the performed thermal histories (see Figure 2.1 for codes DT^* and IT^*) 18
2.2 Kamal's model parameters obtained by least squares criterium (Equation 2.9) from calorimetric and rheological analysis. 21

3.1 System compliance, k^{-1} and Young modulus, E calculated at different values of force, F. 38

4.1 Equations employed to calculate the material constants in principal directions of a single lamina of the GF-PDMS composite with $v_f = 0.3$. The equations are based on the experimental study described in Section 4.4. 92
4.2 Material constants assigned for the finite element simulation of the laminate. 105

Chapter 1

Introduction

1.1 Background and motivation

After the World War II, the development of new composite materials has raised an increasing interest. Several composites have been developed over the years, characterized by different constituent materials and types of reinforcement depending on their application field. Among them, fiber-reinforced polymers (FRPs) found wide applications in structural field, where they were mainly used as reinforcing elements of existing structures, for example concrete beams, or as an alternative to conventional materials in the design of structures, such as wind turbines, airplane parts or automobile frames [1, 2]. At the same time fiber-reinforced composites with elastomeric matrices, FREs (fiber-reinforced elastomers), also developed. In these composites, the elastomeric matrix, while characterized by good performance in flexibility, damping and absorption, is limited by its low strength and stiffness, which prevent its application in those fields where load bearing is required. The integration of rigid reinforcing elements into elastomeric matrices would allow their mechanical properties to be improved, partially maintaining the flexibility that characterize elastomers. FREs have been largely employed in car tires and conveyor belts for years, but their applications, apart from these few fields, have always been overlooked. In recent years, with the growth of the field of soft robotics, the interest for FREs increased, particularly for biomimetic applications, trying to mimic the behavior of natural being from locomotion and morphing, to the development of prosthetics or exoskeletons. Elastomeric composites,

capable of meeting the required characteristics of light weight, load bearing capability and high deformability are very promising for this kind of applications. Especially for soft robotics applications, the combination of elastomers with properly oriented reinforcements (e.g. continuous fibers) can generate composites with strongly direction-dependent properties that lead to the possibility to obtain complex deformation responses in the presence of simple stress states. For example, in the so called *smart soft composites* (SSCs), the application of an external simple stimulus, provided by an embedded active component, usually shape memory alloys that respond to mechanical, thermal, or electrical inputs, can enable responses that could not be achieved neither by traditional isotropic materials nor by anisotropic stiff advanced composites [3, 4]. The complex displacements that are obtained in response to the applied simple stimulus are the result of an appropriately design of the orientation of the fibers and of the high deformability of the matrix. The orientation of the fibers determines the type of response that the FREs will experience upon application of a stimulus due to load-coupling effects common to all anisotropic materials. The high deformability of FREs makes possible to exploit a wide range of movements required by different applications (for example the movements of an artificial finger) which could not be achieved by conventional FRPs, which are characterized by much stiffer matrices, even with the application of low-intensity stimuli.

The state of the art on the development of these stimulus-responsive materials with load-coupling effects is still quite limited. The literature mainly reports on studies focused on the possible uses of SSCs and their actuation mechanisms, such as the rehabilitation glove showed by Chen et al. [5], the "muscle glove" showed by Yao et al. [6] or the bio-inspired autonomous underwater vehicle showed by Kim et al. [4] and studies on the analysis of the overall response and the displacement ranges achievable by these composites [3, 7–11]. Some literature is also available about rope-rubber composites and fabric-reinforced elastomers [12–14], but an extensive understanding of the deformation mechanisms of fiber-reinforced elastomers as well as a suitable characterization methods for determining their mechanical response is not present.

1.2 Aim and objectives

The present work aims to expand the knowledge of fiber-reinforced elastomers. In particular, a study of a continuous glass fibers (GF) reinforced polydimethylsiloxane (PDMS) will be presented. The first part of the work is centered on a deep characterization of the PDMS matrix and on how its processability and its mechanical properties are influenced by the production process and the relevant process parameters. The work then proceeds with the characterization of the glass fiber-polydimethylsiloxane composite according to the classical approach typically adopted for the characterization of fiber-reinforced polymers, that is, characterizing a thin layer of composite material with mono-oriented continuous fibers, the so called *lamina*. According to the classical approach, once the properties of the single lamina are known, the behavior of any laminate composed of stacked laminae can be predicted. This study aims to explore to what extent this approach could also applied to FREs, which are characterized by a nearly incompressible, highly deformable soft elastomeric matrix with a modulus on the order of MPa and by fibers with a modulus on the order of tens of GPa, that is moduli that differ more then four orders of magnitude, resulting in a level of anisotropy never explored in traditional composites. The limitations of the experimental procedures usually employed for the mechanical characterization of a lamina will be displayed and some solutions will be proposed. Then, an example of a complex response obtainable with a particular lamination sequence will be presented, and the experimental results will be compared with the theoretical prediction obtainable by applying the classical approach.

1.3 Structure of the thesis

The thesis is structured as follows:

- *Chapter 2* is focused on the study on the PDMS matrix. After a brief theoretical background, a detailed study on how the thermal history applied to the uncured material influences its crosslinking kinetic is showed. The kinetics is studied through two different approaches, using differential scanning calorimetry and rheological analysis and a kinetics model is proposed. Then, the influence of the curing thermal

history on the structure and the elastic modulus of the crosslinked PDMS is showed. The crosslinking degree is estimated from the mechanical properties of the formed PDMS, measured by rheological analysis, and from swelling measurements, and a correlation between the two methods is found.

- *Chapter 3* briefly describes the characterization of the modulus of the glass fibers employed for the production of the composite material.
- *Chapter 4* reports the whole investigation of the GF-PMDS composite, and it is organized into the following subsections:
  - *Section 4.1* illustrates in detail the motivation and the relevance of investigating these types of composites.
  - *Section 4.2* gives a brief theoretical background about the features of anisotropic materials and introduces the basis of the classical approach employed to study laminates.
  - *Section 4.3* introduces the methods employed for the lab scale manufacturing of these continuous fiber composites and the most critical aspects encountered in the production of this type of composites are discussed.
  - *Section 4.4* shows the mechanical characterization of a composite single lamina at small strains. In particular, the methods for the evaluation of the four independent material constants that characterize a single lamina (elastic modulus in direction of the fibers, elastic modulus in direction perpendicular to the fibers, major Poisson's ratio and shear modulus in the plane of the lamina) are illustrated and the relevant results reported are compared with predictions from micromechanical models.
  - *Section 4.5* shows the characterization of a specific symmetric-balanced lamination sequence, up to large strains and the peculiar behavior observed is discussed.
  - *Section 4.6* describes the mechanical behavior of an antisymmetric lamination sequence. The load-coupling effects are observed and quantified and the response is compared with the prediction of the classical lamination theory. Some finite element simulations are also presented.

  - *Section 4.7* briefly summarizes all the outcomes of the composite characterization.

- *Chapter 5* recalls the main results achieved during the present study. Ideas for future developments are also proposed.

Chapter 2

Polydimethylsiloxane characterization

2.1 Introduction

In this chapter a deep study on the Sylgard®184 polydimethylsiloxane (PDMS) is showed. Sylgard®184 is a commercially available PDMS produced by Dow Corning. It is a two components system consisting in an elastomer base and a curing agent that when mixed, react to form a three dimensional network. Thanks to their interesting properties such as good biocompatibility, low toxicity, good physiological inertness, a high humidity and temperature stability, high transparency and high deformability [15], PDMSs are commonly used in several applications such as medical sensors, electronic devices like micro electro-mechanical system (MEMS), smart soft composites or soft robots manufacturing and for the production of biomedical soft tissues, elastic lenses and waveguides [4,7,16–23]. The crosslinking reaction of Sylgard®184 takes place spontaneously at room temperature over approximately 48 h, but this time can be shortened by heating [24] and it is known that the crosslinking kinetics [25,26] and the structure of the formed network and thus the relevant mechanical properties [27,28] are significantly affected by the thermal history applied during the crosslinking process. Since the mechanical performance of the devices for which the PDMS is used strongly depends on the behavior of the constituent materials, the knowledge of how the PDMS mechanical properties depend on the curing history is very important for a proper material and device

design. Furthermore, due to a relatively high value of the uncured mixture viscosity and due to the fact that it further increases once the curing process has started, problems in processing PDMS are commonly encountered in a wide range of applications. For these reasons a systematic characterization of the crosslinking process kinetics could provide useful information to properly process the material.

The present study is intended to systematically characterize the crosslinking kinetic of Sylgard®184, providing a kinetic model to be used to predict how fast the material passes from a liquid state to a solid state, and thus is no more processable. At the same time the influence of the thermal history applied on the crosslinking degree and thus on the final mechanical properties of the PDMS is assessed. A thermal history consist usually in two steps: a first heating to reach a certain temperature and a second stage in which the temperature is kept constant for a certain time. The present study aims to investigate the different influence of the two steps on the crosslinking degree of the material. This study is preliminary to the characterization of a novel fiber-reinforced soft composite, but it may be also of general interest as its object is a PDMS widely used in literature. A short theoretical background to introduce the basic concept employed for the study will be followed by the description and analysis of the experimental results first in terms of crosslinking kinetic and then in terms of crosslinking degree.

2.2 Theoretical background

2.2.1 Crosslinking kinetics

PDMS is a chemically crosslinked elastomer with alternating silicon and oxygen atoms as backbone and side methyl groups. The evolution of the polymer crosslinking can be monitored following the change in some of the material physical properties induced by the occurring chemical reaction [29]. The hydrosilylation reaction that takes place in the PDMS crosslinking process is an exothermic reaction, thus the heat released during the reaction can be used to detect the evolution of the process. Furthermore, if it is assumed that, during the crosslinking reaction, the formation of each covalent bond releases the same amount of energy, the heat of reaction can be related to the amount of bonds formed within the network [30, 31].

During the crosslinking process a change in the mechanical properties of the material is also observed. For example, if we consider the dynamic mechanical response of the material in terms of conservative G' and dissipative G'' components of the shear modulus, both are related to the structure of the formed network, and their evolution allows to detect the liquid-like solid-like transition that occurs in the material. During crosslinking an increase in the moduli of the material is induced by the growth of the molecular chains, up to the formation of a three-dimensional network. The moment at which this network is formed is called "gel point" and can be detected observing the dynamic mechanical response. After this point, further crosslinks gradually form and both the moduli further increase, until the network is completed [32] .

In the present study, both the heat of reaction related to the exothermic hydrosilylation reaction that takes place during the crosslinking process and the response of the material in terms of dynamic shear modulus will be analyzed and compared. The heat of reaction has been measured with differential scanning calorimetry, the response in terms of dynamic shear modulus with rheological analysis. A complete description of how differential scanning calorimetry works can be found in [33] and detailed recommendations for collecting experimental thermal analysis data and performing kinetic computations can be found in [29, 34] . Likewise, a complete description about the operation of a rheometer and dynamic mechanical analysis can be found in [32]. Here we will focus only on the description of the theoretical approach adopted for the data analysis and interpretation of the results.

In order to describe the evolution of a certain properties during time a conversion α that varies from 0 (beginning of the process) to 1 (end of the process) is usually defined. Differential scanning calorimetry (DSC) can detect the heat of reaction released in time $Q(t)$, as heat flow $dQ(t)/dt$ and a conversion rate $d\alpha_C/dt$ can be defined as:

$$\frac{d\alpha_C}{dt} = \frac{1}{Q_T}\frac{dQ(t)}{dt} \tag{2.1}$$

where Q_T is the total heat of the reaction, obtained integrating the exothermic peak on the total reaction time. The conversion $\alpha_C(t)$ can be obtained integrating the reaction heat curve at each time step and normalizing over

the total heat Q_T:

$$\alpha_C(t) = \frac{\int_0^t \left(\frac{dQ(t)}{dt}\right) dt}{\int_0^{t_{end}} \left(\frac{dQ(t)}{dt}\right) dt} = \frac{Q(t)}{Q_T} \tag{2.2}$$

where t_{end} represents the time at which the reaction is completed. If it is assumed that, during the crosslinking reaction, the formation of each covalent bond releases the same amount of energy, the conversion can be related to the amount of bonds formed within the network [30,31].

In order to define the conversion related to the shear modulus change measured by rheological analysis, the evolution of the conservative component of the modulus, G' can be considered. The conversion $\alpha_R(t)$, can be defined as:

$$\alpha_R(t) = \frac{lnG'(t) - lnG'_{min}}{lnG'_{max} - lnG'_{min}} \tag{2.3}$$

where G'_{min} and G'_{max} are respectively the minimum and the maximum value of the conservative component of the modulus during curing. The conversion rate can be defined as the first derivative of $\alpha_R(t)$ in time: $d\alpha_R/dt$.

Among the definitions found in literature [26,35], the selected definition allows to better observe the trend of the conservative component of the modulus, given the wide variation expected for G', from 10^{-4} Pa when the reaction starts (liquid state) to 10^6 Pa at the end of the reaction (solid state). Furthermore, this description emphasizes the liquid-solid transition that is a very important step in all crosslinking processes.

In order to describe the rate dependence, $d\alpha/dt$, of the two conversions α above defined, a modified version of the autocatalytic model proposed by Kamal et al. [36] often used for silicon rubbers [25, 26, 37, 38] can be adopted:

$$\frac{d\alpha}{dt} = (K_1 + K_2\ \alpha^m)(1-\alpha)^n \tag{2.4}$$

where m and n are the orders of the reaction and K_1 and K_2 are rate

constants defined by Arrhenius Equation:

$$K_1 = A_1\ exp\left(-\frac{E_1}{R\ T}\right) \qquad K_2 = A_2\ exp\left(-\frac{E_2}{R\ T}\right) \tag{2.5}$$

with R = gas constant, T = absolute temperature, A_{1-2} = pre-exponential factor, E_{1-2} = activation energy. Since an order of the reaction higher than 2 is extremely uncommon, it can be assumed $m + n = 2$ [35,37]. Assuming, then, $E_1 = E_2 = E$ the model can be reduced to an equation of the form:

$$\frac{d\alpha}{dt} = k(T)\ f(\alpha) \tag{2.6}$$

where:

$$k(T) = exp\left(-\frac{E}{R\ T}\right) \tag{2.7}$$

and

$$f(\alpha) = \left(A_1 + A_2\ \alpha^{2-n}\right)(1-\alpha)^n \tag{2.8}$$

The model so defined has 4 parameters (E, A_1, A_2, n) to be identified in order to describe the kinetics. The parameters can be identified by minimization of the following function:

$$D = \sum_{i=1}^{w} \frac{\sqrt{\sum\left(\left|\frac{d\alpha}{dt}\right|_{exp} - \left|\frac{d\alpha}{dt}\right|_{model}\right)^2}_{i}}{w} \tag{2.9}$$

over the w experimental curves obtained from the different thermal histories performed. Then, to obtain the evolution of α in time, the model can be numerically integrated with *Runge Kutta* 4th order method.

2.2.2 Crosslinking degree

The degree of crosslinking of a polymer network can be described by mean of the mean molecular weight between crosslinks, M_c. The mean molecular weight between crosslinks is a measure of the molecular weight of the polymer chain between two links of the polymer network. Lower M_c means higher crosslinking density and vice versa. According to the theory of rubber elasticity [39], the rubber shear modulus G can be correlated to M_c by mean of the following relation (under the "phantom network"

assumption):

$$G = \frac{\rho_0 \, R}{2 \, M_c} \, T \tag{2.10}$$

where G = shear modulus of the rubber, ρ_0 = polymer density, R = gas constant, T = absolute temperature.

M_c can be also related to the swelling in solvents of ideal rubbers, through the Flory-Huggins theory of polymer solution. A detailed description of the theory of polymer systems can be found in [39, 40]. Toluene, since has a good interaction with PDMSs [41–43], has been chosen as solvent. Among the equations reported in literature, the approach proposed by Flory and Rehner [44], Rennar and Oppermann [45] and Robert et al. [43] have been considered and compared. Equations 2.11, 2.12 and 2.13 describe the equilibrium swelling with functionality of the crosslinks equal to 4, according to Flory and Rehner [44], Rennar and Oppermann [45] and Robert et al. [43], respectively:

$$-\frac{\rho}{M_c} = \frac{ln(1 - v_2) + v_2 + \chi \, v_2^2}{V_s \, v_2^{1/3}} \tag{2.11}$$

$$-\frac{\rho}{M_c} = \frac{ln(1 - v_2) + v_2 + \chi \, v_2^2}{V_s \, \frac{v_2^{1/3}}{2}} \tag{2.12}$$

$$-\frac{\rho}{M_c} = \frac{ln(1 - v_2) + v_2 + \chi \, v_2^2}{V_s \, \left(v_2^{2/3} - \frac{v_2}{2}\right)} \tag{2.13}$$

in which ρ = dry polymer density, M_c = mean molecular weight between crosslinks, V_s = molar volume of the solvent (for toluene 106.52 cm^3/mol [46]), v_2 = volume fraction of polymer in the swollen network and χ = solvent-polymer interaction parameter. The solvent-polymer interaction parameter depends on both the solvent and the polymer and may vary with the extent of crosslinking and with concentration [42], therefore, the determination of the solvent-polymer interaction parameter (in this case the toluene-PDMS interaction parameter) is not trivial and different values can be found in literature [47]. Bueche [42] considered a constant toluene-PDMS interaction parameter $\chi = 0.465$, differently, Robert et al. [43] states that the toluene-PDMS interaction parameter can be calculated as $\chi = \chi_0 + \beta \, v_2$ with $\chi_0 = 0.44$ and $\beta = 0.36$. In the present work these two proposals

for the solvent-polymer interaction parameter will be referred to as χ_B (Bueche) and χ_R (Robert), respectively. In the present analysis, χ_R has been adopted with Equation 2.13 while either χ_R and χ_B have been adopted with Equations 2.11 and 2.12.

M_c values obtained from swelling tests can then be compared to those obtained from rheological analysis and the applicability of the theory for the system analyzed can be verified.

2.3 Methods

2.3.1 Material preparation

The PDMS employed in this work, Sylgard®184, is a commercial two components system consisting of an elastomer base (component A) and a curing agent (component B). Both the components are initially liquid and transparent. Typically, the elastomer base contains linear PDMS pre-polymers with two vinyl end groups that react with the component B multifunctional crosslinker leading to a three-dimensional crosslinked network. The hydrosilylation reaction mechanism of the PDMS is known and well reported in literature [48, 49]. The two components are mixed at room temperature, with a low speed helix mixer for 10 min, in $10:1(A:B)$ mass ratio, as suggested by the supplier [24]. The mixture is first degassed in a vacuum bell jar for 20 min (low vacuum $P = 9\ 10^4 Pa$) to remove air bubbles incorporated during mixing and then kept at $4°C$ and used for rheological and calorimetric analysis within 5 h from mixing. The same procedure has been also adopted for the production of the PDMS to be used as matrix for the PDMS-GF composite (see Chapter 4).

2.3.2 Thermal histories

In order to describe the kinetics of the reaction, the following thermal histories have been considered (Figure 2.1):

- thermal histories in isothermal conditions (hereinafter referred to as IT) in which the sample is kept for 1 min at $25°C$ to stabilize the material temperature, then it is heated at the rate of $8°C/min$ to the curing temperature T_c at which it is kept for 1 h. Curing temperatures

$T_c = 65$, 75 and $85°C$ have been considered. In these histories the crosslinking is expected to occur at constant temperature during the isothermal step;

- thermal histories in dynamic conditions (hereinafter referred to as DT) in which the sample is kept 1 min at $25°C$, then it is heated up to $130°C$ at constant rate. Rates of 1, 2, 4 and $8°C/min$ have been adopted. In these histories the crosslinking is expected to occur during heating.

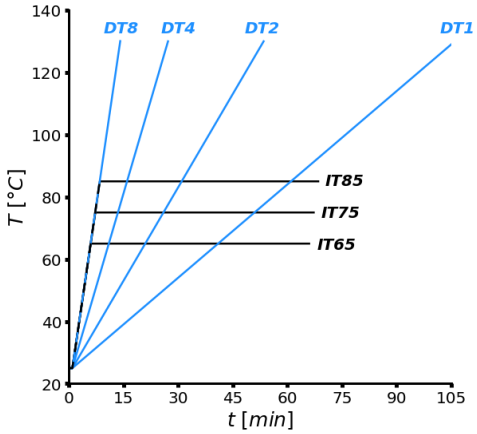


Figure 2.1: Thermal histories imposed to the material for kinetics evaluation in both calorimetric and rheological analyzes (temperature vs. time). In black "isothermal conditions" IT, in blue "dynamic conditions" DT. Adapted from [50].

In order to evaluate the influence of the thermal history on the mechanical properties of the crosslinked PDMS, the thermal histories employed are showed in Figure 2.2 and can be described with the following four steps:

- the sample is kept for 1 min at $25°C$ to stabilize the material temperature;
- the sample is heated at constant rate up to a defined temperature, T_c;
- the sample is kept at constant temperature, referred to as curing temperature T_c, for a curing time, t_c, of 4 h;
- the sample is cooled to $25°C$ at the rate of $8°C/min$ and kept at this temperature for 10 min to stabilize its temperature.

In particular, heating rates $\dot{T} = 1$, 2, 4 and $8°C/min$ were employed, fixing a constant $T_c = 100°C$, and a fixed heating rate of $8°C/min$ was employed with $T_c = 65$, 75, 85, 100, 125 and $150°C$. The first series of thermal histories were performed to study the effect of the heating rate on the PDMS properties, while the second series of thermal histories were performed to investigate the effect of the curing temperature on the properties of the PDMS. The range of heating rates was chosen considering that heating rates higher than $8°C/min$ did not allow homogeneous heating of the sample while $1°C/min$ was considered a reasonably low heating rate, low enough that crosslinking can occur almost entirely during sample heating. The temperatures explored are in the range of curing temperatures suggested by the supplier [24]. Furthermore, the thermal stability of the PDMS in this temperature range is well documented. Liu at al. [51] experimentally verified that thermal decomposition of Sylgard®184 starts at temperature about $200°C$ and reaches its maximum rate at $310°C$.

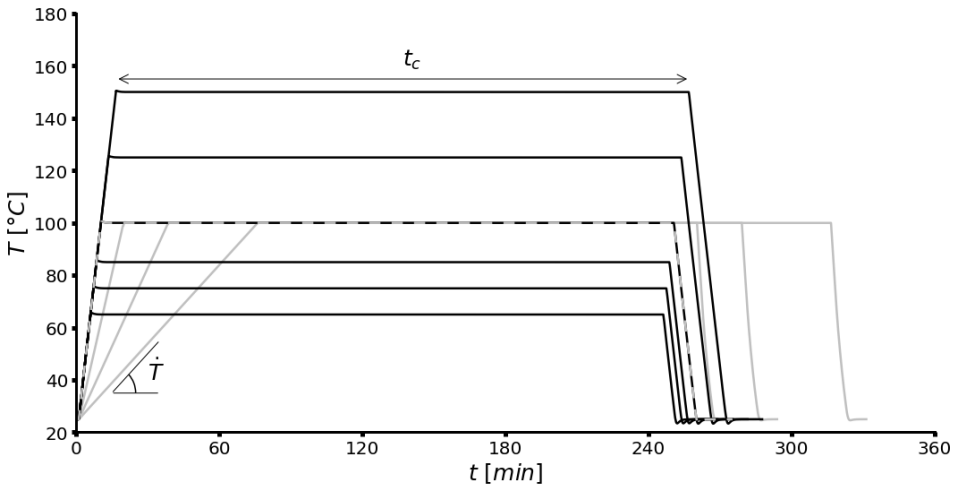


Figure 2.2: Thermal histories imposed to the material in rheological analyzes for the evaluation of the influence of the thermal history on the mechanical properties (temperature vs. time). In black thermal histories for which $\dot{T} = 8°C/min$ and T_c ranges from 65 to $150°C$, in gray thermal histories for which $T_c = 100°C$ and $\dot{T}$ ranges from 1 to $8°C/min$. Adapted from [52].

2.3.3 Calorimetric analysis

Differential scanning calorimetry measurements were performed under nitrogen, at atmospheric pressure, using a Mettler Toledo DSC 3 calorimeter. The sample mass used ranged from 16 mg to 29 mg. Each test was carried out twice to verify the repeatability of the obtained values. The thermal histories applied are detailed in Section 2.3.2.

2.3.4 Rheological analysis

Rheological dynamic mechanical analyzes in shear mode were performed with an Anton Paar MCR 502 rheometer, in plate-plate configuration (diameter of the plate 25 mm), to measure the evolution of the conservative and dissipative components of the complex shear modulus under the different thermal histories detailed in Section 2.3.2. The thermal histories could be applied by means of the Peltier plate and hood system H-PTD 200 which equipped the rheometer. The uncured PDMS mixture was first poured on the rheometer lower plate, then the upper plate was moved toward the lower one and positioned at a distance of 1 mm. The material in excess was trimmed before starting the test. All the measurements were performed in air and at atmospheric pressure and were carried out at constant frequency of 1 Hz, whereas the strain amplitude was set to 5% for values of the complex modulus, G^*, up to 4 10^5 Pa and to 0.5% for larger values. The linear behavior of the material was verified for both the experimental conditions applied. A normal force of 1 N was applied during the tests to avoid sample slip between the plates. All the tests were carried out at least three times to verify the repeatability of the measurements.

2.3.5 Swelling analysis

All swelling measurements have been performed at room temperature, 25$^\circ C$ and atmospheric pressure. The cylindrical samples (diameter = 25 mm, thickness = 1 mm) obtained at the end of the rheological experiments were cut in smaller specimens about one third of the initial volume, and the mass of each specimen, m_0, was measured before immersing it in a large excess of toluene for 24 h to reach the equilibrium state. Then, the swollen specimen mass, m', was measured after lightly pressing the specimen between two pieces of filter paper. The specimen was then left to dry for 12 h and the

mass of the dried specimen, m, was measured again. The 12 h drying period allowed to completely release the toluene dissolved in the PDMS (no further mass loss was observed even after a subsequent drying of the specimen under vacuum).

From these measurements the polymer extractable fraction, w_{ext}, that is the fraction of the polymer mass loses during immersion in toluene and the volume fraction of polymer in the swollen network, v_2 can been obtained as follows:

$$w_{ext} = \frac{(m_0 - m)}{m_0} \tag{2.14}$$

$$v_2 = \frac{\frac{m}{\rho}}{\frac{(m' - m)}{\rho_s} + \frac{m}{\rho}} \tag{2.15}$$

where m_0, m' and m are respectively the initial, swollen and dry mass of the specimen, ρ_s is the solvent density (0.865 g/cm^3 for toluene at room temperature [46]) and ρ is the density of the dry polymer after the extraction of the free chains. This last property was derived from the polymer density measured before extraction, ρ_0, according to the following equation:

$$\rho = \rho_0(1 - w_{ext\ m}) \tag{2.16}$$

where $w_{ext\ m}$ is the average value of the measured extractable fractions, w_{ext}. The polymer density ρ_0 was measured with a pycnometer Pycnomatic ATC Thermo Scientific, at 25°C, and resulted to be 1.070 ± 0.015 g/cm^3.

From the values of the volume fraction of polymer in the swollen network, v_2, the mean molecular weight between crosslinking of the different specimens can be calculated according to Equations 2.11, 2.12 and 2.13.

2.4 Results and discussion

2.4.1 Crosslinking kinetics

Figure 2.3 shows the specific heat flow, Φ, in time, t, measured by differential scanning calorimetry (DSC). The codes $DT1$, $DT2$, $DT4$, $DT8$, $IT65$, $IT75$ and $IT85$ refer to the corresponding thermal history applied (See Figure 2.1). The time at which the heat flow and thus the speed of the

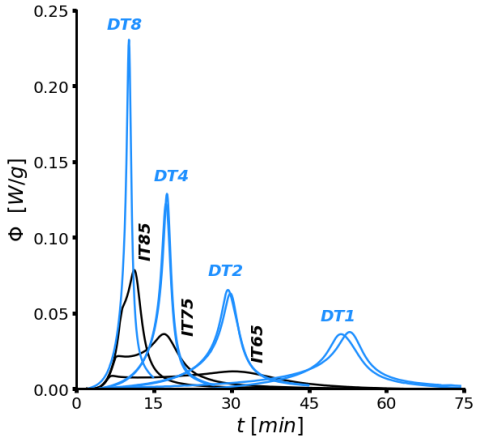
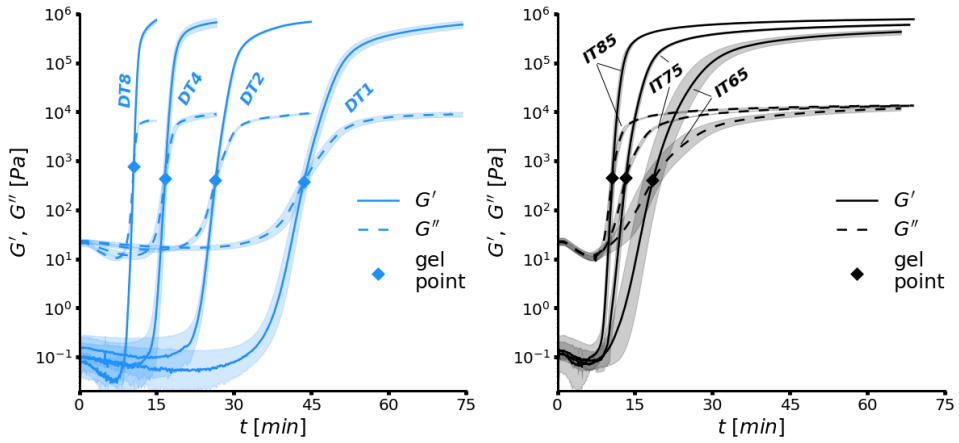


Figure 2.3: Specific heat flow, ϕ vs time, t measured applying the thermal histories showed in Figure 2.1. In black "isothermal conditions" IT, in blue "dynamic conditions" DT. Raw data were corrected by baseline subtraction. Adapted from [50].

reaction reaches its maximum depends on the thermal history applied. In particular, the reaction is faster if higher heating rate or higher isothermal curing temperatures are applied. The overlap of the first part of the IT curves with the $DT8$ one is consistent with the fact that in IT conditions the initial heating ramp applied to reach the curing temperature T_c is carried out at $8°C/min$, that is the same rate adopted in the $DT8$ thermal history (see Figure 2.1). Figure 2.4 shows the conservative and the dissipative components of the shear modulus, respectively G' and G'' measured during rheological analysis with the same thermal histories applied for the calorimetric analysis (Figure 2.1). Note that the y axis representation is logarithmic. Both G' and G'' start to sharply increase after an initial induction time. G' increases with higher rate then G'' and at a certain point the two components cross. The point in which G' equals G'' can be assumed, in first approximation, as the "gel point" [26], that is the point in which the transition between liquid-state and solid-state occurs. After this point both the moduli further increase up to a plateau which indicates that the reaction is concluded. The time at which the gel point occurs depend on the applied thermal history, in particular it occurs at shorter time if the heating rate or the isothermal curing temperature are higher. Table 2.1 shows the times at which the gel point occurs for the thermal history considered.

Table 2.1: Time at gel point of the performed thermal histories (see Figure 2.1 for codes DT^* and IT^*)

Thermal history	Time at gel point
$DT1$	$2609 \pm 50\ s$
$DT2$	$1583 \pm 19\ s$
$DT4$	$995 \pm 30\ s$
$DT8$	$635 \pm 10\ s$
$IT65$	$1099 \pm 110\ s$
$IT75$	$791 \pm 27\ s$
$IT85$	$638 \pm 24\ s$



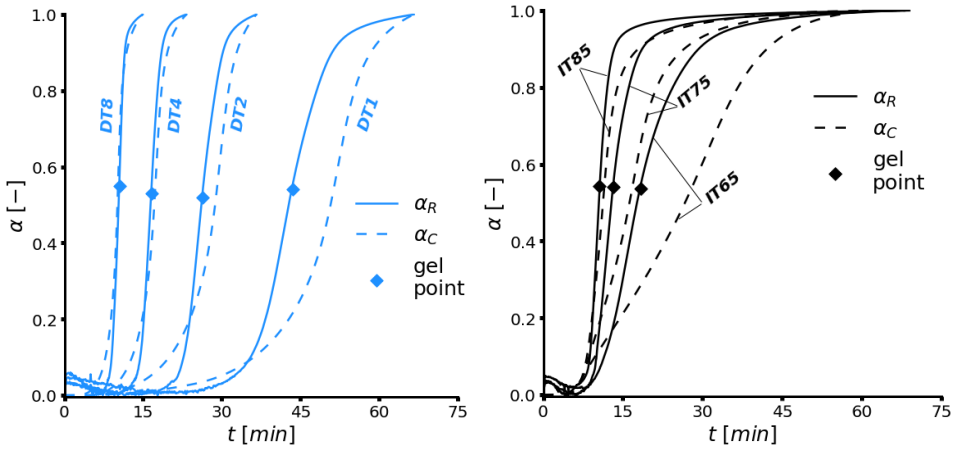
(a) (b)

Figure 2.4: Mean conservative component of the shear modulus, G' (continuous lines) and mean dissipative component of the shear modulus, G'' (dashed lines) with the respective error bands, vs time, t in (a) "dynamic conditions" DT and (b) "isothermal conditions" IT. The diamonds indicate the gel points. Adapted from [50].

A variation of the curing temperature of only $20°C$ or a change in the heating rate lower than one order of magnitude considerably affects the gel point time, and this highlights how these issues should be considered when designing the curing process of the material.

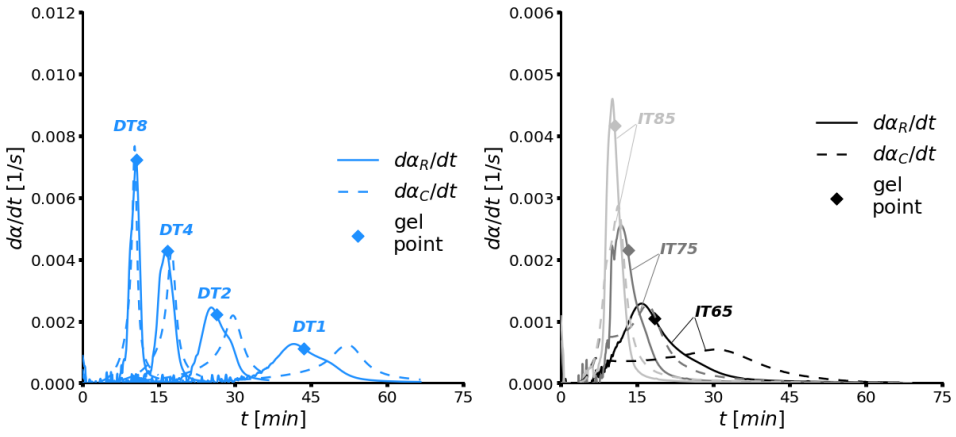
In order to compare calorimetric and rheological results in terms of evolution of the crosslinking reaction during time the conversions α_C and

α_R, and the conversion rates $d\alpha_C/dt$ and $d\alpha_R/dt$ calculated as described in Section 2.2.1, are showed respectively in Figure 2.5 and 2.6.



(a) (b)

Figure 2.5: Comparison of conversion from calorimetric analysis α_C (dashed lines) and conversion from rheological analysis α_R (continuous lines) vs time, t in (a) "dynamic conditions" DT and (b) "isothermal conditions" IT. Adapted from [50].



(a) (b)

Figure 2.6: Comparison of conversion rates from calorimetric analysis $d\alpha_C/dt$ (dashed lines) and from rheological analysis $d\alpha_R/dt$ (continuous lines) vs time, t in (a) "dynamic conditions" DT and (b) "isothermal conditions" IT. Adapted from [50].

The two conversions α_C and α_R show a similar "S-shapes" curve but the two processes evolve in different times. The calorimetric curves α_C starts to grow from the beginning of the curing process, confirming that the reaction starts just after the mixing of the two liquid parts also at room temperature. Otherwise, the rheological curves α_R shows and initial "induction" time in which there is no evident change in the mechanical properties of the material. The calorimetric analysis shows the heat released during the reaction, and can be correlated with the polymer network bonds formation. Probably, the change in the mechanical properties can be detected only after the formation of a certain amount of bonds. For each thermal history, after the first "induction" time, α_R starts to quickly increase, overcoming α_C (this behavior is more visible for dynamic thermal histories with low heating rate, as $DT1$ and $DT2$ or lower isothermal curing temperature as $IT65$ and $IT75$, Figure 2.5). The maximum of the conversion rate $d\alpha/dt$ occurs always at shorter time in rheological analysis than in calorimetric analysis (See Figure 2.6), and this difference is more evident at low heating rate, for DT tests and at low curing temperature for IT tests.

Another interesting observation can be made in relation to the conversions at the time at which the gel point (diamonds in Figure 2.5 and Figure 2.6) occurs. At that time, the conversion for the rheological tests α_R is 0.53 ± 0.01 while, the conversion measured from calorimetric tests α_C is lower and equal to 0.30 ± 0.05, independently of the transformation history. This indicates that whatever time the liquid like-solid like transition takes place, which depends on the reaction kinetics and thus on the applied thermal history, the conversion at the gel point is the same. Furthermore, the value of α_C at the gel point indicates that only about 30% of the chemical bonds formed during the whole crosslinking process are involved in the production of the infinite network that is formed at the gel point; the material is already in a gel state at a quite early stage of the chemical reaction and the further bonds formation is just responsible for the structure of the final network on which the mechanical properties will depend.

In order to fully describe the kinetics of reaction a modified version of the autocatalytic model proposed by Kamal et al. [36] was adopted. The applicability of the model assumption of a single step kinetics to the more complex reaction process under study have been verified in a previously

published paper [50], in which the Friedman isoconversional method [29] has been employed, and a constant activation energy has been obtained in the first phase of the crosslinking process, for calorimetric analysis up to $\alpha_C = 0.55$ and for rheological analysis up to $\alpha_R = 0.80$ [50].

In order to calculate the four Kamal's model parameters E, A_1, A_2 and n as described in Section 2.2.1 an optimization in two steps has been employed. Two different set of parameters have been calculated for calorimetric and rheological analysis. For calorimetric analysis, data in the range $0.15 \leq \alpha_C \leq 0.55$ (in which the Friedman analysis indicates constant activation energy [50]) were first used to determine all the model parameters. Then, a new estimation of the parameter n alone was obtained by using the data in the whole range $0 \leq \alpha_C \leq 1$, maintaining constant the other three parameters. For rheological analysis, first data in the range $0.10 \leq \alpha_R \leq 0.80$ (constant activation energy [50]) were used to determine all the parameters, then a better estimation of n was obtained considering only the first part of the curves $0 \leq \alpha_R \leq \alpha_{Rl}$ where α_{Rl} is the value of α in which $d\alpha_R/dt$ is maximum.

The experimental curves obtained from the thermal histories $IT65$, $IT75$, $IT85$, $DT1$, $DT2$, $DT4$ were taken into consideration for model parameters identification, while experimental curves from $DT8$ were used to verify the prediction ability of the model. The parameters obtained are summarized in Table 2.2.

Table 2.2: Kamal's model parameters obtained by least squares criterium (Equation 2.9) from calorimetric and rheological analysis.

Parameter	Calorimetric curves	Rheological curves
E	93.5 kJ/mol	71.5 kJ/mol
A_1	7.2 10^{10} $1/s$	0 $1/s$
A_2	2.9 10^{11} $1/s$	4.8 10^{8} $1/s$
n	0.96	1.28

A comparison of the present results with other PDMS systems studied in literature is reported in [50]. The value of the pre-exponential factor A_1 can be related to the trend of the initial conversion α: the A_1 value different from zero obtained in calorimetric conversion curves, describes the initial slow

heat release, while, for rheological conversion curves $A_1 = 0$ is associated to the initial "induction" time of the phenomenon. A comparison of experimental conversion rates and those predicted by the model (Equation 2.4) is showed in Figure 2.7 and Figure 2.8, respectively, for calorimetric and rheological analyzes.

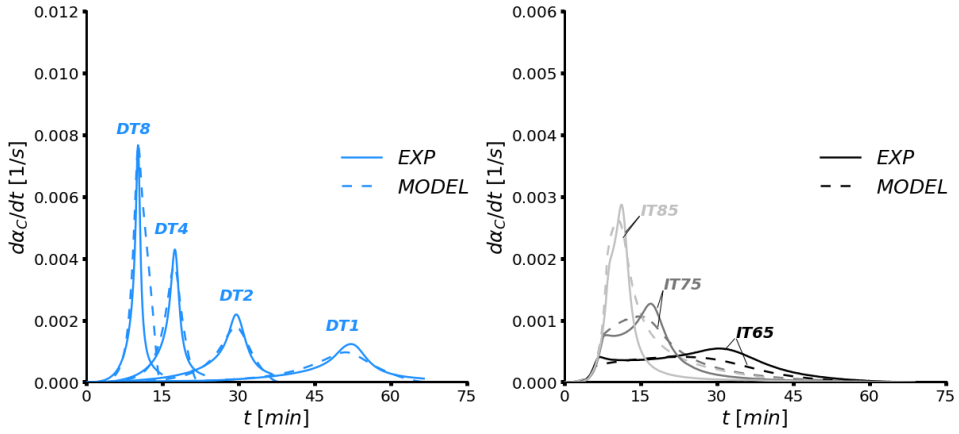


Figure 2.7: Comparison of experimental (continuous lines) and calculated (dashed lines) conversion rates from calorimetric analysis $d\alpha_C/dt$ vs time, t in (a) "dynamic conditions" DT and (b) "isothermal conditions" IT. Adapted from [50].

The prediction of the calorimetric conversions rate is in good agreement with the experimental curve in DT conditions, while, in IT conditions even though peak time and intensity dependency on the curing temperature is properly predicted by the model (the lower the temperature the longer the peak time and the lower the intensity), larger differences between the experimental and the predicted curves can be noted. This is not surprising as the model adopted refers to a single-step kinetics (one single activation energy, E) which is a hypothesis not fully verified, as explained in [50].

The prediction of the rheological conversion rate is in good agreement with experiments for all the thermal histories. Only the curve corresponding to the thermal history $DT8$ has a predicted peak higher that the experimental one, probably because the mean temperature of the specimen is lower than the temperature measured by the rheometer due to a delay in the heating of the core of the specimen. Thus, the actual process is slower

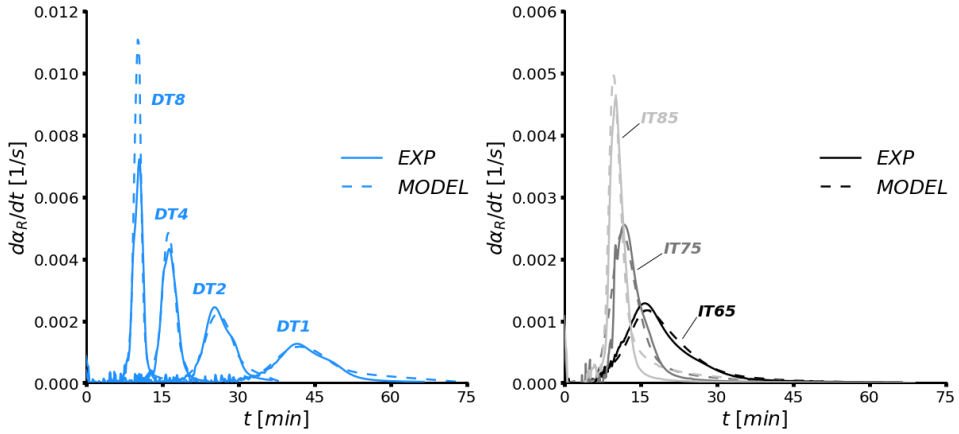


Figure 2.8: Comparison of experimental (continuous lines) and calculated (dashed lines) conversion rates from rheological analysis $d\alpha_R/dt$ vs time, t in (a) "dynamic conditions" DT and (b) "isothermal conditions" IT. Adapted from [50]

than the prediction made assuming a homogeneous heating of the whole specimen.

Conversion α was then calculated from the kinetic model by integration, taking into account the actual thermal history applied to the specimen. The initial heating ramp of the isothermal histories IT and the initial isothermal step at $25°C$ of the dynamic thermal histories DT have been considered, otherwise significant errors would have been found in the prediction of α. In particular, for DT experiments the following *ramp function* for temperature increase has been adopted:

$$T(t) = \dot{T}\,\frac{t - a + |t - a|}{2} + b \quad \text{with} \quad 0 \leq t \leq 4600\ s \tag{2.17}$$

where b is the initial temperature, a is the time during which the initial temperature is kept constant and $\dot{T}$ is the heating rate. In this work $b = 25°C$, $a = 60\ s$, $\dot{T} = 1, 2, 4, 8°C/min$. For IT experiments the following *ramp function* has been used:

$$T(t) = \dot{T}\,\frac{t - c - |t - c|}{2} + T_c \quad \text{with} \quad 60 \leq t \leq 4600\ s \tag{2.18}$$

where T_c is the curing temperature, c is the time to reach T_c and $\dot{T}$ is the

heating rate used to reach T_c. In this work $c = 370\ s$, $445\ s$, $515\ s$ for, respectively, $T_c = 65°C$, $75°C$, $85°C$ and $\dot{T} = 8°C/min$.

The prediction of α are compared to the experimental curves in Figure 2.9 and Figure 2.10 for calorimetric and rheological analysis, respectively.

Despite the differences in conversion rates observed in Figure 2.7, by

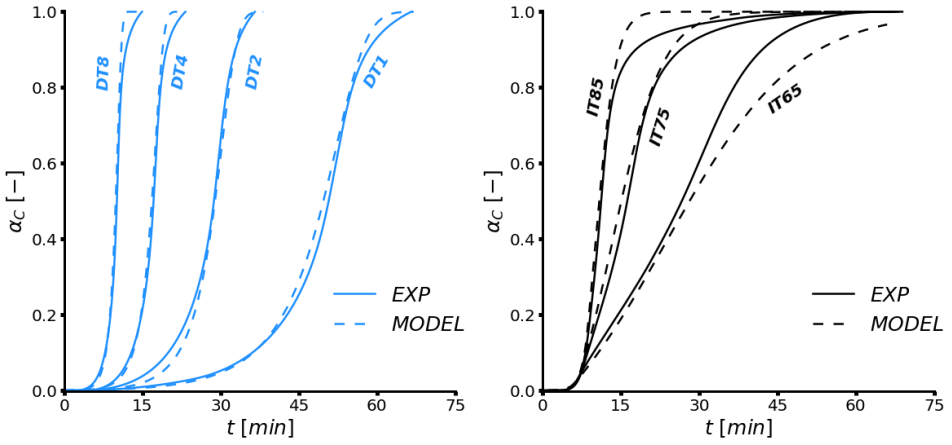


Figure 2.9: Comparison of experimental (continuous lines) and calculated (dashed lines) conversion from calorimetric analysis α_C vs time, t in (a) "dynamic conditions" DT and (b) "isothermal conditions" IT. Adapted from [50].

integrating, an accurate description of the calorimetric conversion α_C can be obtained (Figure 2.9) for all the thermal histories except $IT65$. Also the prediction of α_R (Figure 2.10) is very good for all the experiments. The deviation observable for $\alpha_C > 0.85$ and $\alpha_R > 0.9$, can be related to the fact that the mobility of the molecules changes in the final stage of the process, and therefore the kinetics is expected to be different from the one predicted by the model [29,53]. Furthermore, the model ability to predict the $DT8$ experiments, which was not considered for the parameters identification, confirms the model validity.

The use of a kinetic model allows to predict the evolution in time of the crosslinking process of any thermal history. Thus, the present kinetic model can be a useful tool to predict the processing time of the material in terms, for example, of gel point time and time to complete the crosslinking process. The potential of the kinetic model can be illustrated through the

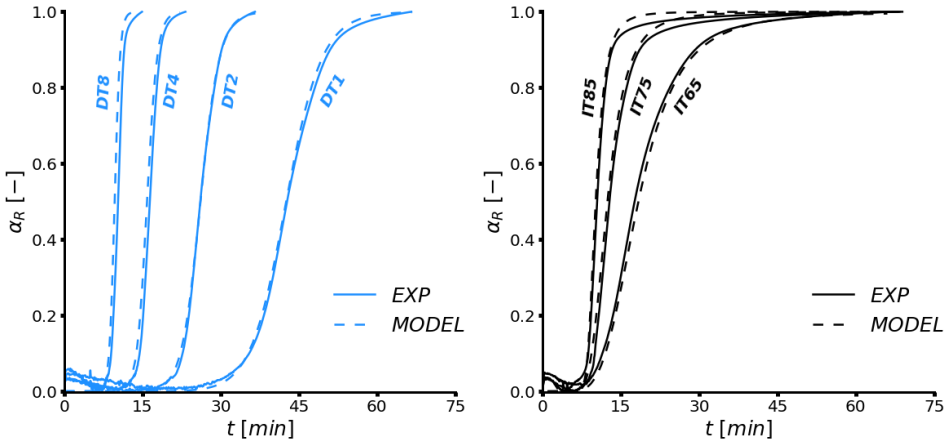


Figure 2.10: Comparison of experimental (continuous lines) and calculated (dashed lines) conversion from rheological analysis α_R vs time, t in (a) "dynamic conditions" DT and (b) "isothermal conditions" IT. Adapted from [50].

construction of iso-conversion curves maps. The maps allow to evaluate the time required to reach a defined conversion at a certain temperature, given a specific thermal history. They also highlight how both the heating rate and the temperature in isothermal curing affect the processability of the material. Figure 2.11 shows an iso-conversion curve map built from the kinetic model for the rheological curves. Three iso-conversion curves are plotted: $\alpha = 0.1$, which can be taken as an indicator of the beginning of reaction, $\alpha = 0.53$ which corresponds to the time in which the gel point is reached and $\alpha = 0.9$ which can indicate when the reaction is almost completed. For example, for an isothermal curing temperature $T_c = 75°C$, if the material is instantaneously heated up to T_c (thermal history c in Figure 2.11), $\alpha_R = 0.1$ is reached in only 3.5 min and $\alpha_R = 0.53$ (gel point) is reached in about 7 min. If the heating rate is $\dot{T} = 8°C/min$ (thermal history b in Figure 2.11), it takes about 8 min to reach $\alpha_R = 0.1$ and about 11 min to reach the gel point. If the heating rate is $\dot{T} = 2°C/min$ (thermal history a in Figure 2.11), the times are even longer. 25 min are necessary to reach a conversion $\alpha_R = 0.53$ (gel point) and the material reaches $\alpha_R = 0.1$ in about 21 min at a temperature of $67°C$ still during heating.

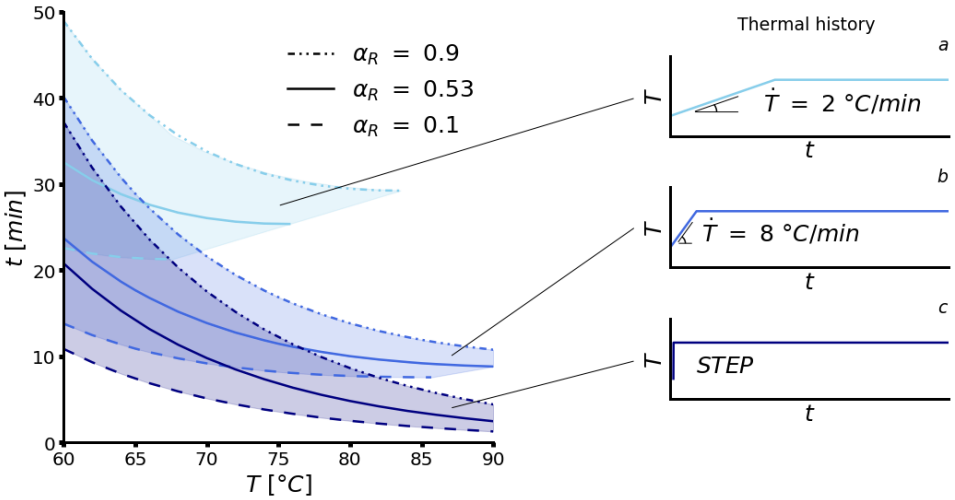
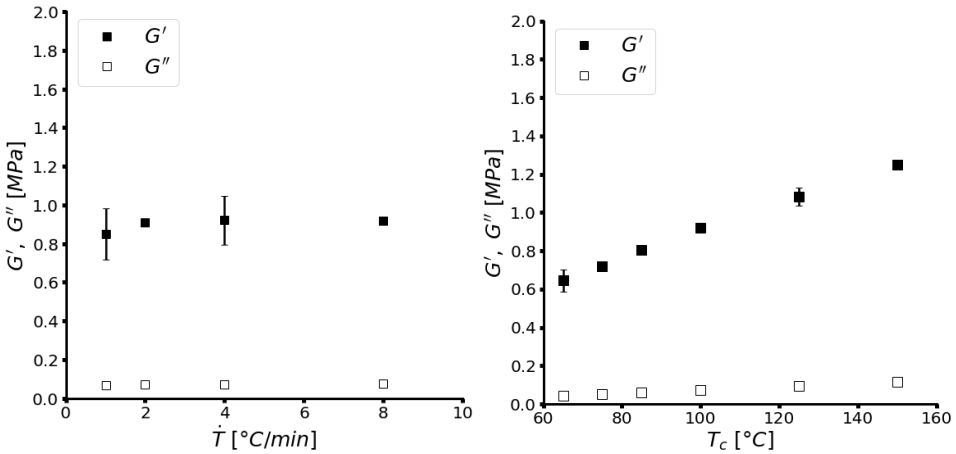


Figure 2.11: Temperature, T vs. time, t iso-conversion curves map for $\alpha_R = 0.1, 0.53, 0.9$. The illustrative map refers to isothermal curing conditions differing in the heating ramp. *a*: $\dot{T} = 2°C/min$, *b*: $\dot{T} = 8°C/min$, *c*: ideal step heating. Adapted from [50].

2.4.2 Crosslinking degree

After the study of the reaction kinetics, the next step was to assess the influence of the thermal history on the mechanical properties of the formed PDMS. For this analysis, the thermal histories reported in Figure 2.2 have been employed. Even if the rheological analysis performed allows to monitor the evolution in time of the shear moduli during the whole curing history, in this second part of the work, the attention was limited to the values of the moduli at the end of the applied thermal history. Figure 2.12 shows the conservative and the dissipative components G' and G'' measured at $25°C$ at the end of each thermal history, as a function of (a) the heating rate, $\dot{T}$ for thermal histories with curing temperature $T_c = 100°C$ (gray curves in Figure 2.2) and (b) the curing temperature, T_c for thermal histories whit heating rate $\dot{T} = 8°C/min$ (black curves in Figure 2.2). It is evident from Figure 2.12a that the heating rate has no significant effect on the properties of the cured PDMS. On the other hand, Figure 2.12b shows that the curing temperature has an evident influence on the PDMS mechanical properties. G' increases from $0.65 \pm 0.06\ MPa$, to $1.25 \pm 0.03\ MPa$ when T_c is increased from $65°C$ to $150°C$.

It it known from literature [20, 27, 28] that the structure of the network



(a) (b)

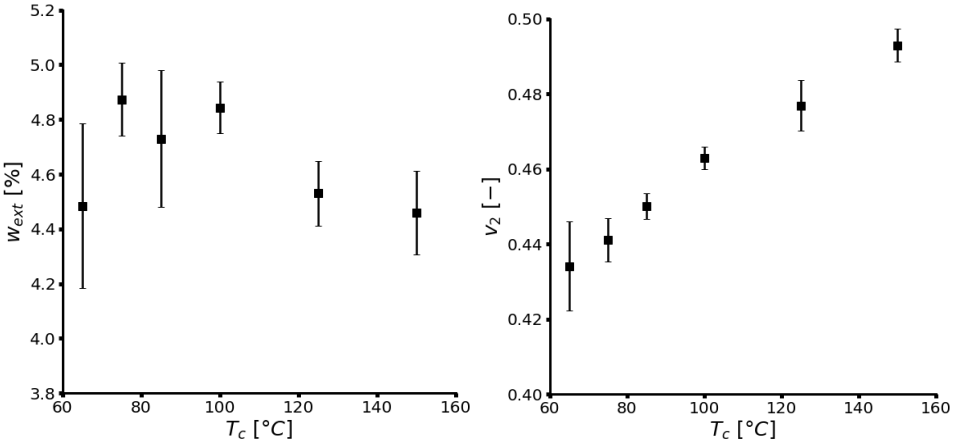
Figure 2.12: Conservative and dissipative components G' and G'' measured at 25°C, at the end of the each thermal history vs. (a) heating rate, $\dot{T}$ and (b) curing temperature T_c applied in the curing process.

and the mechanical properties of PDMSs are significantly affected by the thermal history applied during the crosslinking process. In this work, the influence of the thermal history has been split in two contributions: the effect of the heating rate and the effect of the curing temperature. The major contribution to the mechanical properties change is given by the curing temperature at which the crosslinking takes place, independently of the heating rate applied to reach this temperature in the first stages of the crosslinking. Since the dissipative component G'' is significantly lower than the conservative component G', the dissipative component of the modulus can be considered negligible. This PDMS displays therefore a behavior very close to that of an ideally elastic material. Hence, the values of the complex modulus $G^* = \sqrt{G'^2 + G''^2}$ have been considered a good approximation of the shear elastic modulus G of the PDMS and has been employed to calculate of the mean molecular weight between crosslinks, M_c according to Equation 2.10.

Subsequently, the samples obtained at the end of the thermal histories with different curing temperature (black curves in Figure 2.2) were employed to perform swelling tests as described in Section 2.3.5. Polymer extractable fraction, w_{ext} and volume fraction of polymer in the swollen network, v_2 have been calculated from the values of the initial mass of

the specimens m_0, the swollen specimens mass, m', and the mass of the dried specimens, m according to Equations 2.14 and 2.15, respectively. A table with all the measured masses can be found in a recently published paper [52].

Figure 2.13 reports the calculated values of the polymer extractable fraction, w_{ext} and the volume fraction of polymer in the swollen network, v_2 versus the curing temperature T_c. The extractable fraction (Figure



(a) (b)

Figure 2.13: (a) Polymer extractable fraction, w_{ext} and (b) Volume fraction of polymer in the swollen network, v_2 vs. curing temperature, T_c. Adapted from [52].

2.13a) seems not to be affected by the curing temperature and varies between 4% and 5%, with a mean value of 0.047 ± 0.002. On the contrary, as expected, the volume fraction of polymer in the swollen network v_2 increases with the curing temperature (Figure 2.13b). Higher temperatures have been showed to lead to the formation of stiffer PDMS (higher G', as showed in Figure 2.12b). This means that, according to the theory of rubber elasticity (Equation 2.10) the PDMS formed has higher density of crosslinks, corresponding to lower molecular weight between crosslinks. According to the theory of polymer systems, when a crosslinked polymer is immersed in a good solvent, the network absorbs the solvent until an equilibrium is reached and, in particular, the higher the density of crosslinks, the lower the amount of solvent absorbed. Consequently, the quantity of polymer in the swollen sample (v_2) is larger.

The mean molecular weight between crosslinks M_c was estimated from the volume fraction of polymer in the swollen network v_2 according to Equations 2.11, 2.12 and 2.13 as reported in Section 2.2.2. Figure 2.14 shows the comparison of the values of the mean molecular weight between crosslinks, M_c calculated from both rheological and swelling tests. The

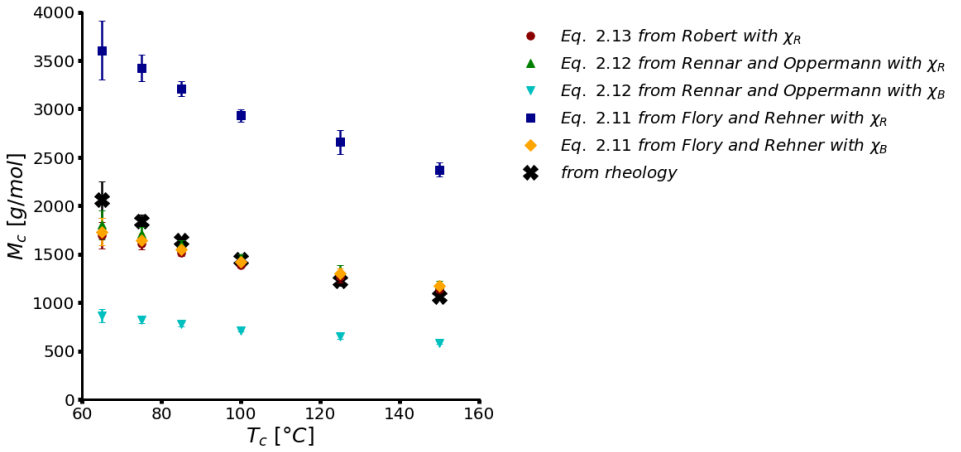


Figure 2.14: Mean molecular weight between crosslinks, M_c vs. curing temperature T_c. Black crosses represent data from rheological analysis and colored markers are data from swelling analysis. For the latter data, values obtained according to Equation 2.11 from Flory and Rehner, Equation 2.12 from Rennar and Oppermann and Equation 2.13 from Robert are reported. Adapted from [52].

values of M_c obtained from the swelling data depend strongly on both the equation and the solvent-polymer interaction parameter, χ adopted. The differences among the results arise from the different assumptions on which models are based [47,54]. It is beyond the purpose of this work to discuss about each model assumption validity for the material studied. The analysis is limited to the evaluation of the most appropriate theory based on the consistency of estimates from dynamic mechanical analysis and swelling experiments. As can be seen in Figure 2.14, the theory from Robert et al. [43] (red dots), the theory from Rennar and Oppermann [45] with the toluene-PDMS interaction parameter χ_R from Robert et al. [43] (green up triangles) and the theory from Flory and Rehner [44] with χ_B from Bueche [42] (orange diamonds) lead to very similar results. On the other hand, M_c from Rennar and Oppermann theory [45] with the toluene-PDMS interaction parameter χ_B from Bueche [42] (light blue down triangles) are significantly

lower than those from the theories just mentioned while the results of the analysis based on the theory from Flory and Rehner [44] with χ_R from Robert et al. [43] (blue squares) are significantly higher. Furthermore, M_c calculated from the elastic modulus (black crosses in Figure 2.14) are in good agreement with M_c obtained with the first three mentioned swelling models (red dots, green up triangles and orange diamonds in Figure 2.14). This result indicates that the theory from Rennar and Oppermann with χ_R, the theory from Flory and Rehner with χ_B and the theory from Robert et al. can be adopted to estimate M_c out of swelling experiments on the PDMS studied in this work.

2.5 Summary and conclusive remarks

In this work the crosslinking of the PDMS Sylgard®184 has been studied in terms of kinetics and final crosslinking degree. In particular, a kinetic model based on a modified version of the model proposed by Kamal has been adopted to predict the evolution of two conversions: one related to the evolution of the heat of reaction, measured by differential scanning calorimetry and one related to the evolution of the conservative component of the dynamic shear modulus measured by rheological analysis. Calorimetric and rheometric analyzes allowed to highlight different features of the process. The calorimetric characterization clearly showed the initial phases of the chemical reaction, while this detail was not captured by the rheometric observations. On the other hand, rheological analysis, that provide precise information about changes in the material mechanical properties, allowed to detect the gel point, which could not be identified by the calorimetric analysis. The rheological model can therefore be employed as useful tool for the proper design of the technology for the production of PDMS based products. The model allows, on one end, to predict the processing time, and therefore the time available for PDMS molding before crosslinking, and, on the other, to design an appropriate curing cycle for the preparation of the PDMS for a specific application.

This work allowed also to show that the thermal history applied to the material during the crosslinking process not only change the time to reach a fully crosslinked material but also influence the mechanical properties of the material. In particular, we showed that the temperature at which the

material is kept during the crosslinking process is more effective than the heating rate adopted to reach that temperature, for determining the final mechanical properties of the material. The mechanical properties of the PDMS have been correlated with the structure of the crosslinking network by mean of the theory of rubber elasticity and the mean molecular weight between crosslinks has been calculated. Additionally, swelling experiments have been performed and the mean molecular weight between crosslinks have been obtained according to different approaches proposed in literature. On the basis of the good agreement obtained between M_c calculated from the shear modulus and M_c calculated from some of the theory proposed, M_c estimates based on simple swelling experiments can be considered as a reliable tool to predict the shear modulus of the PDMS considered. This might simplify the material characterization after any curing cycle, since both a dynamometer and relatively large specimens with a proper shape are required to perform a mechanical test, while only a precision weighing scale balance is necessary for swelling measurements, and a small sample of any shape is suitable for this kind of measurements.

The present work has been carried out not only to study the crosslinking kinetics of the PDMS to characterize the material to be used for the production of an elastomeric matrix composite material whose characterization will be showed in Chapter 4, but it has been an in-depth study of the behavior of a PDMS and it is intended to provide quantitative information for all researchers designing applications employing the studied PDMS cured under certain conditions as a part of more complex structures. It is important to mention that we are aware that the present study refers to the properties at small strains and that PDMSs are elastomeric materials with high elongation at break with an elastic but non-linear behavior at large strains. The characterization at large strains has been carried out only on the material produced with the thermal history then used for the production of the composite material, and it is showed in Appendix A, but would be definitely interesting to investigate also how the thermal history applied influence the whole mechanical behavior of the material.

Chapter 3

Glass fibers characterization

3.1 Introduction

This chapter presents a brief discussion of the method used for the mechanical characterization of the glass fibers used in the production of the novel fiber-reinforced elastomer which characterization will be presented in Chapter 4. Indeed, the mechanical properties of fiber reinforced composites are strongly dependent on those of the matrix and those of the fibers. The properties of matrix and fibers are used as an input in composite models for predicting the mechanical behavior of composite materials and structures. The accurate determination of fiber and matrix mechanical behavior is therefore essential to give a reliable description of that of the composite. Firstly, for the analysis of the fiber volume fraction of the laminate produced, a density of the fibers of $2.66 \pm 0.004\ g/cm^3$ have been measured with a pycnometer Pycnomatic ATC Thermo Scientific, at $25°C$. Then, the elastic modulus of the fibers has been measured.

3.2 Theoretical background

Fiber tensile modulus is commonly determined by conducting single fiber quasi-static tensile tests using an appropriate experimental setup. The very small cross-sectional area of the fibers leads to a test procedure that requires special attention, especially regarding the measurement of the fiber cross-section, the fiber clamping and its alignment to the loading direction [55]. In addition, due to the high stiffness of the fiber, a specific

procedure has to be followed to eliminate the possible contribution of the test system compliance on the measurement of the mechanical properties of the fiber as described in the ASTM C1557 - 20 - Standard Test Method for Tensile Strength and Young's Modulus of Fibers [56].

The method to evaluate the Young modulus and the system compliance suggested by [56] is as follows. Quasi-static tensile tests on single fibers with at least three different gauge length are needed. Considering the system compliance as the inverse of the force constant k of a spring [56], the gap between the clamps L_t, measured by the testing machine during the tensile test, can be assumed as the sum of the different contributions represented in Figure 3.1:

$$L_t = L_0 + \Delta L + k^{-1}F \tag{3.1}$$

where L_0 is the initial length of the fiber, ΔL is the elongation of the single fiber, k is the spring constant (the inverse of the system compliance) and F the force measured by the testing machine.

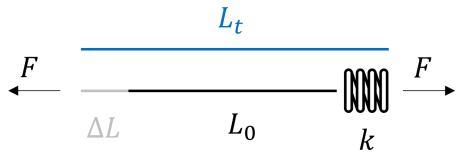


Figure 3.1: Schematic diagram showing contributions in the gap measurement. L_t is the gap between the clamps, L_0 is the initial length of the fiber, ΔL is the elongation of the single fiber, k is the spring constant and F the force measured by the testing machine.

Considering the case of a linear elastic material, according to the Hooke's law the real strain of the tested fiber, ε, that is the ratio between the elongation of the fiber and its initial length, can be calculated as:

$$\varepsilon = \frac{\Delta L}{L_0} = \frac{F}{AE} \tag{3.2}$$

where A is the cross-section of the tested fiber and E is the Young modulus

of the fiber. Combining Equations 3.1 and 3.2 the following equation can be derived:

$$\frac{L_t - L_0}{F} = \frac{L_0}{AE} + k^{-1} \tag{3.3}$$

Therefore, a plot of $(L_t - L_0)/F$ (that is, the inverse of the slope of the force versus cross-head displacement) versus L_0/A will yield a straight line with constant slope of $1/E$ and intercept k^{-1}. Thus, this method allows to measure the Young modulus of stiff fibers eliminating the possible errors caused by the compliance of the measurement system.

3.3 Methods

Quasi-static tensile tests have been performed with a DMA TA RSA III instrument operating in quasi-static mode. This instrument was chosen because it was the only one available in our laboratory with sufficient sensitivity to measure forces of the order of 10^{-3} N. This instrument includes a clamping tool specific for fibers tensile test that allows to align the fiber along the loading direction.

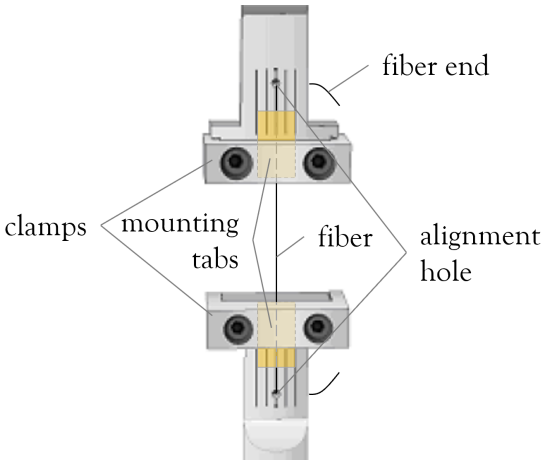


Figure 3.2: A schematic of the mounting system for quasi-static tensile test of single glass fibers.

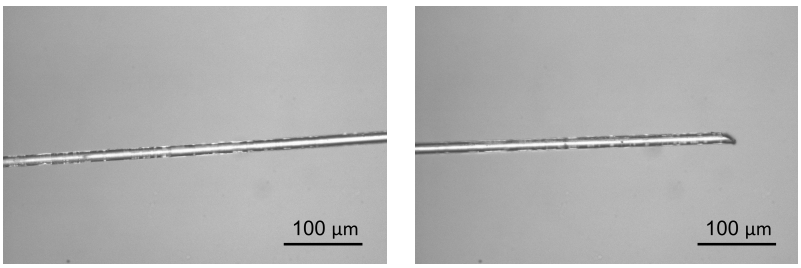
Samples with gauge lengths of about $15, 25, 40$ and 60 mm have been prepared. Single fibers (six samples for each gauge length) with length at least three times longer than the desired gauge length, were randomly extracted from a bundle. Then, with the help of a graph paper support,

two tabs were prepared and positioned in the central part of the fiber, to hold a section of the fiber with desired gauge length, while the two ends extended out of the tabs allow the alignment of the fiber when inserted in the clamping system. For each fiber, three optical microscope images of different parts of the gauge length were taken and the fiber diameter measurement was obtained. The fiber, prepared as described above, was then positioned in the testing machine by inserting the two ends into two holes specifically design to align the fiber along the loading direction, and then closing the two mounting tabs in the clamps. A schematic of the clamping system as described above can be seen in Figure 3.2. The tests have been conducted under displacement control, at constant cross-head displacement rate of 8 $\mu m/s$, as suggested by [56].

3.4 Results and discussion

3.4.1 Optical analysis

An Olympus BX-60 optical microscope in bright field configuration with a magnification level of 20x has been used to collect the images of the single fibers before and, when the fiber was not totally disintegrated, after the tensile test. An example of optical images of a single fiber before and after the test is showed in Figure 3.3.

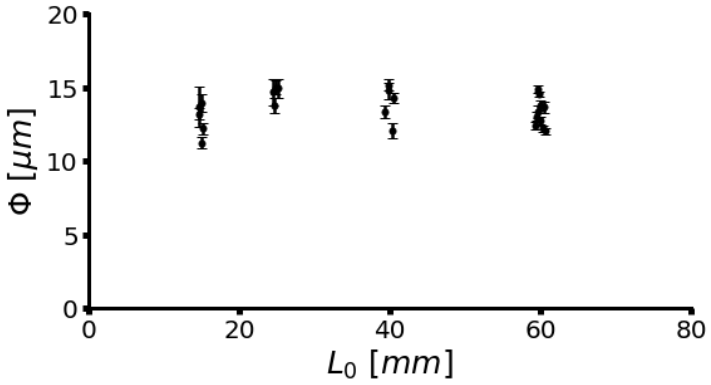


(a) (b)

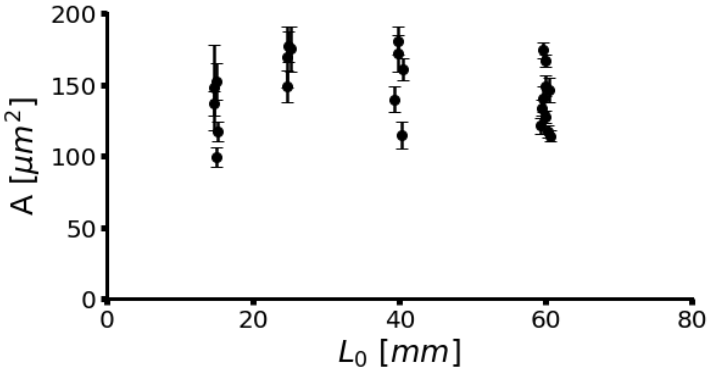
Figure 3.3: (a) Optical image of a single glass fiber before testing. (b) Optical image of a single fiber after testing.

ImageJ software has been used as image processing program to analyze the images and measure the diameter of the fibers. To measure the diameter of each fiber, three images per fiber have been taken, then six measures

per image have been performed, and the resulting eighteen measures have been averaged. Figure 3.4a and b shows, respectively, the distribution of fibers diameters and fibers areas versus the gauge length of all the tested fibers. Overall, the diameter of the fibers ranges between 11 and 15 μm and the fibers area ranges between 99 and 181 μm^2.



(a)



(b)

Figure 3.4: (a) Distribution of fibers diameter, Φ versus gauge length, L_0. (b) Distribution of fibers area, A versus gauge length, L_0.

3.4.2 Mechanical tests

The results of the quasi-static tensile tests as force versus cross-head displacement plots, are shown in Figure 3.5. The curves are straight lines (expected behavior for glass fibers [1]) up to about 0.20 N then tend to deviate from linearity. This can be attributed to a slight slippage of the fiber in the clamps. For this reason, only the curves up to $F = 0.20$ N are

considered. In order to calculate the system compliance and the Young modulus as explained in Section 3.2, the cross-head displacement $L_t - L_0$ (x axis of plots in Figure 3.5) has been extracted for discrete values of force (y axis of plots in Figure 3.5) $F = 0.05$, 0.10, 0.15 and 0.20 N and the values $(L_t - L_0)/F$ and L_0/A have been calculated for each tested fiber.

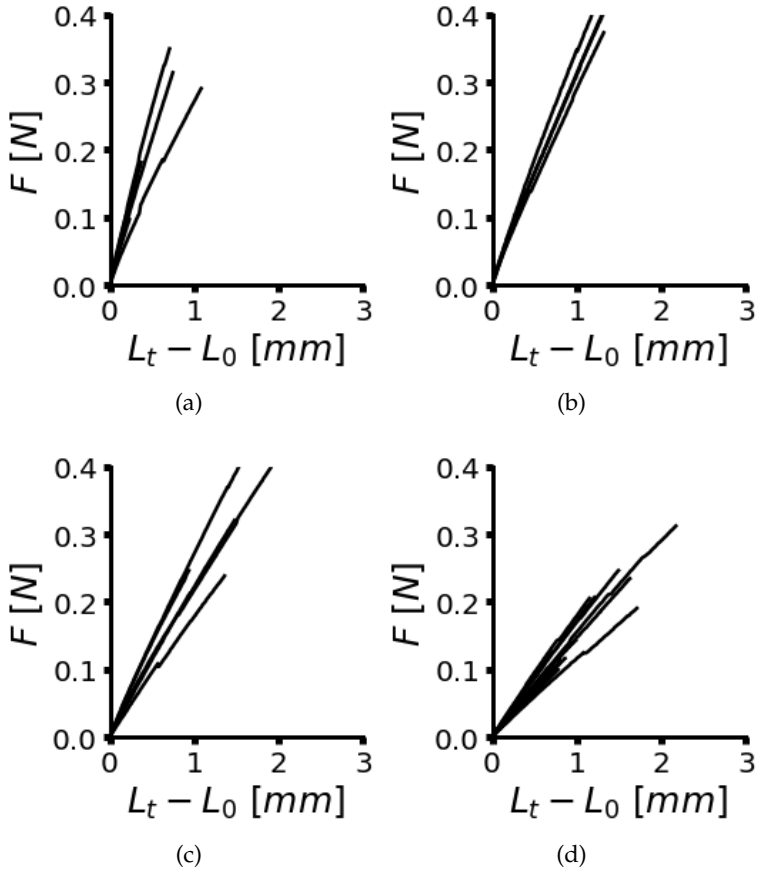


Figure 3.5: Force versus cross-head displacement curves. Approximate fiber gauge length: (a) about 15 mm, (b) about 25 mm, (c) about 40 mm, (d) about 60 mm.

Figure 3.6 shows the plots of $(L_t - L_0)/F$ versus L_0/A for the different values of F considered. As can be seen, the experimental points (black dots) are placed in a straight line, thus, the slope of the line obtained with a linear fitting can be taken as the inverse of the Young modulus $1/E$ and the intercept can be taken as the system compliance k^{-1}.

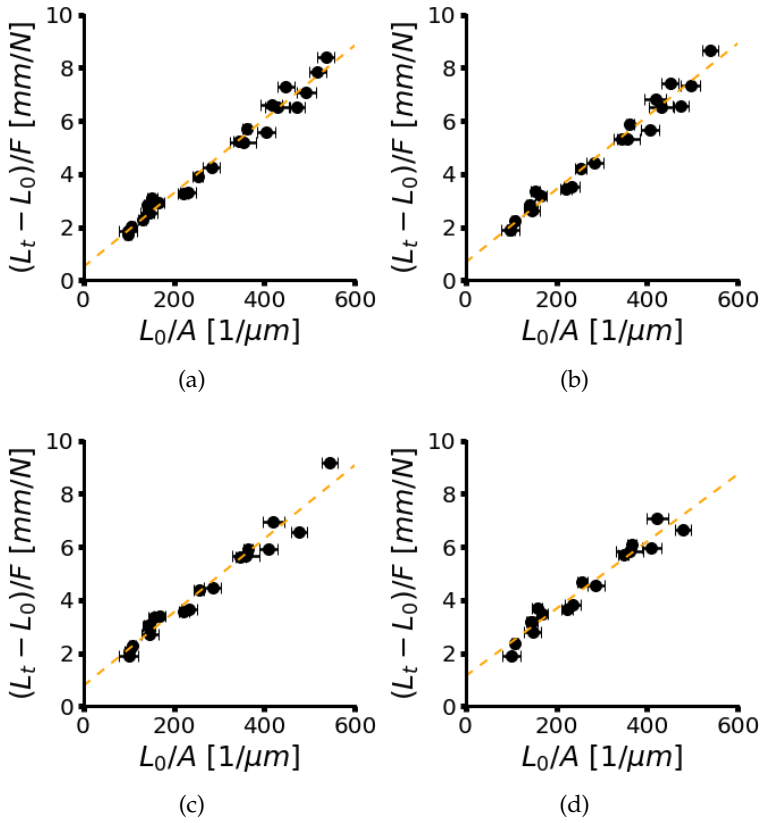


Figure 3.6: Plot of $(L_t - L_0)/F$ versus L_0/A for (a) $F = 0.05\ N$, (b) $F = 0.10\ N$, (c) $F = 0.15\ N$, (d) $F = 0.20\ N$. The dashed lines represent the linear fitting.

Table 3.1 summarizes the values of Young modulus E and system compliance k^{-1}.

Table 3.1: System compliance, k^{-1} and Young modulus, E calculated at different values of force, F.

$F\ [N]$	$k^{-1}\ [mm/N]$	$E\ [GPa]$
0.05	0.49 ± 0.14	71.79 ± 2.31
0.10	0.66 ± 0.17	72.66 ± 2.88
0.15	0.76 ± 0.21	72.09 ± 3.67
0.20	1.13 ± 0.22	78.90 ± 4.91

The system compliance increases progressively with F probably due to a slight slippage of the fiber during the test, which results in increasing system compliance as the force increases. Slippage, however, does not influence the modulus value calculated for $F \leq 0.15\ N$, therefore, the average of the modulus calculated for $F \leq 0.15\ N$, $E_{av} = 72.18\ GPa$ can be considered a reliable measurement of the property of the single fiber.

3.5 Summary and conclusive remarks

In this chapter a simple method for measuring the Young modulus of glass fibers has been showed. The Young modulus of glass fibers is not trivial to measure due to the small diameter of the fiber and its high stiffness. This procedure, inspired to the standard ASTM C1557 - 20 [56], allows to measure it without the support of any complicated equipment. The Young modulus of the glass fibers has been measured for the preliminary characterization of the glass fibers which have been then used to manufacture the GF-PDMS soft composite. In future discussions, an average value of 72 GPa will be adopted as Young modulus of the considered glass fibers.

Chapter 4

GF - PDMS composite

4.1 Introduction

After introducing in the previous chapters the properties of matrix and fiber taken individually, this chapter will report the production and characterization of glass fiber-reinforced polydimethylsiloxane (GF-PDMS) laminates.

In Section 4.2, a brief theoretical background will be given to introduce the concepts necessary to understand the results of the characterization. The principal micromechanical models employed will be introduced and a brief introduction to the Classical Lamination Theory, that is at the foundation of laminate design, will be given.

In Section 4.3 the methods employed for laminates production will be explained and some micrographs will be displayed.

Section 4.4 will be focused on the characterization of single lamina behavior at small strains in which the material response can be considered linear elastic. The experimental tests employed to determine the four elastic constants E_1, E_2, ν_{12} and G_{12} characteristic of a lamina will be described. The characterization of laminae with different fiber volume fraction will be showed and the experimental values of the four properties will be compared with the predictions of micromechanical models widely adopted in literature for the description of laminates. The differences between these elastomeric matrix laminates and traditional laminates will be underlined.

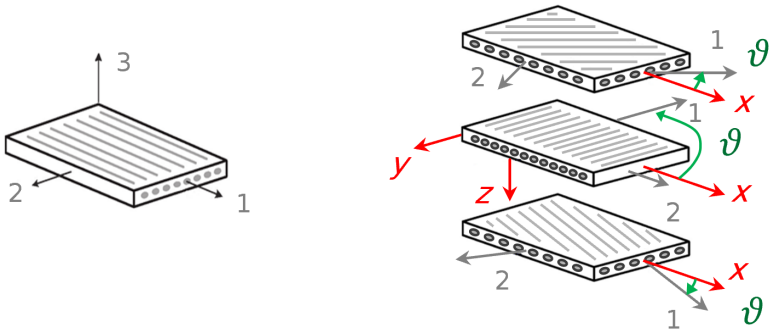
In Section 4.5, the large strains behavior, strongly non-linear, of symmetric-balanced angle ply laminates with different fiber orientation will be presented.

Finally, Section 4.6 will show the behavior of antisymmetric laminates with particular attention to the load coupling effects that can be obtained with the selected stacking sequence. A specially designed test setup will be employed to measure the extension-twist coupling and the experimental results will be compared with those predicted by Classical Lamination Theory and simple finite element analyzes.

4.2 Theoretical background

In a composite material two or more materials are combined on a macroscopic scale to form a useful third material. The advantage of composite materials is that, if well designed, they usually exhibit the best qualities of their components or constituents and often some qualities that cannot be achieved with any of the constituents alone. In fiber-reinforced composite materials, fibers are the principal load-carrying members, while the matrix material keeps the fibers together and acts as a load transfer medium between them. Fiber-reinforced composite materials are often made in the form of a thin layer, called lamina, containing fibers aligned in the same direction. A typical lamina along with its principal material axes parallel and perpendicular to the fiber direction is showed in Figure 4.1a. Starting from laminae, laminates are formed as bonded stack of laminae with various orientations of principal material directions with respect to the laminate principal axis as in Figure 4.1b. In this work, x, y and z will be always the principal directions in the laminate reference system, respectively x along the length of the laminate, y along the width of the laminate and z along its thickness. While 1, 2 and 3 will be the principal directions of the lamina, respectively 1 will be the direction of the fibers, 2 the second direction in the plane of the lamina perpendicular to the fibers and 3 the direction along its thickness.

Composite materials have many mechanical behavior characteristics that are different from those of more conventional *homogeneous* and *isotropic* materials. A homogeneous body has uniform properties, an *isotropic* body has material properties that are the same in every direction at a point in the body [1]. In contrast, composite materials are often both *inhomogeneous* and *anisotropic*, that means respectively that the properties depend on the position in the body and are different in all directions at a point in the



(a) (b)

Figure 4.1: (a) A lamina along with its principal material axes 1, 2 and 3. (b) Laminate formed as bonded stack of laminae with various orientations of principal material directions with respect to the laminate principal axis x, y and z.

body: no planes of material property symmetry exist. Because of the heterogeneous nature of composite materials, they are conveniently studied from two points of view [1]:

- Macromechanics, which is the study of composite material behavior in which the material is assumed to be homogeneous and the effects of the constituent materials are detected only as an average of the apparent macroscopic properties of the composite material.
- Micromechanics, which is the study of composite material behavior in which the interaction of constituent materials is examined on a microscopic scale.

Typically, in order to study the mechanical behavior of a laminate (two or more laminae connected to act as integral element), the properties of a single lamina are defined and then combined by means of the Classical Lamination Theory (CLT). An overview of the macromechanical behavior of a single lamina will be given in Section 4.2.1. The micromechanical approach adopted to homogenize the fundamental properties necessary to describe the lamina behavior will be show in Section 4.2.2 and an introduction to the Classical Lamination Theory will be given in Section 4.2.3.

4.2.1 Macromechanical behavior of a lamina

The study of the macromechanical behavior considers the averaged apparent mechanical properties of a body. The mechanical behavior of a material can be described through its stiffness matrix or its compliance matrix, that is the constitutive equations that relates stress to strain or vice versa. The compliance matrix of a general *anisotropic* material is symmetric [1] and therefore has 21 independent constants:

$$\begin{bmatrix} \varepsilon_1 \\ \varepsilon_2 \\ \varepsilon_3 \\ \gamma_{23} \\ \gamma_{31} \\ \gamma_{12} \end{bmatrix} = \begin{bmatrix} S_{11} & S_{12} & S_{13} & S_{14} & S_{15} & S_{16} \\ & S_{22} & S_{23} & S_{24} & S_{25} & S_{26} \\ & & S_{33} & S_{34} & S_{35} & S_{36} \\ & & & S_{44} & S_{45} & S_{46} \\ & & & & S_{55} & S_{56} \\ & & & & & S_{66} \end{bmatrix} \begin{bmatrix} \sigma_1 \\ \sigma_2 \\ \sigma_3 \\ \tau_{23} \\ \tau_{31} \\ \tau_{12} \end{bmatrix} \tag{4.1}$$

If three orthogonal planes of symmetry exist, the number of independent material constants reduces to 9. The material is called *orthotropic* and the stress-strain relation becomes:

$$\begin{bmatrix} \varepsilon_1 \\ \varepsilon_2 \\ \varepsilon_3 \\ \gamma_{23} \\ \gamma_{31} \\ \gamma_{12} \end{bmatrix} = \begin{bmatrix} S_{11} & S_{12} & S_{13} & 0 & 0 & 0 \\ & S_{22} & S_{23} & 0 & 0 & 0 \\ & & S_{33} & 0 & 0 & 0 \\ & & & S_{44} & 0 & 0 \\ & & & & S_{55} & 0 \\ & & & & & S_{66} \end{bmatrix} \begin{bmatrix} \sigma_1 \\ \sigma_2 \\ \sigma_3 \\ \tau_{23} \\ \tau_{31} \\ \tau_{12} \end{bmatrix} \tag{4.2}$$

In order to give a more direct meaning to the compliance matrix, the components of the compliance matrix can be written in terms of engineering constants:

$$\left[S_{ij}\right] = \begin{bmatrix} \frac{1}{E_1} & -\frac{\nu_{21}}{E_2} & -\frac{\nu_{31}}{E_3} & 0 & 0 & 0 \\ -\frac{\nu_{12}}{E_1} & \frac{1}{E_2} & -\frac{\nu_{32}}{E_3} & 0 & 0 & 0 \\ -\frac{\nu_{13}}{E_1} & -\frac{\nu_{23}}{E_2} & \frac{1}{E_3} & 0 & 0 & 0 \\ 0 & 0 & 0 & \frac{1}{G_{23}} & 0 & 0 \\ 0 & 0 & 0 & 0 & \frac{1}{G_{31}} & 0 \\ 0 & 0 & 0 & 0 & & \frac{1}{G_{12}} \end{bmatrix} \tag{4.3}$$

where E_1, E_2 and E_3 are the Young's moduli respectively in direction 1, 2 and 3. ν_{ij} are the Poisson's ratio (also referred to as extension-extension

coupling coefficient) defined as: $\nu_{ij} = -\varepsilon_j/\varepsilon_i$ for $\sigma_i = \sigma$ and all the other stresses equal to zero. G_{23}, G_{31} and G_{12} are the shear moduli respectively in the planes 2-3, 3-1 and 1-2. Recalling that for symmetry $[S_{ij}] = [S_{ji}]$,

$$\frac{\nu_{ij}}{E_i} = \frac{\nu_{ji}}{E_j} \qquad i,j = 1,2,3 \qquad i \neq j \tag{4.4}$$

Thus, irrespective of the values of E_i and E_j, the transverse strain is the same when the stress in applied in the j-direction as when it is applied in the i-direction. This means that, for example, if $E_1 \gg E_2$ as in the case of soft matrix fiber-reinforced composites, $\nu_{12} \gg \nu_{21}$.

If at every point of a material there is one plane in which the mechanical properties are equal in all directions, then the material is called *transversely isotropic* and the stress-strain relation has only five independent constants:

$$\begin{bmatrix} \varepsilon_1 \\ \varepsilon_2 \\ \varepsilon_3 \\ \gamma_{23} \\ \gamma_{31} \\ \gamma_{12} \end{bmatrix} = \begin{bmatrix} \frac{1}{E_1} & \frac{\nu_{21}}{E_2} & \frac{\nu_{21}}{E_2} & 0 & 0 & 0 \\ \frac{\nu_{12}}{E_1} & \frac{1}{E_2} & \frac{\nu_{32}}{E_2} & 0 & 0 & 0 \\ \frac{\nu_{12}}{E_1} & \frac{\nu_{23}}{E_2} & \frac{1}{E_2} & 0 & 0 & 0 \\ 0 & 0 & 0 & \frac{1}{G_{23}} & 0 & 0 \\ 0 & 0 & 0 & 0 & \frac{1}{G_{12}} & 0 \\ 0 & 0 & 0 & 0 & & \frac{1}{G_{12}} \end{bmatrix} \begin{bmatrix} \sigma_1 \\ \sigma_2 \\ \sigma_3 \\ \tau_{23} \\ \tau_{31} \\ \tau_{12} \end{bmatrix} \tag{4.5}$$

If a plane stress state is defined by setting

$$\sigma_3 = 0 \quad \tau_{23} = 0 \quad \tau_{31} = 0 \tag{4.6}$$

so that

$$\sigma_1 \neq 0 \quad \sigma_2 \neq 0 \quad \tau_{12} \neq 0 \tag{4.7}$$

It can be demonstrated [1] that Equation 4.5 reduces to:

$$\begin{bmatrix} \varepsilon_1 \\ \varepsilon_2 \\ \gamma_{12} \end{bmatrix} = \begin{bmatrix} S_{11} & S_{12} & 0 \\ S_{12} & S_{22} & 0 \\ 0 & 0 & S_{66} \end{bmatrix} \begin{bmatrix} \sigma_1 \\ \sigma_2 \\ \tau_{12} \end{bmatrix}$$

$$or \tag{4.8}$$

$$\begin{bmatrix} \varepsilon_1 \\ \varepsilon_2 \\ \gamma_{12} \end{bmatrix} = \begin{bmatrix} \frac{1}{E_1} & \frac{\nu_{21}}{E_2} & 0 \\ -\frac{\nu_{12}}{E_1} & \frac{1}{E_2} & 0 \\ 0 & 0 & \frac{1}{G_{12}} \end{bmatrix} \begin{bmatrix} \sigma_1 \\ \sigma_2 \\ \tau_{12} \end{bmatrix}$$

where the matrix that relates stresses to strains, abbreviated $[S_{12}]$, is the reduced compliance matrix.

If we consider Equation 4.4, to describe the constitutive equation of a *transversely isotropic* material in a plane stress state four independent material properties (E_1, E_2, ν_{12} and G_{12}) are needed. By definition, a lamina can be considered a *transversely isotropic* material in a plane stress state. Hence, in this work, in order the mechanically characterize the behavior of the GF-PDMS lamina at small strains, the material properties E_1, E_2, ν_{12} and G_{12} will be measured.

If there is an infinite number of planes of symmetry the constitutive equation will simplify to the one of *isotropic* material described by only two independent constants, that can be the Young's modulus E and the Poisson's ratio ν or the shear modulus G, that can be used as an alternative to either Young's modulus or Poisson's ratio. They are related by the following equation [1]:

$$G = \frac{E}{2(1+\nu)} \tag{4.9}$$

Focusing on the lamina's behavior, note that Equation 4.8 relates stresses and strains of an *transversely isotropic* lamina, when the principal material coordinates, local coordinates 1, 2 and 3, coincide with the coordinate direction in which the mechanical problem has to be solved x, y, and z. When, on the contrary, the local coordinates do no coincide with the global coordinates of the system, a method of transforming stress-strain relations from one coordinate system to another is needed. From elementary mechanics of materials it is possible to express stresses and strains in a $1-2$ coordinates system in terms of stresses and strains in a $x-y$ coordinates system, rotated by an angle ϑ (See Figure 4.1b), by means of the following transformation equations:

$$\begin{bmatrix} \sigma_1 \\ \sigma_2 \\ \tau_{12} \end{bmatrix} = [T] \begin{bmatrix} \sigma_x \\ \sigma_y \\ \tau_{xy} \end{bmatrix} \tag{4.10}$$

$$\begin{bmatrix} \varepsilon_1 \\ \varepsilon_2 \\ \frac{\gamma_{12}}{2} \end{bmatrix} = [T] \begin{bmatrix} \varepsilon_x \\ \varepsilon_y \\ \frac{\gamma_{xy}}{2} \end{bmatrix} \tag{4.11}$$

where

$$[T] = \begin{bmatrix} cos^2(\vartheta) & sin^2(\vartheta) & 2sin(\vartheta)cos(\vartheta) \\ sin^2(\vartheta) & cos^2(\vartheta) & -2sin(\vartheta)cos(\vartheta) \\ -sin(\vartheta)cos(\vartheta) & sin(\vartheta)cos(\vartheta) & cos^2(\vartheta) - sin^2(\vartheta) \end{bmatrix} \tag{4.12}$$

If the simple matrix

$$[R] = \begin{bmatrix} 1 & 0 & 0 \\ 0 & 1 & 0 \\ 0 & 0 & 2 \end{bmatrix} \tag{4.13}$$

is introduced, the conventional engineering strain vectors

$$\begin{bmatrix} \varepsilon_1 \\ \varepsilon_2 \\ \gamma_{12} \end{bmatrix} = [R] \begin{bmatrix} \varepsilon_1 \\ \varepsilon_2 \\ \frac{\gamma_{12}}{2} \end{bmatrix} \qquad \begin{bmatrix} \varepsilon_x \\ \varepsilon_y \\ \gamma_{xy} \end{bmatrix} = [R] \begin{bmatrix} \varepsilon_x \\ \varepsilon_y \\ \frac{\gamma_{xy}}{2} \end{bmatrix} \tag{4.14}$$

can be used in the stress-strain transformations. Applying these transformations to Equation 4.8, it is possible to relate stresses to strains in any coordinate system:

$$\begin{bmatrix} \varepsilon_x \\ \varepsilon_y \\ \gamma_{xy} \end{bmatrix} = [R][T]^{-1}[R]^{-1}[S][T] \begin{bmatrix} \sigma_x \\ \sigma_y \\ \tau_{xy} \end{bmatrix} = \begin{bmatrix} \overline{S_{11}} & \overline{S_{12}} & \overline{S_{16}} \\ \overline{S_{21}} & \overline{S_{22}} & \overline{S_{26}} \\ \overline{S_{61}} & \overline{S_{62}} & \overline{S_{66}} \end{bmatrix} \begin{bmatrix} \sigma_x \\ \sigma_y \\ \tau_{xy} \end{bmatrix} \tag{4.15}$$

where the matrix that relates stresses to strains, abbreviated $[\overline{S_{12}}]$, is the transformed reduced compliance matrix and it has terms in all nine positions in contrast to the presence of zeros in the reduced compliance matrix $[S_{12}]$.

Similarly, it is possible to relate strains to stresses through the inverse matrix, that is the transformed reduced stiffness matrix $[\overline{Q_{12}}]$:

$$\begin{bmatrix} \sigma_x \\ \sigma_y \\ \tau_{xy} \end{bmatrix} = \begin{bmatrix} \overline{Q_{11}} & \overline{Q_{12}} & \overline{Q_{16}} \\ \overline{Q_{21}} & \overline{Q_{22}} & \overline{Q_{26}} \\ \overline{Q_{61}} & \overline{Q_{62}} & \overline{Q_{66}} \end{bmatrix} \begin{bmatrix} \varepsilon_x \\ \varepsilon_y \\ \gamma_{xy} \end{bmatrix} \tag{4.16}$$

This lead to further important considerations. In the case of *orthotropic* material, if the local coordinates system coincides with the global coordinate system there is no interaction between normal stresses σ_1, σ_2 and σ_3 and shearing strains γ_{23}, γ_{31} and γ_{12} (null value of the upper right corner of 4.2). For example, in *orthotropic* materials, the application of a normal stress in a principal material direction results in extension in the direction of the stress and contraction perpendicular to the stress. The magnitude of the extension in one principal material direction under normal stress in that direction is different from the extension in another principal material direction under the same normal stress in that other direction. Thus, different Young's moduli exist in the various principal material directions. In addition, different Poisson's ratios are associated with different pairs of principal material directions and the application of shear stress causes shearing deformation, but the magnitude of the shearing deformation is totally independent of the various Young's moduli and Poisson's ratios.

Instead, for *anisotropic* materials, or *orthotropic* material if the local coordinates system does not coincide with the global coordinates system, the application of a normal stress leads not only to extension in the direction of the stress and contraction perpendicular to it, but also to shearing deformation. Conversely, application of shearing stress causes extension and contraction in addition to the distortion of shearing deformation. Thus, significant coupling occurs between the applied stress and the various strain responses. In particular, the terms $\overline{S_{11}}$, $\overline{S_{22}}$ represent extensional response to an individual applied stress, σ_x and σ_y. The term $\overline{S_{66}}$ represents shear strain response to an applied shear stress in the same plane. The term $\overline{S_{12}}$ represents the extension-extension coupling. The terms $\overline{S_{16}}$ and $\overline{S_{26}}$ represent normal strain response to applied shear stress (shear-extension coupling).

Another consideration that has to be done is that when stress- strain relations are considered, the engineering constants must also satisfy certain constrictions. For example, for *isotropic* material, the Poisson's ratio is restricted to the range

$$-1 < \nu < \frac{1}{2} \tag{4.17}$$

in order that shear or hydrostatic loading does not produce negative strain

energy. For *orthotropic* materials the relations between engineering constants are more complex. They are all related to the thermodynamic constraints which hinder the non-physical generation of energy. The constraints for *orthotropic* materials were generalized by Lempriere and are well explained in [57]. Among the other, the following condition must be satisfied:

$$|\nu_{ij}| < \sqrt{\frac{E_i}{E_j}} \tag{4.18}$$

which implies that, for *orthotropic* materials, even values much greater than $1/2$ are accepted Poisson's ratio, and the value increases as the difference between E_1 and E_2 increases.

4.2.2 Micromechanical behavior of a lamina

Micromechanics is intended to find the relationship of the composite material properties to the properties of the constituents, in order to predict the properties of the lamina starting from the one of the fibers and of the matrix [1]. The main assumption on which it is based is that the strains in the fiber direction are the same in the fibers as in the matrix. On this assumption, the material constants (E_1, E_2, ν_{12} and G_{12}) of a lamina will be determined in terms of the elastic modulus E_f and the Poisson's ratio ν_f of the fibers, the elastic modulus E_m and the Poisson's ratio ν_m of the matrix and their relative volume. If a lamina of length L and width w is elongated along the fibers direction, it will deform with a total strain ε_1:

$$\varepsilon_1 = \frac{\Delta L}{L} \tag{4.19}$$

If the constituents materials behave elastically, the fiber and matrix stresses in the fibers direction, respectively σ_f and σ_m are:

$$\sigma_f = E_f\, \varepsilon_1 \qquad \sigma_m = E_m\, \varepsilon_1 \tag{4.20}$$

Calling A the cross-sectional area of the lamina, A_f the cross-sectional area of the fibers and A_m the cross-sectional area of the matrix, the resultant force F on the lamina is:

$$F = \sigma_1\, A = \sigma_f\, A_f + \sigma_m\, A_m \tag{4.21}$$

Substituting Equation 4.20 in Equation 4.21 and recalling that $\sigma_1 = E_1\ \varepsilon_1$:

$$E_1 = E_f\ \frac{A_f}{A} + E_m\ \frac{A_m}{A} \tag{4.22}$$

The volume fraction of fibers and matrix can be written as:

$$v_f = \frac{A_f}{A} \qquad v_m = \frac{A_m}{A} \tag{4.23}$$

Thus,

$$E_1 = E_f\ v_f + E_m\ v_m \tag{4.24}$$

Equation 4.24 is known as the *rule of mixtures* of the apparent Young's modulus of the composite material in the direction of the fibers, and can be seen also as a simple *spring-in-parallel* model [1].

The major Poisson's ratio ν_{12} is obtained by an approach similar to the analysis for E_1. The fundamental simplifying assumption is that the fiber strains are identical to the matrix strains in the fiber direction. Thus,

$$\nu_{12} = \nu_f\ v_f + \nu_m\ v_m \tag{4.25}$$

On the other hand, in order to predict the modulus E_2 in direction transverse to the fibers, the same transverse stress σ_2 in assumed to be applied on both fibers and matrix. The strains in fibers and matrix are, therefore, obtained from the stresses:

$$\varepsilon_f = \frac{\sigma_2}{E_f} \qquad \varepsilon_m = \frac{\sigma_2}{E_m} \tag{4.26}$$

The total extension of the transverse dimension Δw can be seen as the sum of the elongation of the fibers and that of the matrix:

$$\Delta w = \varepsilon_2\ w = v_f\ w\ \varepsilon_f + v_m\ w\ \varepsilon_m \tag{4.27}$$

Simplifying w and substituting Equation 4.26 and recalling that $\sigma_2 = E_2\ \varepsilon_2$:

$$\sigma_2 = E_2 \left[\frac{v_f\ \sigma_2}{E_f} + \frac{v_m\ \sigma_2}{E_m} \right] \tag{4.28}$$

Thus,

$$E_2 = \frac{E_f \; E_m}{v_m \; E_f + v_f \; E_m} \tag{4.29}$$

which is the expression of the apparent Young's modulus in the direction transverse to the fibers and can be seen also as a *spring-in-series* model [1].

In order to determine the in-plane shear modulus of a lamina G_{12} the mechanics of materials approach assumes that the shearing stresses on the fiber and on the matrix are the same. This assumption leads to the same type of expression obtained for the transverse Young's modulus E_2:

$$G_{12} = \frac{G_f \; G_m}{v_m \; G_f + v_f \; G_m} \tag{4.30}$$

Both E_2 and G_{12} are matrix-dominated properties, indeed the fibers do not contribute much to the modulus unless the percentage of fibers is very high.

This very simple approach adopted for the evaluation of matrix-dominated properties usually underestimate the real value of the modulus [1]. Better approaches are available in literature [1]. One of the most employed is the one developed by Halpin and Tsai [58]. They developed an interpolation procedure that is an approximate representation of more complicated micromechanical results. According to Halpin and Tsai, the modulus in the direction transverse to the fibers E_2 and the shear modulus G_{12}, called generically M, can be expressed as follow:

$$M = M_m \; \frac{1 + \xi \; \eta \; v_f}{1 - \eta \; v_f} \tag{4.31}$$

where

$$\eta = \frac{(M_f / M_m) - 1}{M_f / M_m + \xi} \tag{4.32}$$

in which M_f and M_m are the corresponding fibers and matrix modulus (E or G) and ξ is called fibers reinforcement factor. The determination of a suitable value for ξ can be done empirically, fitting the experimental results of a particular composite but some physical insight into the Halpin-Tsai equation can be gained by examining its behavior for the ranges of values of ξ. ξ can range from 0 to ∞. When $\xi = 0$, Equation 4.31 simplifies to the *spring-in-series* model, generally associated with a lower bound of

a composite material modulus, when $\xi = \infty$ Equation 4.31 simplifies to the *spring-in-parallel* model, generally associated with an upper bound of a composite material modulus (Figure 4.2). Thus, ξ is a measure of the reinforcement of the composite material by the fibers. For small values of ξ, the fibers are not very effective, whereas for large values of ξ, the fibers are extremely effective in increasing the composite stiffness above the matrix stiffness. The differences can be associated to many factors among which the loading condition, the fiber geometry and the packing geometry [1].

In this work experimental results will be compared to the simple models here introduced.

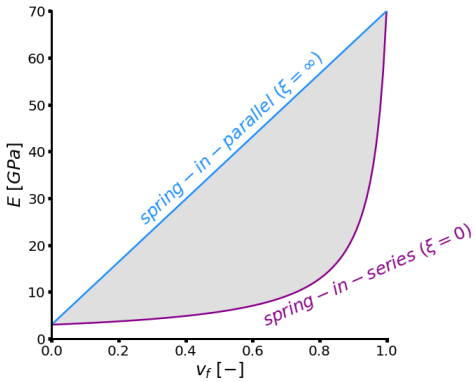


Figure 4.2: Predicted modulus bounds for a laminate with $E_1 = 70\ GPa$ and $E_2 = 3\ GPa$.

4.2.3 Classical Lamination Theory

The Classical Lamination Theory (CLT) enables the analysis of laminates that have individual laminae with principal material directions oriented at arbitrary angles to the chosen or natural axes of the laminate. It aims to describe the variation of stresses and strains through the laminate thickness that is essential to the definition of the extensional and bending stiffness of a laminate [1]. It is based on the following simplifying assumptions, commonly called Kirchhoff hypothesis for plates, that enable to reduce a complicated three-dimensional elasticity problem to a solvable two-dimensional mechanics of deformable bodies problem [1]:

- The laminate is assumed to consist in perfectly bonded laminae.

- The bonds are assumed to be infinitesimally thin and non shear-deformable. That is, the displacements are continuous across the lamina boundaries. Furthermore, a line originally straight and perpendicular to the middle surface of the laminate is assumed to remain straight and perpendicular to the middle surface when the laminate is deformed and the normals are assumed to have constant length. This means that the shearing strains in planes perpendicular to the middle surface and the strain perpendicular to the middle surface are ignored ($\gamma_{xy} = \gamma_{yz} = \varepsilon_z = 0$).

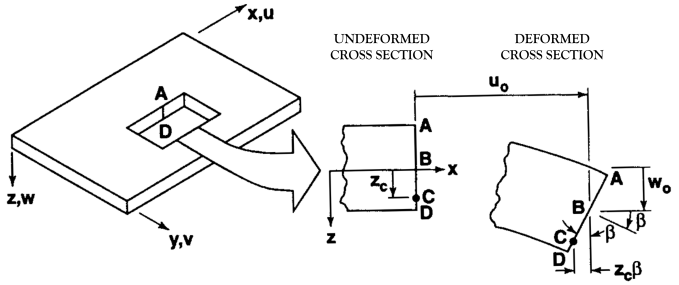


Figure 4.3: Geometry of deformation in the $x - z$ plane. Adapted from [1].

Following the Kirchhoff hypothesis the laminate displacements u, v and w in respectively x, y and z directions can be derived. Referring to the laminate cross section showed in Figure 4.3 the displacement at point C along the thickness of the laminate, u_c, can be written in function of the displacement of point B on the middle surface, u_o, as:

$$u_c = u_o - z_c \; tan\beta \tag{4.33}$$

Since the line $ABCD$, under deformation, remains perpendicular to the middle surface, $tan\ \beta$ is the slope of the laminate middle surface in the x direction, that is,

$$tan\beta = \frac{\partial w_o}{\partial x} \tag{4.34}$$

and the displacement, u, at any point z through the laminate thickness is

$$u = u_o - z \; \frac{\partial w_o}{\partial x} \tag{4.35}$$

Similarly, the displacement v in y direction is

$$v = v_o - z \frac{\partial w_o}{\partial y} \tag{4.36}$$

The laminate strains ε_x, ε_y and ε_{xy}, that by virtue of the Kirchhoff hypothesis are the only strains present in the laminate, can be defined in terms of displacements as (assuming linear elasticity):

$$\varepsilon_x = \frac{\partial u}{\partial x} \quad \varepsilon_y = \frac{\partial v}{\partial y} \quad \gamma_{xy} = \frac{\partial u}{\partial y} + \frac{\partial v}{\partial x} \tag{4.37}$$

Thus, deriving the displacements u and v in Equations 4.35 and 4.36, the strain vector of the laminate can be written as:

$$\begin{bmatrix} \varepsilon_x \\ \varepsilon_y \\ \gamma_{xy} \end{bmatrix} = \begin{bmatrix} \varepsilon_x^o \\ \varepsilon_y^o \\ \gamma_{xy}^o \end{bmatrix} + z \begin{bmatrix} \kappa_x \\ \kappa_y \\ \kappa_{xy} \end{bmatrix} \tag{4.38}$$

where the middle-surface strains are

$$\begin{bmatrix} \varepsilon_x^o \\ \varepsilon_y^o \\ \gamma_{xy}^o \end{bmatrix} = \begin{bmatrix} \dfrac{\partial u_o}{\partial x} \\ \dfrac{\partial v_o}{\partial y} \\ \dfrac{\partial u_o}{\partial y} + \dfrac{\partial v_o}{\partial x} \end{bmatrix} \tag{4.39}$$

and the middle-surface curvatures are

$$\begin{bmatrix} \kappa_x \\ \kappa_y \\ \kappa_{xy} \end{bmatrix} = - \begin{bmatrix} \dfrac{\partial^2 w_o}{\partial x^2} \\ \dfrac{\partial^2 w_o}{\partial y^2} \\ 2\,\dfrac{\partial^2 w_o}{\partial x \partial y} \end{bmatrix} \tag{4.40}$$

By substitution of the strain variation through the thickness, Equation 4.38, in the stress-strain relation, Equation 4.16, the stresses in the k^{th} layer can be expressed in terms of the laminate middle-surface strains and curvatures as:

$$\begin{bmatrix} \sigma_x \\ \sigma_y \\ \tau_{xy} \end{bmatrix}_k = \begin{bmatrix} \overline{Q_{11}} & \overline{Q_{12}} & \overline{Q_{16}} \\ \overline{Q_{21}} & \overline{Q_{22}} & \overline{Q_{26}} \\ \overline{Q_{61}} & \overline{Q_{62}} & \overline{Q_{66}} \end{bmatrix}_k \left[\begin{bmatrix} \varepsilon_x^o \\ \varepsilon_y^o \\ \gamma_{xy}^o \end{bmatrix} + z \begin{bmatrix} \kappa_x \\ \kappa_y \\ \kappa_{xy} \end{bmatrix} \right] \tag{4.41}$$

The $[\overline{Q_{12}}]$ can be different for each layer of the laminate, so the stress variation through the laminate thickness is not necessarily linear, even though the strain variation is linear. The resultant forces per unit width N

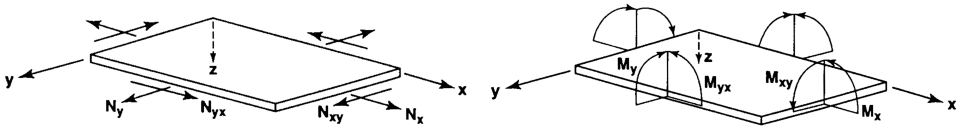


Figure 4.4: Forces and moments on a laminate. Adapted from [1].

and moments per unit width M, acting on the laminate, schematized in Figure 4.4, can be obtained by integration of the stresses in each lamina through the laminate thickness:

$$\begin{bmatrix} N_x \\ N_y \\ N_{xy} \end{bmatrix} = \sum_{k=1}^{N} \int_{z_{k-1}}^{z_k} \begin{bmatrix} \sigma_x \\ \sigma_y \\ \tau_{xy} \end{bmatrix}_k dz \tag{4.42}$$

and

$$\begin{bmatrix} M_x \\ M_y \\ M_{xy} \end{bmatrix} \sum_{k=1}^{N} \int_{z_{k-1}}^{z_k} \begin{bmatrix} \sigma_x \\ \sigma_y \\ \tau_{xy} \end{bmatrix}_k z\, dz \tag{4.43}$$

By substitution of 4.41, if the stiffness matrix $[\overline{Q_{12}}]$ is considered constant within the lamina, Equations 4.42 and 4.43 become:

$$\begin{bmatrix} N_x \\ N_y \\ N_{xy} \\ M_x \\ M_y \\ M_{xy} \end{bmatrix} = \begin{bmatrix} A_{11} & A_{12} & A_{16} & B_{11} & B_{12} & B_{16} \\ A_{21} & A_{22} & A_{26} & B_{21} & B_{22} & B_{26} \\ A_{61} & A_{62} & A_{66} & B_{61} & B_{62} & B_{66} \\ B_{11} & B_{12} & B_{16} & D_{11} & D_{12} & D_{16} \\ B_{21} & B_{22} & B_{26} & D_{21} & D_{22} & D_{26} \\ B_{61} & B_{62} & B_{66} & D_{61} & D_{62} & D_{66} \end{bmatrix} \begin{bmatrix} \varepsilon_x^o \\ \varepsilon_y^o \\ \gamma_{xy}^o \\ \kappa_x \\ \kappa_y \\ \kappa_{xy} \end{bmatrix} \tag{4.44}$$

where

$$
\begin{aligned}
A_{ij} &= \sum_{k=1}^{N} (\overline{Q_{ij}})_k \, (z_k - z_{k-1}) \\
B_{ij} &= \tfrac{1}{2} \sum_{k=1}^{N} (\overline{Q_{ij}})_k \, (z_k^2 - z_{k-1}^2) \\
D_{ij} &= \tfrac{1}{3} \sum_{k=1}^{N} (\overline{Q_{ij}})_k \, (z_k^3 - z_{k-1}^3)
\end{aligned}
\tag{4.45}
$$

The so called ABD matrix in Equation 4.44 allows to describe the response of the laminate in terms of forces and moments given the strains of the middle-surface and the curvatures of the laminate. Vice versa, given forces and moments applied on a laminate, the inverse matrix ABD^{-1} allows to predict strains of the middle-surface and the curvatures, that is the full field of displacement of the laminate.

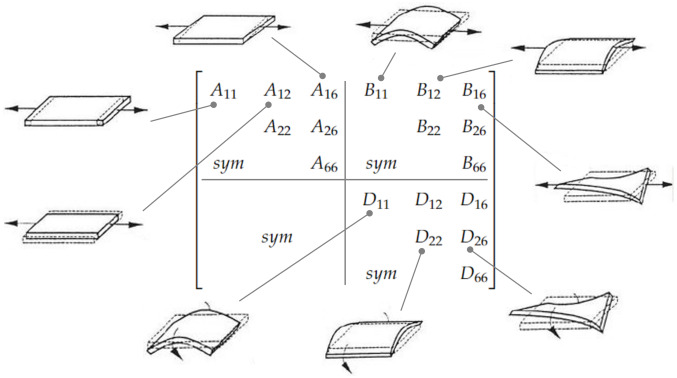


Figure 4.5: Illustration of the physical meaning of the ABD matrix.

It is important to note that several coupling between deformation modes and type of loading are possible when dealing with laminates. In particular, the A_{ij} are extensional stiffnesses with A_{16} and A_{26} representing shear-extension coupling at the laminate level analogous to that found for a single lamina (Equation 4.16), the B_{ij} are bending-extension coupling stiffnesses, they represent coupling between bending and extension, a phenomenon not found at the lamina level, and the D_{ij} are bending stiffnesses, whit D_{16} and D_{26} representing the bend-twist coupling. An illustration of the various coupling is showed in Figure 4.5.

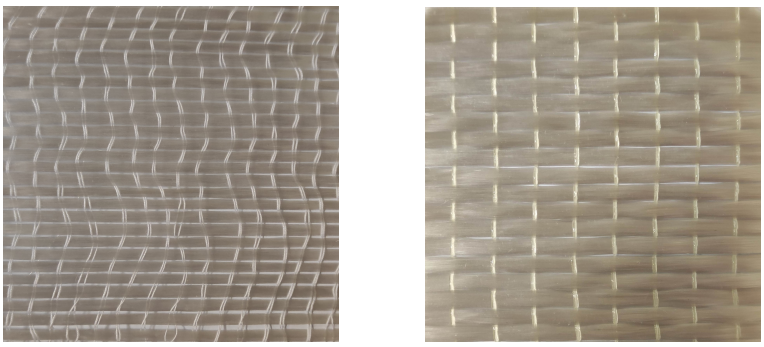
4.3 Production of the composite

Two different fabrication technologies were used to produce the GF-PDMS laminates. Some laminates were produced using a vacuum-assisted resin infusion technique (VARI), typically used for the production of rigid polymer matrix composites [59]. Other laminates, instead, were produced with a wet lay-up process using a mold, in which the uncured liquid PDMS is poured after placing the desired number of fiber layers inside the cavity. A particular procedure has been also developed to produce the unidirectional fibers layer used to produce the laminates. In the next sections, the procedure followed to produce the layers of unidirectional fibers will be explained in detail, as well as the two technologies for producing the composite, emphasizing their respective pros and cons.

4.3.1 Preparation of unidirectional fiber layers

In commercially available tapes of continuous fibers (uni-directional and multi-directional) bundles of fibers are kept together by stitches usually made of thin threads (see few example in Figure 4.6). In traditional rigid-matrix laminates, these thin threads are left in the fibers layers and are embedded in the composite matrix, in order to help to keep the fibers straight and in the right position during manufacturing, and the global performance of the laminate is not influenced by the presence of these slight connections. In this work it will be showed that the behavior of soft-matrix laminates is instead highly affected by the presence of the stitches. In a low stiffness matrix ($E \approx 1\ MPa$), the stiffness of the single threads is not negligible and, in the direction perpendicular to the fibers, clearly affects the behavior of the laminates leading to an clear non-homogeneity in the response of the laminate (the results of this study will be showed in Section 4.4.3.1).

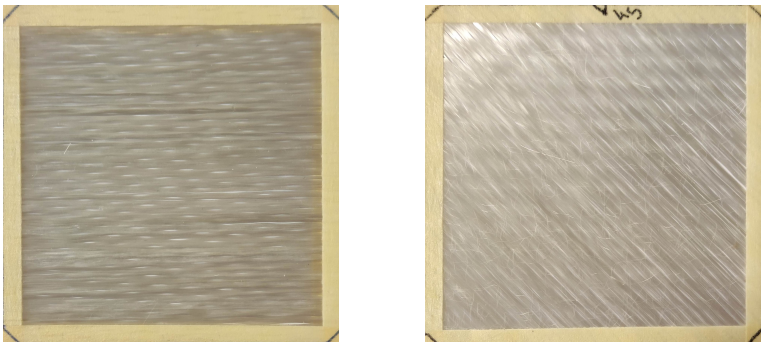
It was therefore deemed appropriate to develop a procedure to obtain unidirectional fiber layers without stitches. In order to maintain fiber alignment and obtain unidirectional fiber layers without stitches, it was necessary to sustain the fibers at the ends with adhesive tape before removing the stitches. Considering that unidirectional fiber tapes are not easily available on the market and that often the stitches are thermally welded and therefore impossible to remove, it has been decided to start



(a) (b)

Figure 4.6: (a) Unidirectional glass fibers tape with cotton stitches. Areal weight 210 g/m^2. (b) Unidirectional glass fibers tape with thermowelded stitches. Areal weight 600 g/m^2.

from $\pm 45^\circ$ bidirectional tapes normally fixed with cotton stitches easily removable. Starting with tapes 1270 mm wide, with areal weight of 400 g/m^2 rectangular sheets were taken, the edges were held with adhesive tape, the stitches were removed, and two layers of unidirectional fibers (areal weight 200 g/m^2), held in place by the adhesive tape at the ends, were obtained. For laminates production, rectangles of the desired size were then extracted from each unidirectional sheet, with the fibers already oriented in the desired direction. Few examples of fibers layers with different orientations are showed in Figure 4.7.



(a) (b)

Figure 4.7: Dry unidirectional glass fibers tapes without stitches, ready to be embedded in the PDMS matrix. The fibers are held in place by the adhesive tape at the ends. (a) Layer for 0° or 90° fiber angle. (b) Layer for $+45^\circ$ or -45° fiber angle.

4.3.2 Vacuum-Assisted Resin Infusion

Vacuum assisted resin infusion (VARI) is a typical laminate manufacturing process to produce high quality components. In this process, dry fabrics are laid in an open mold and a plastic vacuum bag is placed on the top of the mold. The mold is connected with a resin source and a vacuum pump. The liquid resin infuses into the reinforcing fibers thanks to the vacuum drawn through the mold.

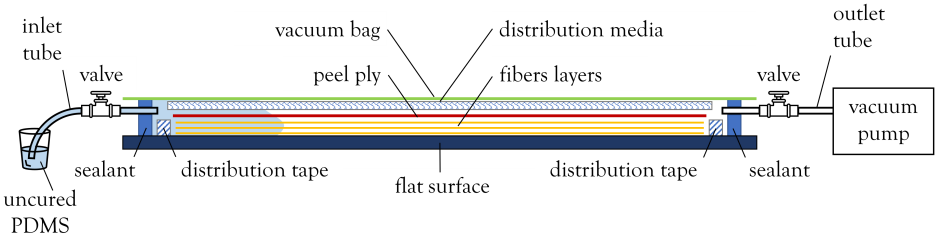


Figure 4.8: Schematic illustration of the vacuum assisted resin infusion process (VARI).

The setup of the VARI system used in this work is showed in Figure 4.8. The main steps of the process are:

- the desired fiber layers are positioned on a flat rigid surface;
- accompanying materials such as peel plies, distribution media and distribution tape are laid on the surface;
- the preform is sealed with a vacuum bag and the air is evacuated by a vacuum pump;
- the liquid uncured PDMS mixed and degassed as explained in Section 2.3.1 is infused into the preform until complete impregnation;
- the system is sealed and left to cure for the first 20 h at 23°C and then for 75 min at 150°C;
- after cooling, the laminate is demolded and ready to use.

The reported thermal history was chosen based on the experience acquired during the investigation of the crosslinking kinetics of Sylgard®184, described in detail in Chapter 2. In particular, the first crosslinking phase at

$23°C$ is necessary to facilitate the impregnation of the fibers and the extraction of any air bubbles trapped in the laminate during the impregnation phase. The second phase at $150°C$ is needed to complete the crosslinking of the PDMS in a reasonable time (at $23°C$ it would take days). This technique, which does not use a mold, provides great flexibility and allows to produce laminates of different sizes according to the project requirements. In addition, the upper distribution media collects all the air bubbles eventually trapped in the vacuum bag reducing therefore the presence of defects in the laminate. On the other hand, several disposable ancillary materials (peel ply, distribution media, sealing tape, vacuum bag) have to be used and the lack of a rigid and perfectly smooth top surface, like that of a mold, results in a higher surface roughness on the side facing the peel ply. In addition to the previously mentioned, the main limitation of the vacuum infusion technique is the limited control on the laminate thickness, and therefore on the fiber-volume fraction of the laminates obtained. Indirectly, by varying the extraction force of the vacuum pump and the effectiveness of the vacuum sealing of the system, it is possible to vary the amount of PDMS infused into the vacuum bag during impregnation, and thus the fiber-volume fraction. The control is however not as simple and straightforward as the control of the thickness that can be done using a mold with a defined thickness cavity.

4.3.3 Molding

A schematic illustration of the laminate manufacturing steps necessary by using a mold, is showed in Figure 4.9. The procedure involves the following steps:

- preparation of the desired fiber layers of the size of the mold cavity;
- mixing and degassing of pre-polymer and curing agent according to the procedure explained in Section 2.3.1;
- mold filling with alternating layers of liquid uncured PDMS and fiber layers;
- degassing by leaving the open mold in a vacuum oven (applied vacuum $\approx 7\ 10^4\ Pa$) for $1\ h$ to allow the air bubbles incorporated during the previous steps to be expelled;

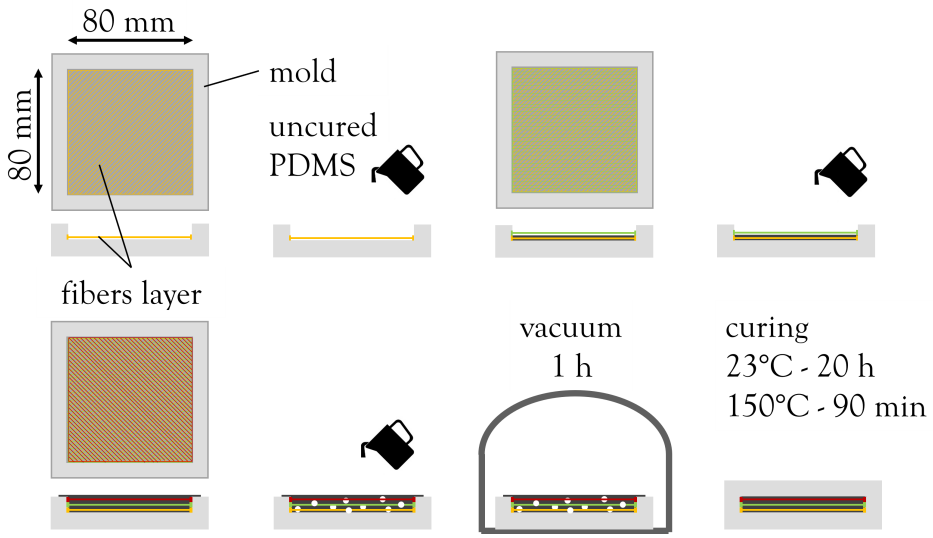


Figure 4.9: Schematic illustration of the process applied to produce a laminates with a mold.

- mold closure and removal of the liquid PDMS in excess;
- curing for 20 h at 23°C and then for 90 min at 150°C;
- cooling and demolding of the laminate.

In this procedure the mold is left in the oven at 150°C for 90 min, instead of 75 min used to cure the laminate produced with VARI, because about 15 min are required to bring the mold walls to the desired temperature of 150°C. This technique, compared to VARI, allows an accurate control of the laminate thickness (which coincides with the depth of the mold cavity). In this way, by varying the number of fiber layers and the depth of the cavity, it is possible to accurately vary the fiber-volume fraction of the laminate. On the other hand, the size of the laminate is limited by the size of the mold, so there is less flexibility in the production. In addition, defects are much more frequent, especially air bubbles trapped in the mold that cannot be removed as easily as with the vacuum bag. In this work, two molds with different size has been used. A small square mold 80 mm x 80 mm and a bigger rectangular mold 300 mm x 210 mm. The cavity thickness for both molds could be varied between 1 mm and 2 mm.

4.3.4 Fiber-volume fraction evaluation

The fiber-volume fraction of the laminate obtained have been evaluated knowing the number, n, and the areal weight, AW, of the fibers tapes embedded in a sample and the thickness t of the sample, according to the following equation:

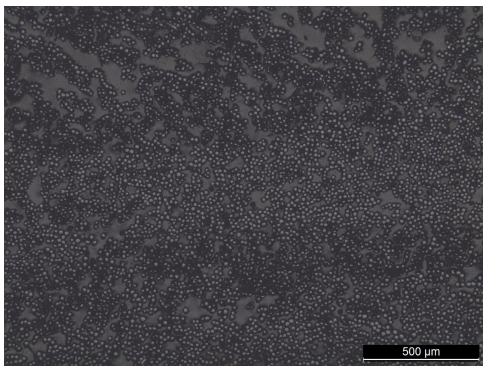
$$v_f = \frac{V_f}{V_{tot}} = \frac{AW\ w\ L\ n}{w\ L\ t} = \frac{AW\ n}{t} \tag{4.46}$$

where w is the width of the sample, L is the length of the sample and the other symbols have been mentioned before. The declared area weight of the fibers tape have been used after validating it by weighing more than a hundred layers of fibers of known area.

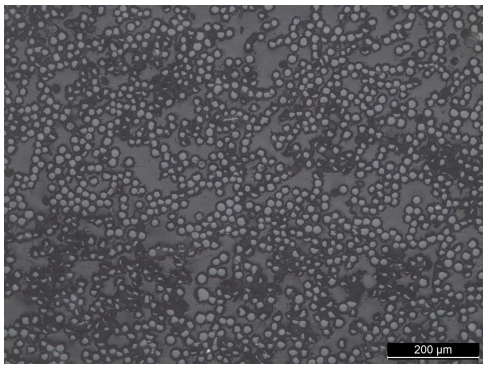
4.3.5 Microscopy

To have an idea of the homogeneity of the laminates produced, some samples were observed with an Olympus BX-60 optical microscope in bright field configuration. In order to analyze the fibers distribution along the thickness of the laminates, mono-oriented laminates have been cut perpendicularly to the fiber direction, have been embedded in epoxy-resin and polished on rotating wheels covered with clothes impregnated of water suspension of diamond abrasive powder.

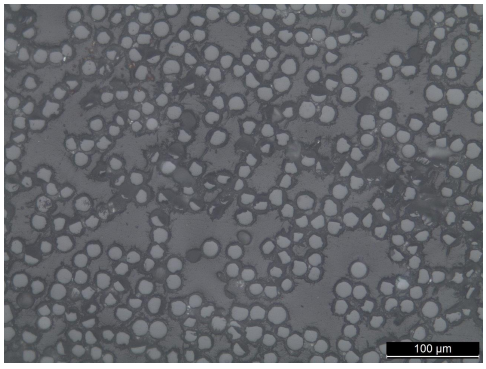
Figure 4.10 shows some micrographs respectively with magnification level 50x, 100x and 200x. The micrographs show the section of the fibers embedded in the PDMS matrix. The fibers are well aligned all in the same direction. Areas more or less rich in fibers can be observed but no macroscopic void are present in the samples analyzed. The fibers are properly bonded to the matrix and no air bubbles are left inside the composite. The dark gray parts that are sometimes visible around the fibers are probably due to some contamination left by the polishing process.



(a)



(b)



(c)

Figure 4.10: Micrographs of unidirectional GF-PDMS laminates cut perpendicularly to the fiber direction. Fibers are the light gray circle. (a) Magnification level 50x. (b) Magnification level 100x. (c) Magnification level 200x.

4.4 Lamina's mechanical characterization: small strains

As explained in Section 4.2.1 a lamina can be considered a *transversely isotropic* material in plane stress state, and four independent material constants are required to describe its mechanical behavior. In this section the mechanical behavior of a GF-PDMS lamina at small strains will be investigated. In this range for deformation the material will be considered linear-elastic. The material constants calculated and the methods adopted are as follows:

- elastic modulus in the fiber direction, E_1, measured by means of quasi-static tensile tests with load applied in the fibers direction (Figure 4.11a);
- elastic modulus in direction perpendicular to the fiber, E_2, measured by means of quasi-static tensile test applying the load in direction perpendicular to the fibers (Figure 4.11b);
- Poisson's ratio ν_{12} and ν_{21}, measured by means of respectively quasi-static tensile tests with load applied in the fibers direction (Figure 4.11a) and quasi-static tensile tests applying the load in direction perpendicular to the fibers (Figure 4.11b).
- in plane shear modulus G_{12}, measured by means of quasi-static tensile tests of symmetric-balanced laminates $[+45, -45]_{2S}$ (Figure 4.11c).

4.4.1 Methods

Uniaxial tensile tests were performed with an INSTRON 5967 or a Z010 ZwickRoell universal testing machine, under displacement control. Two load cell were used: a 30 kN load cell for quasi-static tensile tests in fibers direction and 2 kN load cell for the other tests. Tests were carried out in a controlled environment at 23$^{\circ}C$ and 50% of relative humidity. Strains have been measured locally, with a digital image correlation (DIC) system. The DIC technique consists in recording the displacement of a suitable pattern on the sample during the test and evaluating the deformations by correlating the evolution of the recorded images with respect to a reference one, representing the undeformed state. The images were acquired either with

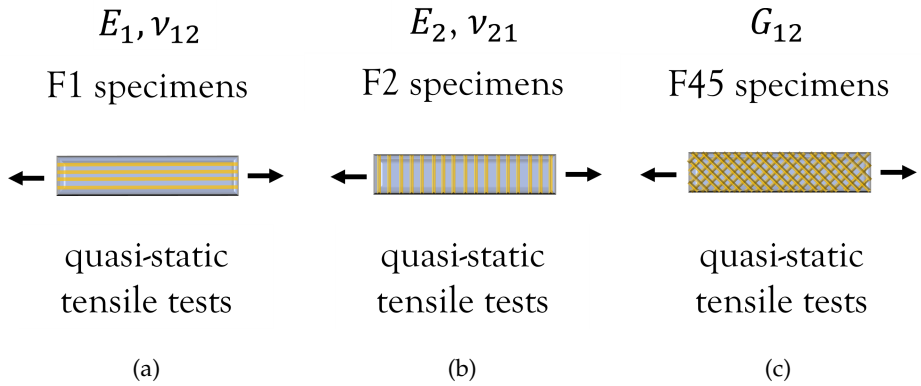


Figure 4.11: Quasi-static tests performed to measure the four independent elastic constants of the lamina. (a) Tensile test in fibers direction. (b) Tensile test in direction perpendicular to the fibers. (c) Tensile tests on symmetric-balanced laminates $[+45, -45]_{2S}$.

a UI-5490SE camera (sensor size 12.7 *mm*) mounting a NIKON 28-105 objected and analyzed with VIC2D-2009 software, or with a Prosilica GT 6600, Allied Vision Technologies camera (sensor size 35 *mm*) and analyzed with Mercury^{RT} software. The distance between the camera and the specimen was about 1 *m*.

4.4.2 Determination of E_1

The method adopted for measuring the modulus E_1 followed the ASTM D3039/D3039M - 17 Standard Test Method for Tensile Properties of Polymer Matrix Composite Materials [60]. The modulus in fiber direction E_1 is quite difficult to measure, especially in highly *anisotropic* laminates. The greater the difference between fibers and matrix properties, the more difficult to perform the test. In fact, uniaxial tensile tests present several critical issues, particularly in the gripping of specimens. For rigid matrix composites the use of end tabs is strongly recommended to reduce edge effects [60]. In flexible matrix composites, the use of end tabs or other gripping systems are indispensable to perform a tensile test. The four orders of magnitude difference between the fiber and matrix properties leads to a composite that is very stiff in one direction and very compliant in the perpendicular direction. When gripping a specimen with these characteristics, the matrix, compressed by the grips, expands perpendicularly and the fibers misalign,

creating an hourglass shape as in Figure 4.12. If the tensile test is carried out under these conditions, the fibers tend to realign themselves by separating as at the grips and this leads to a positive deformation in direction 2 (Figure 4.12) followed by the slipping of the sample out of the grip as soon as the fibers are stretched.

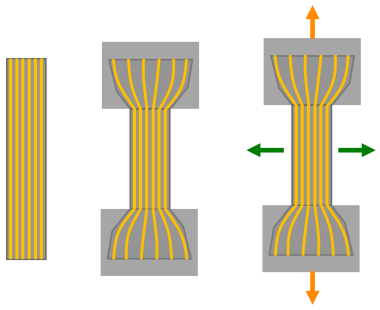
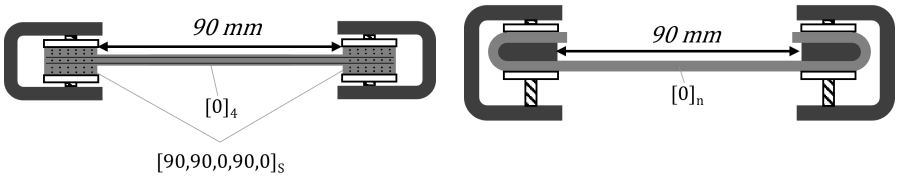


Figure 4.12: Illustration of the behavior of unidirectional continuous fibers flexible composites clamped without end tabs. Yellow lines are the continuous fibers. From left to right: the specimen before clamping, the specimen with hourglass shape due to the compression of the clamps, the specimen tends to expand (green arrows) when a load in the fiber direction is applied (orange arrows).

Two different approaches have been adopted to avoid this problem:

- the use of end tabs to reinforce the specimen in the direction perpendicular to the fibers in the area of the grips (Figure 4.13a);
- the use of special grips so that the specimen ends are bent in a U shape in order to maximize the grip surface and decrease the pressure necessary to clamp the sample (Figure 4.13b).

Fibers layers with fibers oriented perpendicularly to the loading direction have been employed as end tabs. The fibers layers have been embedded in the matrix during the production of the composite, positioning aluminum spacers in the central part of the mold to compensate for the difference in thickness between the central part of the sample and the gripping zones. The lamination sequence for the gripping was $[90, 90, 0, 90, 0]_S$. Even with the introduction of these features, both solutions do not allow to perform tensile tests up to specimen failure, as slippage occurs prematurely. However, they can be adopted to measure the modulus at small deformations.



(a) (b)

Figure 4.13: Illustration of the gripping system employed to perform quasi-static tensile tests in fibers direction. (a) Specific end tabs to properly clam the specimen. (b) U-shaped" built-in tabs to properly hold the specimen without adding tabs.

4.4.2.1 Experimental results

All the specimens tested had width $w_0 = 15\ mm$ and thickness ranging from 0.46 mm and 1.11 mm with a gauge length of 90 mm. The fiber-volume fraction ranged between 0.31 and 0.49. Tests have been performed at strain rate of 0.11 $1/s$. Uniaxial tension stress σ has been calculated as:

$$\sigma = \frac{F}{w_0\ t_0} \tag{4.47}$$

where F is the load measured, w_0 is the initial width of the specimen and t_0 is the initial thickness of the specimen. Engineering strains in direction 1 and 2 have been measured optically with DIC.

Fourteen specimens have been tested in total. An example of the stress-strain curves obtained are shown. In particular, Figure 4.14a shows the stress-strain curves obtained from specimens with end tabs and fiber-volume fraction $v_f = 0.31$. Figure 4.14b shows the stress-strain curves obtained from specimens with the U-shaped ends and fiber-volume fraction $v_f = 0.37$. The end of the test does not correspond to the failure of the specimen: tests have been stopped when the specimen started to slip from the grips.

The tensile modulus E_1 have been calculated as the slope of the linear fit of the first part of the stress-strain curve, up to 0.002 of strain. Figure 4.15 shows the tensile modulus, E_1 versus the fiber-volume fraction, v_f of the tested specimens. Despite some dispersion in the data, a linear increase of the modulus with fiber-volume fraction can be observed.

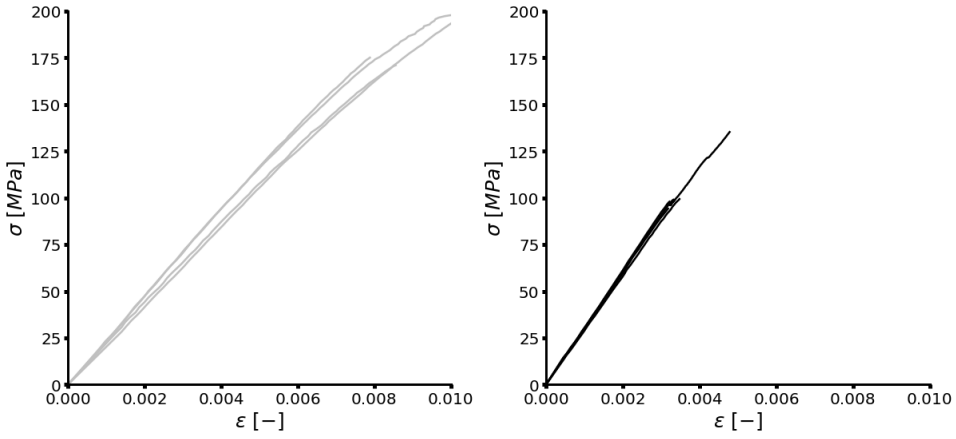


Figure 4.14: Stress-strain curves of uniaxial tensile tests in fibers direction. (a) Specimens with end tabs and fiber-volume fraction $v_f = 0.31$. (b) Specimens with U-shaped ends and fiber-volume fraction $v_f = 0.37$.

4.4.2.2 Micromechanical models

The micromechanical model adopted to fit experimental results of the measurement of E_1 is the simple *spring-in-parallel* model. In order to apply the model, the modulus of the fiber E_f and the modulus of the matrix E_m have to be known. The modulus of the fibers, E_f, was considered to be 72000 MPa, measured as explained in Chapter 3 for the glass fibers used to produce the laminae. The modulus of the PDMS, E_m, was considered to be 3.3 MPa. This values could be obtained from the shear modulus of the PDMS cured at $T_c = 150°C$, measured with rheological experiments as showed in Chapter 2, applying Equation 4.9 and considering a Poisson's ratio $\nu = 0.45$ (measured for Sylgard®184 in the work of Pini [61]). This value was also verified by performing quasi-static tensile tests on the PDMS alone cured under the same thermal history of the composite. The results of quasi-static tensile tests are reported in Appendix A.

The modulus in fiber direction E_1 can be plotted versus the fiber-volume fraction v_f according to Equation 4.24 remembering that $v_m = 1 - v_f$. Figure 4.16 shows the comparison of the *spring-in-parallel* model and the moduli E_1 experimentally measured. The *spring-in-parallel* model is consistent with the values of the moduli experimentally measured with both the gripping methods.

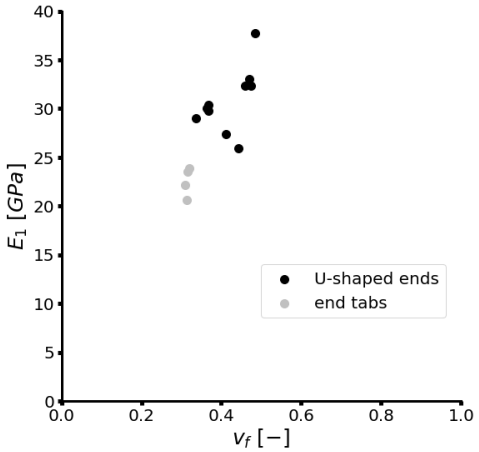


Figure 4.15: Tensile modulus, E_1 versus fiber-volume fraction, v_f.

4.4.3 Determination of E_2

Elastic modulus in direction perpendicular to the fiber direction, E_2, has been measured by means of quasi-static tensile tests applying the load in direction perpendicular to the fibers. Rectangular specimens with width $w_0 = 12.5\ mm$ and thickness ranging from 0.47 mm and 2.11 mm with a gauge length of 50 mm have been employed. The fiber-volume fraction ranged between 0.15 and 0.47. Tests have been performed at strain rate of 0.12 $1/s$. Uniaxial tensile stress σ has been calculated through Equation 4.47. Engineering strains in direction 1 and 2 have been measured optically with DIC.

4.4.3.1 Experimental results

In the first part of the section the distribution of the local strain along the specimen will be showed and the effect of the presence of the stitches evidenced. In the second part an average strain values will be considered and the average modulus E_2 calculated.

4.4.3.1.1 Local strains

In order to verify the homogeneity of the composite, the strain distribution along the length of the specimen has been analyzed. Two different types of specimens have been analyzed. Specimens ”type A” obtained from laminae made with unidirectional fibers tapes like the one showed

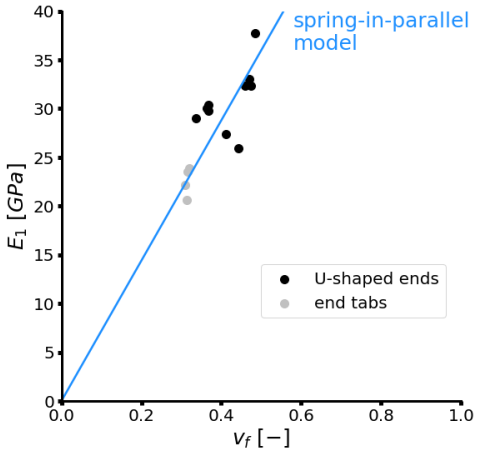
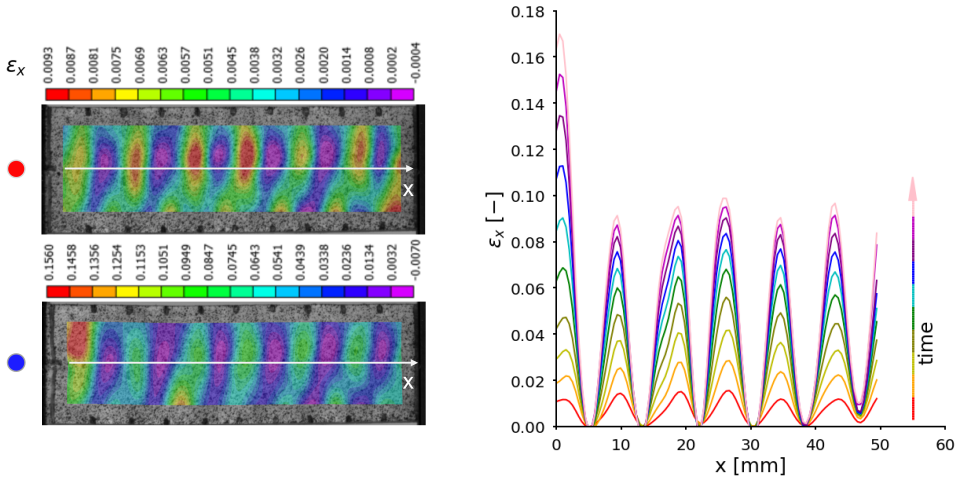


Figure 4.16: Tensile modulus, E_1 versus fiber-volume fraction, v_f. The light blue line is the *spring-in-parallel* model (Equation 4.24) with $E_f = 72000\ MPa$ and $E_m = 3.3\ MPa$. Circles are experimental results.

in Figure 4.6b, in which the stitches are embedded in the composite, and specimens "type B" obtained from laminae made with fibers layers without stitches like the one in Figure 4.7.

An example of strains distribution of a "type A" specimen is showed in Figure 4.17a. The upper image corresponds the strain ε_x distribution after 2.4 s from the beginning of the test, the lower image corresponds to the strain ε_x distribution after 29 s. Figure 4.17b shows the evolution in time of the local strain in the central line of the specimen (white line in Figure 4.17a). It can be seen that there are zones in which the strain is practically null during all the test and zones in which the strain increases with time, as expected in a tensile test. The zones in which there is no deformation correspond to the position of the stitches. Even if they are just thin threads, since the matrix has a very low stiffness ($E_m = 3.3\ MP$) the stitches act has a rigid constrain for the matrix. This kind of specimens have been therefore discarded for all the subsequent tests.

Figure 4.18 refers instead to a example of "type B" specimen. In particular, the upper image of Figure 4.18a shows the strain ε_x distribution after 11 s from the beginning of the test, the lower image shows the strain ε_x distribution after 37 s. Figure 4.18b shows the evolution in time of the local strain in the central line of the specimen (white line in Figure 4.18a). It can be seen that even for these specimens the strains are not homogeneous, but



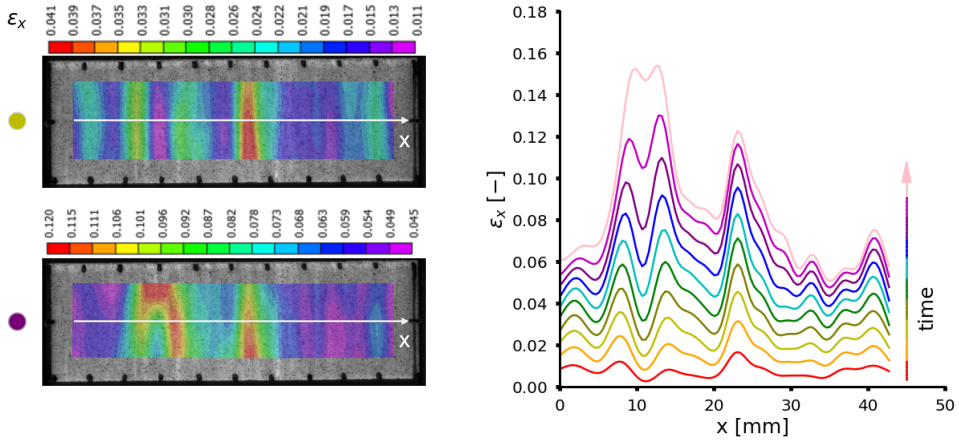
(a) (b)

Figure 4.17: (a) Example of strains distribution of a "type A" specimen. The upper image shows the strain distribution after 2.4 s from the beginning of the test, the lower image shows the strain distribution after 29 s from the beginning of the test. The colored dots on the left of the two maps refer to the color of the curve in (b) taken at the same time. (b) Local strain, ε_x, versus the coordinate x of the central line of the specimen (white line in (a)). Curves colored from red to pink indicate the ε_x distribution at different increasing times.

there are no zones that do not deform. The inhomogeneity of the strain is presumably related to the inhomogeneity of the fibers distribution into the sample. This inhomogeneity can not be avoided considering the manual process employed to produce the laminates. Anyway, for the analysis of the lamina's properties at small strains this inhomogeneity is acceptable. Indeed, as it will be showed in the next section, the modulus E_2 have been calculated in the strain range $0 - 0.01$.

4.4.3.1.2 Global strains

For the evaluation of the global strain of each specimen a mean value of the strains have been extracted with DIC software. A total of thirty five specimens have been tested. Figure 4.19 shows, as an example, the stress-strain curves of the specimens of three different fiber-volume fractions ($v_f = 0.21$, $v_f = 0.32$ and $v_f = 0.46$). Elastic modulus E_2 has been calculated as the slope of the linear fit of the first part of the stress-strain



(a) (b)

Figure 4.18: (a) Example of strains distribution of a "type B" specimen. The upper image shows the strain distribution after 11 s from the beginning of the test, the lower image shows the strain distribution after 37 s from the beginning of the test. The colored dots on the left of the two maps refer to the color of the curve in (b) taken at the same time. (b) Local strain, ε_x, versus the coordinate x of the central line of the specimen (white line in (a)). Curves colored from red to pink indicate the ε_x distribution at different increasing times.

curve. In particular, for fiber-volume fraction $v_f < 0.3$ has been considered a linear region up to 0.1 of strain and for fiber-volume fractions $v_f > 0.3$ a linear region up to 0.03 of strain.

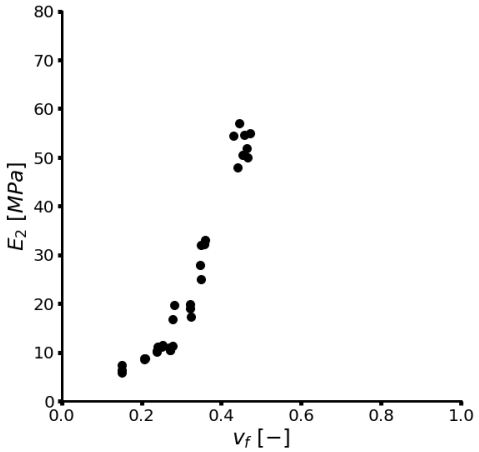


Figure 4.20: Tensile modulus, E_2 versus fiber-volume fraction, v_f.

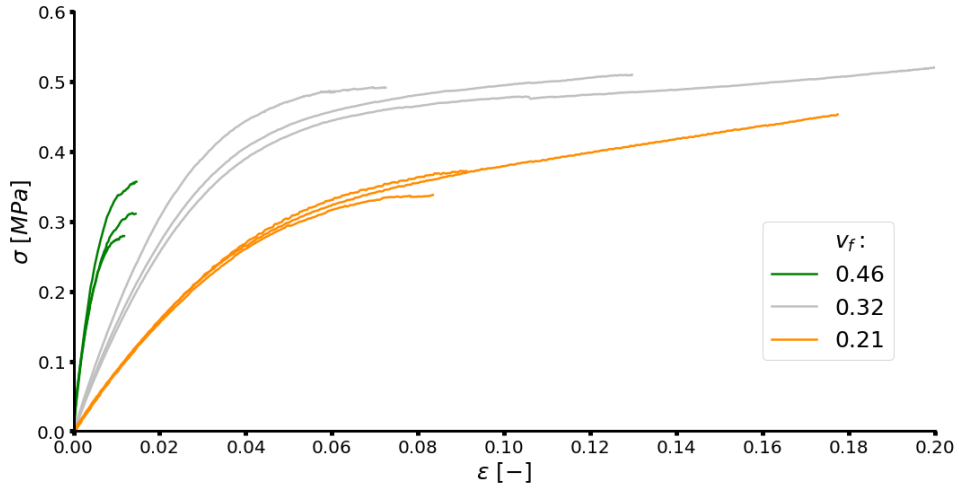


Figure 4.19: Stress-strain curves of uniaxial tensile tests with load perpendicular to the fibers direction. In green specimens with $v_f = 0.46$, in gray specimens with $v_f = 0.32$ and in orange specimens with $v_f = 0.21$.

The modulus E_2 versus the fiber-volume fraction of all the tested specimens is showed in Figure 4.20. The values of the modulus exponentially increase with fiber-volume fraction, reaching values almost 20 times greater than the modulus of the matrix alone.

4.4.3.2 Micromechanical models

A comparison of the experimental values obtained with the *spring-in-series* model (Equation 4.29) is showed in Figure 4.21 (purple continuous line). The experimental values of the modulus are significantly higher than the values predicted by the *spring-in-series* model. It is often observed in literature [1] that the *spring-in-series* model underestimates the values of the modulus in direction perpendicular to the fibers due to the simple assumptions made to derive the model [1] and better approaches, among which the Halpin-Tsai equation, have been developed.

As can be seen in Figure 4.21, even the Halpin-Tsai equation is not able to properly predict the moduli of the fiber-reinforced laminae considered. The dashed lines correspond to the Halpin-Tsai prediction with different values of the fibers reinforcement factor ξ. It is interesting to note that ξ values between 1 and 2 are good values for the prediction of the modulus E_2 in rigid matrix fiber-reinforced composites. For this range of values

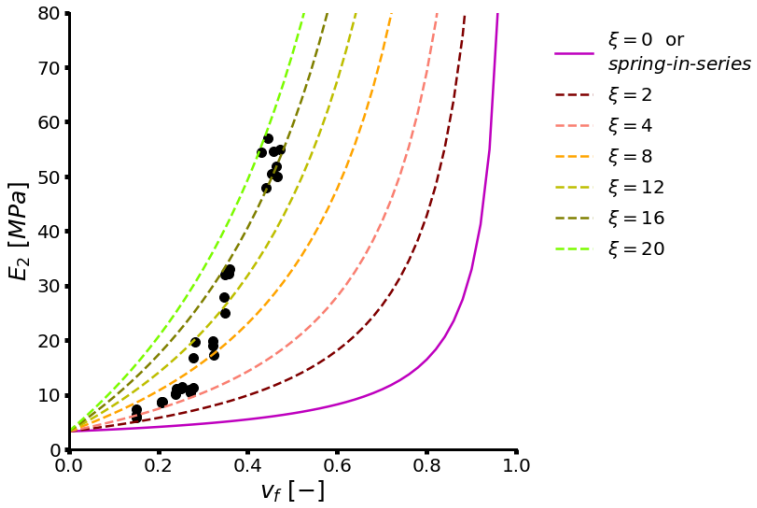


Figure 4.21: Tensile modulus, E_2 versus fiber-volume fraction, v_f. Comparison of experimental data with *spring-in-series* model (Equation 4.29) and Halpin-Tsai equation (Equation 4.31). ξ is the fibers reinforcement factor.

a physical interpretation of the fibers reinforcement factor is sometimes possible [1]. Here, in order to fit the experimental E_2 values, ξ values between 4 and 20 must be considered and a physical interpretation is no more possible. Furthermore, a single value of ξ is not enough to predict the moduli at different fiber-volume fraction. For example, $\xi = 4$ could be assumed for specimens with $v_f = 0.2$ while, $\xi = 16$ is necessary to predict the modulus of specimens with $v_f > 0.4$. Therefore, the Halpin-Tsai equation cannot be considered a valid approach for the prediction of the modulus of GF-PDMS composites.

A further observation can be made if we consider the incompressible nature of the matrix. It is know [62] that if a cylindrical bock of an incompressible material constrained between two rigid plates is compressed or extended, the material shows an increase of its modulus. The entity of the increase depends on the ratio between the radius a of the plates and their distance h. The higher the ratio a/h, the higher the effective modulus. Gent [62] showed that a constrained incompressible materials can show a modulus tens of times higher that the modulus of the material unconstrained. In these laminates the matrix in nearly incompressible, the measured Poisson's ratio of the PDMS considered is 0.45 [61], and the matrix is constrained by almost undeformable fibers. Although the

geometry of the system is different, the confinement effect may be present and the effective values of the matrix modulus may depend on the fiber content. In particular, higher fiber content leads to lower distance between fibers and thus higher rubber confinement and higher matrix effective modulus. This seem to agree with the observed increase in the ξ parameter of the Halpin-Tsai model.

On the basis of the considerations about the possible rubber confinement a new model has been developed to predict the variation of the modulus E_2 with the variation of the fiber-volume fraction. The new model is based on Equation 4.29 of the *spring-in-series* model but considers a modulus of the matrix variable with the fiber-volume fraction:

$$E_2 = \frac{E_f E_m(v_f)}{(1 - v_f)E_f + v_f E_m(v_f)} \tag{4.48}$$

In order to properly define the function $E_m(v_f)$ and empirical approach has been used. The modulus of the matrix needed to obtain the right values of E_2, applying the *spring-in-series* model has been calculated for each experimental values with the following equation, directly derived from Equation 4.29:

$$E_{m_t} = \frac{1 - v_f}{\frac{1}{E_2} - \frac{v_f}{E_f}} \tag{4.49}$$

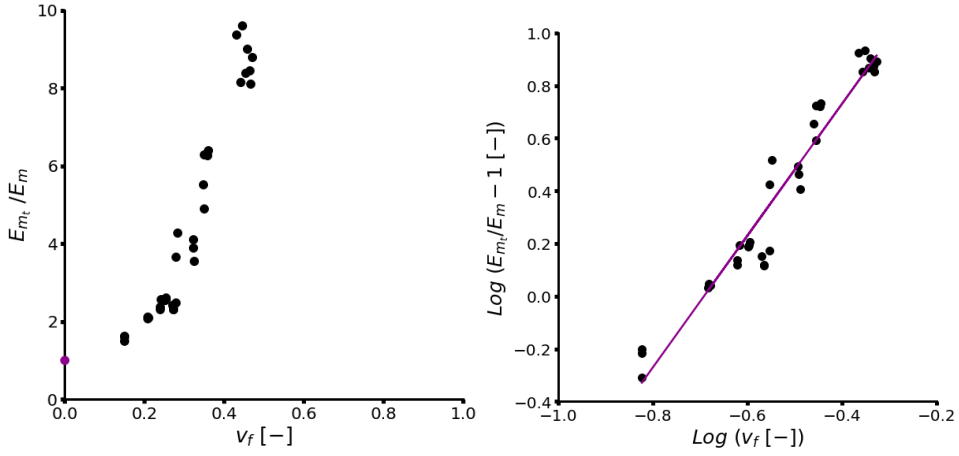
The values E_{m_t}, normalized with respect to the modulus of the pure matrix without fibers ($E_m = 3.3\ MPa$) are showed in Figure 4.22a versus the relevant fiber-volume fraction. The fitting function has to be chosen in such a way that for $v_f = 0$, $E_{m_t} = E_m$ (purple dot in Figure 4.22a). Given this constraint, a power law has been chosen:

$$\frac{E_{m_t}}{E_m} - 1 = A\ {v_f}^{\,b} \tag{4.50}$$

In a log-log representation, the power law can be represented as a linear function:

$$Log\left(\frac{E_{m_t}}{E_m} - 1\right) = Log(A) + b\ Log(v_f) \tag{4.51}$$

that is, the plot of $Log(E_{m_t}/E_m - 1)$ versus $Log(v_f)$ can be approximated to a straight line of slope b and intercept $Log(A)$ (Figure 4.22b). The linear fitting returns $b = 2.5$ and $A = 54$. Therefore, the new model can be written



(a) (b)

Figure 4.22: (a) E_{m_t} calculated according 4.49, normalized respect to the modulus of the pure matrix without fibers ($E_m = 3.3\ MPa$) versus fiber-volume fraction, v_f. (b) $Log(E_{m_t}/E_m - 1)$ versus $Log(v_f)$. Black dots are experimental values. Purple line is the linear fit.

as:

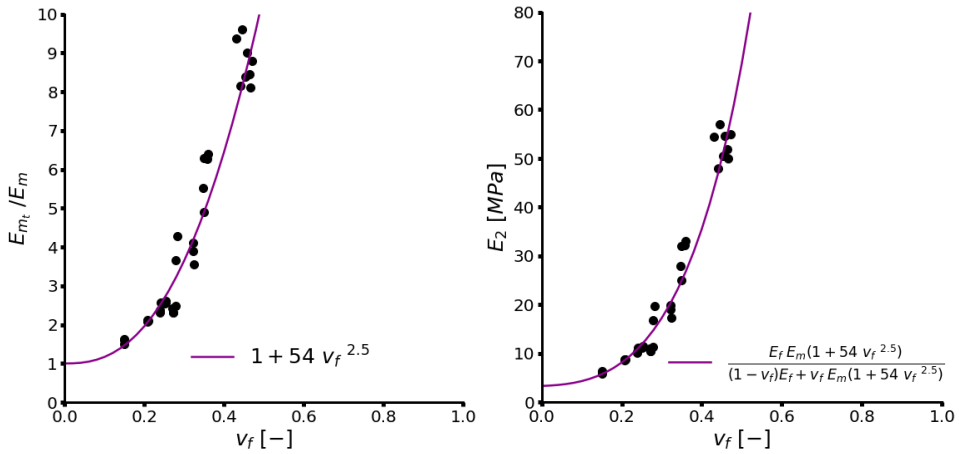
$$E_2 = \frac{E_f E_m (1 + A\ {v_f}^b)}{(1 - v_f)E_f + v_f E_m (1 + A\ {v_f}^b)} \tag{4.52}$$

In Figure 4.23a can be seen that Equation 4.50 well predicts the experimental data and in Figure 4.23b can be seen the prediction of the modulus E_2.

Although we are not able to provide a theoretical calculation of the contribution of the rubber confinement because it depends on many factors that we are not able to control at this stage of experimentation (including geometry, Poisson's ratio, fiber-matrix adhesion) the increase in modulus predicted by this model is aligned with the behavior expected from confined rubber. Further studies in this direction are certainly of interest for future works.

4.4.4 Determination of Poisson's ratios

Both Poisson's ratios ν_{12} and ν_{21} have been measured. The Poisson's ratio is the negative ratio of lateral contraction strain to axial extensional strain caused by axial extensional stress:



(a) (b)

Figure 4.23: (a) E_{m_t} calculated according Equation 4.49, normalized respect to the modulus of the pure matrix without fibers ($E_m = 3.3\ MPa$) versus fiber-volume fraction. Purple line reproduce Equation 4.50 with $b = 2.5$ and $A = 54$. (b) Tensile modulus, E_2 versus fiber-volume fraction, v_f. Comparison of experimental data (black dots) with Equation 4.52 with $b = 2.5$ and $A = 54$ (purple line).

$$\nu_{12} = -\frac{\varepsilon_2}{\varepsilon_1} \quad \sigma_1 \neq 0 \qquad \nu_{21} = -\frac{\varepsilon_1}{\varepsilon_2} \quad \sigma_2 \neq 0 \tag{4.53}$$

Thus, ν_{12} can be calculated from quasi-static tensile tests with load applied in the fibers direction (direction x coincides with direction 1) also employed for the evaluation of E_1 while ν_{21} can be calculated from quasi-static tensile tests applying the load in direction perpendicular to the fibers (direction x coincides with direction 2) also employed for the evaluation of E_2.

The test conditions for these tests have been already reported in Sections 4.4.2 and 4.4.3. Strains in direction x and y have been evaluated with DIC. The strains in direction perpendicular to the loading direction are not easy detectable. In quasi-static tensile tests with load applied in the fibers direction, the gripping of the sample is complex and fibers misalignment or pre-deformation of the specimen at the beginning of the test can occurs. This lead to the formation of a toe [63] in the experimental results that has to be corrected. In quasi-static tensile tests with load in direction perpendicular to the fibers, the strains ε_y are of the order of the DIC software resolution. An example of the strains ε_x and ε_y versus time are

showed in Figure 4.24. Figure 4.24a refers to a quasi-static tensile tests with load applied in the fibers direction. In this case the transversal strain ε_y is higher than the longitudinal strain ε_x. Figure 4.24b refers to a quasi-static tensile tests with load in direction perpendicular to the fiber. Vice versa, in this case, the longitudinal strain ε_x is higher than the transversal strain ε_y which is almost null.

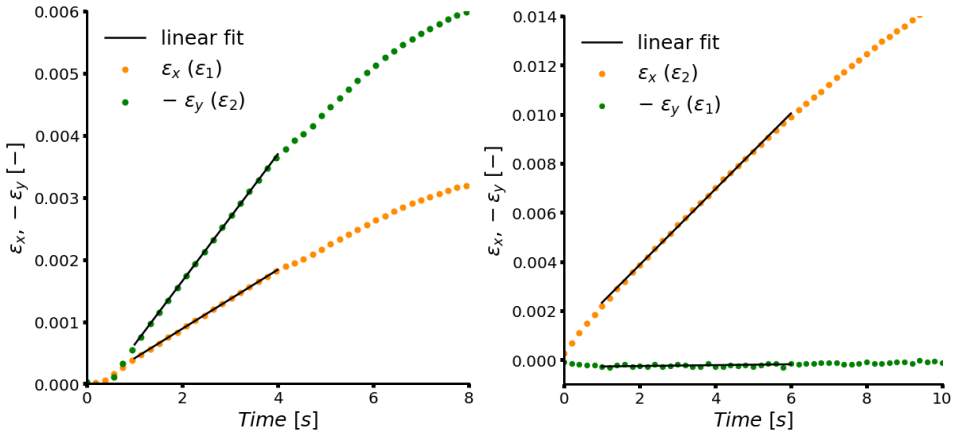


Figure 4.24: Strains ε_x and ε_y versus time for (a) quasi-static tensile tests with load applied in the fibers direction (direction 1). (b) Quasi-static tensile test with load in direction perpendicular to the fiber (direction 2).

In order to calculate an approximated values of the initial Poisson's ratio, the slope of the two strain-time curves have been evaluated fitting the first part of the curves with a linear function (black lines in Figure 4.24), avoiding the first experimental points influenced by possible initial misalignment. The Poisson's ratio has been calculated as the ratio of the two slopes.

It is important to remember, as explained in Section 4.2.1, that even values much greater than 1/2 are acceptable Poisson's ratios. The following condition must be satisfied:

$$|\nu_{ij}| < \sqrt{\frac{E_i}{E_j}} \tag{4.54}$$

Figure 4.25a and b shows respectively the limits of $|\nu_{12}|$ and $|\nu_{21}|$ according to Equation 4.54 evaluating E_1 and E_2 at different fiber volume fraction

respectively according to Equations 4.24 and 4.52. Validity region of the Poisson's ratio for the fiber-volume fractions considered in this work is highlighted. ν_{12} up to 40 are acceptable for this highly *orthotropic* composite, and only values very close to zero are acceptable for ν_{21}.

The filled black dots in Figure 4.25 are the experimental values. On average, ν_{12} is 2.16 ± 0.69 and ν_{21} ranges between 0.0002 and 0.02. The values of ν_{21} have a quite big dispersion due to the very low entity of the transversal contraction. Remembering Equation 4.4 from Section 4.2.1 it is

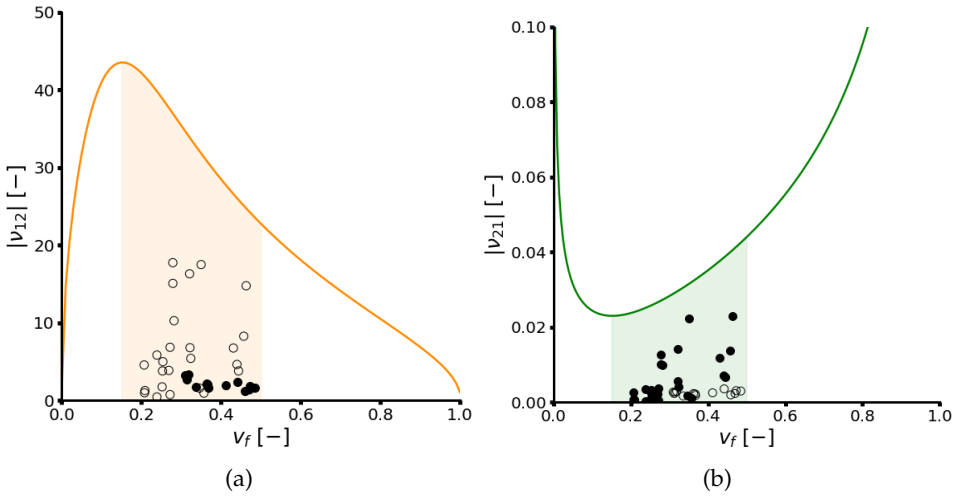


Figure 4.25: Theoretical limits of Poisson's ratios and experimental results. (a) The orange line shows the limits of $|\nu_{12}|$ according to Equation 4.54. Validity range for the Poisson's ratio for the fiber-volume fractions considered in this work is highlighted. The filled black dots are the experimental values. The empty dots are the ν_{12} values calculated with Equation 4.4 from the ν_{21} experimentally evaluated. (b) The green line shows the limits of $|\nu_{21}|$ according to Equation 4.54. The area of validity of the Poisson's ratio for the fiber-volume fractions considered in this work is highlighted. The filled black dots are the experimental values. The empty dots are the ν_{21} values calculated with Equation 4.4 from the ν_{12} experimentally evaluated.

possible to predict ν_{21} from ν_{12} and vice versa knowing the values of E_1 and E_2. Considering the *spring-in-parallel* model for E_1 and the new model described in Section 4.4.3.2 for E_2, the converted ν_{21} and ν_{12} have been calculated and compared to experimental values in Figure 4.25. Despite the big dispersion of the data from quasi-static tensile tests with load in direction 2, the prediction is adequate.

4.4.5 Determination of G_{12}

4.4.5.1 Experimental results

The in-plane shear modulus G_{12} has been measured according Standard ASTM D3518 [64]. An overview of the experimental procedures adopted in literature to calculate the in-plane shear modulus can be found in the work carried out by Magni [65]. In his work it is showed that, among the others, the procedure described in Standard ASTM D3518 is the most appropriate for soft matrix fiber-reinforced composites. According to Standard ASTM D3518 [64], in order tho measure the in-plane shear properties of a lamina, quasi static tensile tests on symmetric-balanced laminates with plies oriented at $\pm 45^\circ$ with respect to the length of the laminate can be performed. The theory is based on considerations from the CLT (Section 4.2.3). In a symmetric-balanced $\pm 45^\circ$ angle-ply laminate subjected to a load along the length of the laminate, shear strains are null ($\gamma_{xy} = 0$) and shear stresses alternate in sign from the laminae oriented at $+45^\circ$ to the laminae oriented at -45°, so that the resulting shear stress is zero.

Recalling the transformation equations 4.10, 4.11 and 4.12, the in-plane shear stress τ_{12} can been calculated as:

$$\tau_{12} = \frac{F}{2\ w_0\ t_0} = \frac{\sigma_x}{2} \tag{4.55}$$

where F is the load measured, w_0 is the initial width of the specimen and t_0 is the initial thickness of the specimen. The shear strain γ_{12} can been calculated as:

$$\gamma_{12} = \varepsilon_x - \varepsilon_y \tag{4.56}$$

where ε_x and ε_y are engineering longitudinal and transversal strains, respectively in the load direction and in the perpendicular direction. Tests have been performed on rectangular specimens with stacking sequence $[+45, -45]_{2S}$, width $w_0 = 25\ mm$, thickness ranging from 0.78 mm and 2.31 mm and with a gauge length of 210 mm. The fiber-volume fraction ranged between 0.21 and 0.41. Tests have been performed at strain rate of 0.12 $1/s$. Twenty-five specimens have been tested. ε_x and ε_y have been measured optically with DIC.

Before showing the experimental results, few considerations about the

approximations in this testing procedure have to be made. Since at the two ends of the specimen the fibers are not free to move, as they are partially fixed into the clamping system, only a central area of the specimen in which the influence of the clamped region can be neglected, is considered for the measurement of the strains. A schematic view of the analyzed area of the specimens is showed in Figure 4.26.



Figure 4.26: Schematic view of the analyzed area of the specimen employed for the measurement of the in-plane shear modulus G_{12}.

The strain state at 45° to the $x-y$ axis of the specimen is a pure shear if $|\varepsilon_x| = |\varepsilon_y|$. This can be showed with the strain Mohr's circle representation [66]. The strain Mohr's circle is a representation of a plane state of strains which allows to easily find the principal strains in a body subjected to a certain strain state. Given ε_x, ε_y and γ_{xy}, the Mohr's circle consists in a circle passing through the two points of coordinates (ε_x, $-\gamma_{xy}/2$) and (ε_y, $\gamma_{xy}/2$). The principal directions correspond to the intersections with the x axis (when shear strains are zero), while a state of pure shear correspond to the intersections with the y axis (when normal strains are zero). If the laminate principal directions are aligned to the $x-y$ plane ($\gamma_{xy} = 0$), as is expected for a symmetric-balanced $\pm 45°$ angle-ply laminate, a state of pure shear is present at 45° to the $x-y$ axis of the specimen (90° in the Mohr reference) if $|\varepsilon_x| = |\varepsilon_y|$ (Figure 4.27a). If $|\varepsilon_x| \neq |\varepsilon_y|$, small tensile or compressive strains exist in addition to the relatively large shear strains in the principal directions of the lamina (Figure 4.27b). The center of the Mohr's cycle can be calculated as:

$$\varepsilon_{c_{Mohr}} = \frac{\varepsilon_x + \varepsilon_y}{2} \tag{4.57}$$

Another consideration has to be made about fibers reorientation. During loading, fibers tend to orient toward the longitudinal direction and in the case of specimens with deformable matrices the reorientation can be significantly high. This may lead to an unacceptable violation of the assumptions of this method. According to Standard ASTM D3518 [64] the methods is acceptable if the fibers reorientation is less then 1.5°. In

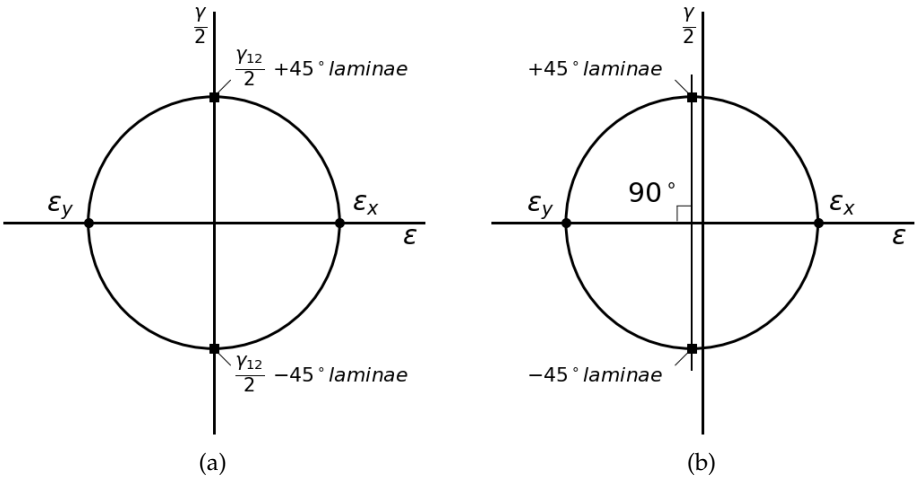


Figure 4.27: Strain Mohr's circle representations. (a) State of plane strain in which $|\varepsilon_x| = |\varepsilon_y|$. (b) State of plane strain in which $|\varepsilon_x| < |\varepsilon_y|$. Small compressive strains exist at 45° to the x-y axis of the specimen.

order to estimate the fibers reorientation, the following geometric approach has been used. Consider a lamina at a time $t = t_0$, characterized by an initial width, w_0, and with the fibers oriented at an angle ϑ_0 to the loading direction, as reported in Figure 4.28. All the fibers are assumed to have the same length, d, and they can be considered inextensible ($E_f >> E_m$). As the lamina is stretched, at a generic time $t = t_i$ its width, w_i, reduces and causes the fibers to tilt. The fibers angle reached can be related to the strain measured perpendicularly to the loading direction, ε_y, as:

$$\varepsilon_y = \frac{w - w_0}{w} = \frac{d\ sin\vartheta - d\ sin\vartheta_0}{d\ sin\vartheta_0} \tag{4.58}$$

thus,

$$sin\vartheta = (\varepsilon_y + 1)\ sin\vartheta_0 \tag{4.59}$$

On the tested specimens, a reorientation of 1.5° is reached for $|\varepsilon_x|$ and $|\varepsilon_y|$ less than 0.03. In this range of deformations $|\varepsilon_x|$ and $|\varepsilon_y|$ almost coincide, the center of Mohr's circle at fibers reorientation of 1.5° is on average $\varepsilon_{c_{Mohr}} = -0.00016 \pm 0.00089$. This slight compression present in the principal directions of the lamina can be assumed negligible, considering that γ_{12} is 0.053 ± 0.002 that is more than two order of magnitude higher than $\varepsilon_{c_{Mohr}}$. Thus, a state of almost pure shear is actually present in the

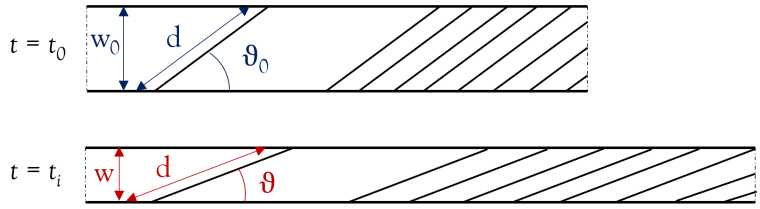


Figure 4.28: Schematic representation of fibers reorientation in a lamina of the specimen during loading.

specimens. Figure 4.29 shows the variation of $\varepsilon_{c_{Mohr}}$ and fibers angle ϑ calculated according to Equation 4.58 versus the test time of specimens with fiber-volume fraction $v_f = 0.31$. Figure 4.30 shows the shear stress

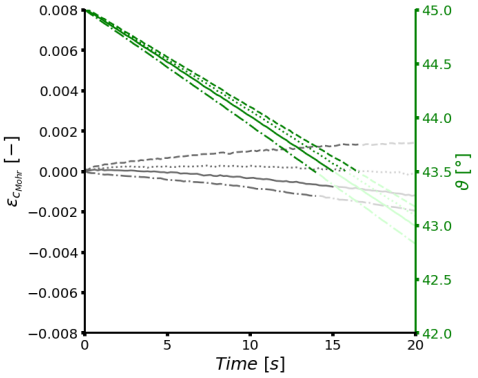


Figure 4.29: Coordinate of the center of the Mohr's circle $\varepsilon_{c_{Mohr}}$ and fibers angle ϑ versus the test time of specimens with fiber-volume fraction $v_f = 0.31$. The lines in pale colors are the values for which $\Delta\vartheta > 1.5°$.

τ_{12} - shear strain γ_{12} curves calculated according Equations 4.55 and 4.56 in the range of validity above explained ($\vartheta < 1.5°$) for specimens with fiber-volume fraction $v_f = 0.26$, $v_f = 0.31$ and $v_f = 0.37$. As can be seen, the stress-strain curves are not linear. A strain level of $\gamma_{12} = 0.005$ has been adopted as upper limit for linear behavior. The shear modulus G_{12} was then calculated as the slope of a linear fitting of the curve in this strain range. The shear moduli so calculated for all the tested specimens versus the respective fiber-volume fraction are showed in Figure 4.31. As previously observed for the modulus E_2, also the values of the shear modulus exponentially increase with fiber-volume fraction, reaching values almost 30 times greater than the shear modulus of the matrix alone.

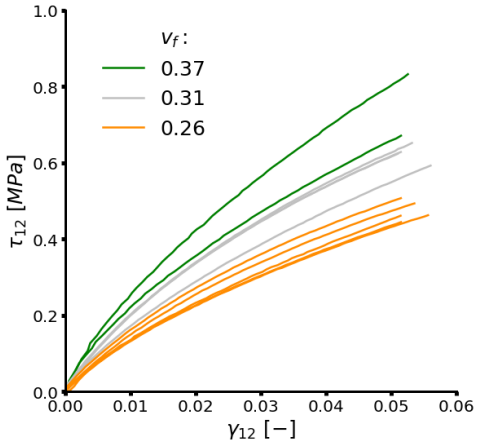


Figure 4.30: Shear stress τ_{12} - shear strain γ_{12} curves up to fibers reorientation $\vartheta = 1.5°$ for specimens with fiber-volume fraction $v_f = 0.26$, $v_f = 0.31$ and $v_f = 0.37$.

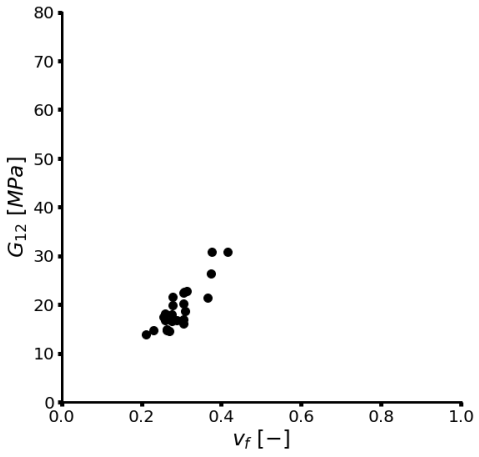


Figure 4.31: Shear modulus G_{12} calculated as the slope of the linear fit of the τ_{12} - γ_{12} curves in the range $0 < \gamma_{12} < 0.005$, versus fiber-volume fraction.

4.4.5.2 Micromechanical models

A comparison of the experimental values obtained with the *spring-in-series* model described with Equation 4.30 is showed in Figure 4.32 (continuous line). As for modulus E_2, also the experimental values of the shear modulus are significantly higher than the values predicted by the *spring-in-series* model. On the contrary, as can be seen in Figure 4.32, dashed line, Halpin-Tsai approach (Equation 4.31), in this case, is able to predict the trend of the experimental results with a fibers reinforcement factor $\xi = 36.8$. Even if this value is extremely high and thus a physical interpretation is not possible, this model can be used to predict the values of the shear modulus for the composite under study for fiber-volume fraction from 0.2 to 0.5.

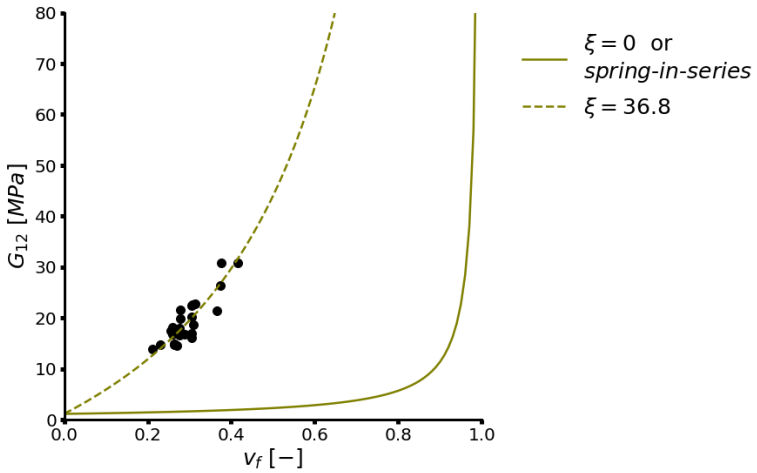


Figure 4.32: Shear modulus, G_{12} versus fiber-volume fraction, v_f. Comparison of experimental data with *spring-in-series* model (Equation 4.30) and Halpin-Tsai Equation (Equation 4.31). ξ is the fibers reinforcement factor.

4.4.6 Summary and conclusive remarks

In this section the mechanical characterization at small strains of laminae of GF-PDMS composite with several fiber-volume fractions have been showed. All four independent material constants have been experimentally measured and the results have been compared with theoretical models. Quasi-static tensile tests on specimens with fibers oriented in the loading direction have been employed for the determination of the modulus E_1 and for the Poisson's ratio ν_{12}, and two approaches have been showed to

be effective in resolving the clamping issue. Quasi-static tensile tests on specimens with fibers oriented at 90° to the loading direction have been employed of the characterization of the modulus E_2 and the Poisson's ratio ν_{21}, while symmetric-balanced $\pm 45°$ angle-ply laminates have been employed for the characterization of the in-plane shear modulus G_{12}. From a micromechanical point of view, theoretical models that are able to predict the moduli of the composite, given the properties of the constituent materials and the their volume ratios, have been found.

Poisson's ratios ν_{12} and ν_{21} have been found to be reasonably constant over the range of fiber-volume fraction considered ($0.15 < v_f < 0.50$). The modulus E_1 can be correctly predicted with the simple *spring-in-parallel* model as for rigid matrix fiber-reinforced composites [1]. The modulus G_{12} can be predicted using the Halpin-Tsai approach with an empirical fibers reinforcement factor $\xi = 36.8$. This value of ξ is significantly higher than the values typically found for rigid matrix fiber-reinforced composites. A novel model have been proposed for the prediction of the modulus E_2, which could not be predicted by Halpin-Tsai model with empirical ξ. The new model, although still merely empirical, is consistent with the possible stiffer behavior exhibited by nearly incompressible materials such as the elastomeric matrix of the composite considered, if confined between rigid bodies such as glass fibers.

Overall, the present study proposes an experimental test setup suitable for the characterization of fiber-reinforced elastomers which, due to the huge difference between matrix and fibers properties, are not trivial to characterize and attention must be paid to obtain reliable results. Furthermore, the present study proposes tools to predict the properties of laminae of fiber-reinforced elastomeric composites.

4.5 Symmetric-balanced laminates: stress-strain behavior at large strains

4.5.1 Introduction

The characterization of elastomeric matrix composites, such as the one in the present study, cannot be limited to the study of its behavior at small deformations, since, unlike traditional composites with rigid matrix, the

peculiarity of these composites is precisely that of being able to reach high levels of deformation. The ability to achieve high levels of deformation in these composites may not be evident when examining the lamina loaded along its principal directions. In fact, from the tests performed to determine moduli E_1 and E_2, the deformations at break of the lamina were found to be relatively limited. On the other hand, the study of symmetric-balanced laminates showed a mechanical response whose characterization at small strains would be very limited in describing the behavior of the laminate. In Section 4.4.5 the shear stress-strain curves were showed limiting to a very small range of strains in which the equations to calculate the shear modulus were valid. In this section the behavior of the symmetric-balanced laminates $[+45, -45]_{2S}$ extended to the entire strain range reached and that of other symmetric-balanced laminates $[+30, -30]_{2S}$, $[+60, -60]_{2S}$ and $[+75, -75]_{2S}$ will be showed.

All of these laminates exhibit a very peculiar behavior whose interpretation requires the understanding of the mechanical behavior of the elastomeric matrix. Therefore, some considerations on elastomers and elastomeric matrix composites will be also included.

4.5.2 Quasi-static tensile tests

Similarly to the tests performed for small strains characterization (Section 4.4), quasi-static tensile tests were performed with an INSTRON 5967 universal testing machine equipped with a 2 kN load cell. Tests have been performed under displacement control at nominal strain rate of 0.12 $1/s$, in a controlled environment at 23°C and 50% of relative humidity. Engineering strains in the x and y directions have been measured locally, with a digital image correlation (DIC) system. The tensile tests were observed with a UI-5490SE camera (sensor size 12.7 mm) mounting a NIKON 28-105 objected and the images analyzed with VIC2D-2009 software. The distance between the camera and the specimen was about 1 m.

Tests have been performed on rectangular specimens. The fiber-volume fraction of all the specimens were kept constant, at a value of $v_f = 0.3$. Six $[+45, -45]_{2S}$ specimens with width $w_0 = 25$ mm, thickness $t_0 = 2$ mm and a gauge length of 210 mm have been tested, while four specimens for configuration $[+30, -30]_{2S}$, $[+60, -60]_{2S}$ and $[+75, -75]_{2S}$ with width $w_0 = 12.5$ mm, thickness $t_0 = 2$ mm and a gauge length of 50 mm have

been tested. $[+45, -45]_{2S}$ specimens are larger in size because they are the same used in Section 4.4.5 where the indications of the Standard ASTM D3518 [64] were followed to measure the shear modulus. For the characterization of the properties at large deformations, instead, the small square mold 80 *mm* x 80 *mm* were used, which allowed an easier preparation of the laminates.

For the analysis of the properties of the laminates at large deformations the calculation of true stresses and true strains is necessary because width, thickness and length variation during the test is not negligible as in the evaluation of the properties at small strains. For each specimen, the true stress in loading direction has been calculated as:

$$\sigma_{x\ true} = \frac{F}{w\ t} \tag{4.60}$$

where F is the load measured, w is the actual width of the specimen and t is the actual thickness of the specimen. The actual width and thickness have been calculated as:

$$\begin{aligned} w &= w_0\ (\varepsilon_y + 1) \\ t &= t_0\ (\varepsilon_z + 1) \end{aligned} \tag{4.61}$$

Strains in x and y directions ε_x and ε_y have been evaluated in the central area of the specimens, in which the influence of the clamped region can be negligible. Figure 4.33 shows an illustration of the area employed in the measurement of strains, (red rectangle) and areas where the specimen is not free to deform because the fibers have one end blocked between the clamps (yellow crosses) for the different stacking sequences.

Strain in z direction ε_z has been evaluated on the hypothesis that the volume remain constant during deformation. This is a reasonable hypothesis considering that the elastomeric matrix is almost incompressible and the fibers are practically inextensible, due to the huge difference between their modulus and the matrix modulus. Furthermore, an experimental evidence of the validity of this hypothesis and thus of the accuracy of the value of the strain in z direction calculated, can be found in the work of Magni [65].

If an elementary cube of material, with undeformed dimensions $L_{x0} = L_{y0} = L_{z0}$ is stretched, it deforms in a parallelogram with edges length L_x,

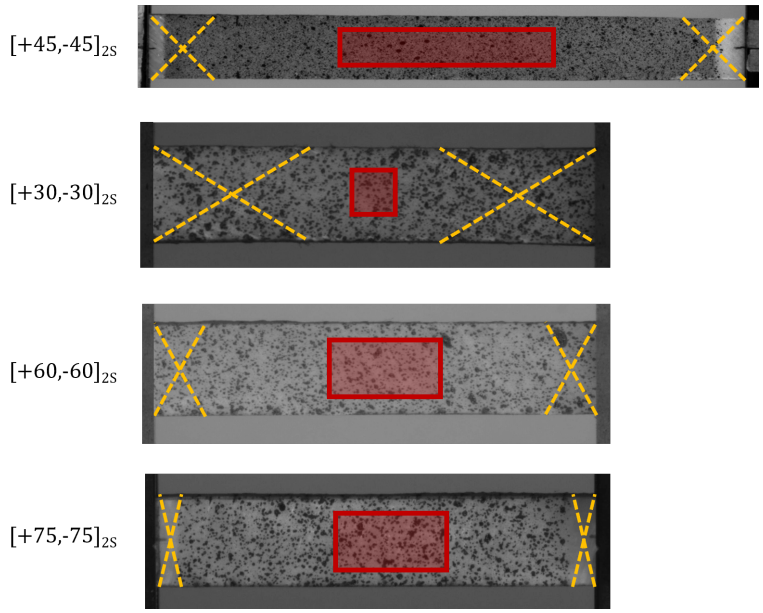


Figure 4.33: Illustration of the area employed for measurement of strains ε_x and ε_y (red rectangle) and areas where the specimen is not free to deform because the fibers have one end blocked between the clamps (yellow crosses).

L_y and L_z. On the hypothesis of constant volume:

$$L_{x0}\ L_{y0}\ L_{z0} = L_x\ L_y\ L_z \tag{4.62}$$

thus, remembering the definition of draw ratios λ_i:

$$\lambda_i = \frac{L_i}{L_{i0}} = \varepsilon_i + 1 \tag{4.63}$$

$$\frac{L_x\ L_y\ L_z}{L_{x0}\ L_{y0}\ L_{z0}} = 1 = \lambda_x\ \lambda_y\ \lambda_z \tag{4.64}$$

and,

$$\varepsilon_z = \lambda_z - 1 = \frac{1}{\lambda_x\ \lambda_y} - 1 = \frac{1}{(\varepsilon_x + 1)\ (\varepsilon_y + 1)} - 1 \tag{4.65}$$

True strains $\varepsilon_{i\ true}$ can be calculated from engineering strains ε_i as:

$$\varepsilon_{i\ true} = ln(\varepsilon_i + 1) \qquad \text{for } i = x, y, z \tag{4.66}$$

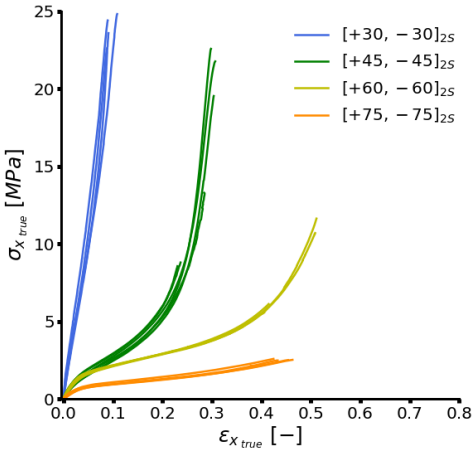


Figure 4.34: True stress-true strain curves $\sigma_{x\ true} - \varepsilon_{x\ true}$ of symmetric-balanced laminates $[+30, -30]_{2S}$, $[+45, -45]_{2S}$, $[+60, -60]_{2S}$ and $[+75, -75]_{2S}$.

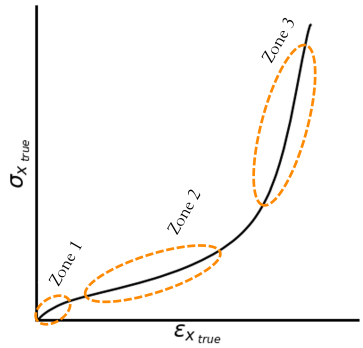


Figure 4.35: True stress-true strain curves $\sigma_{x\ true} - \varepsilon_{x\ true}$ of a symmetric-balanced laminates $[+45, -45]_{2S}$. Three different zones can be identified: initial region at low ε_x (Zone 1), intermediate "softened" region (Zone 2) and final stiffening region at high ε_x (Zone 3).

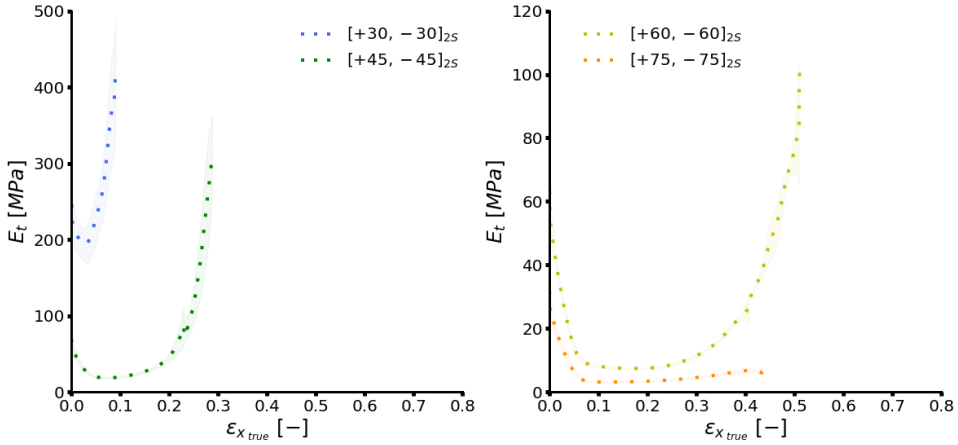
First, stress - strain curves in loading direction will be analyzed. Figure 4.34 shows the true stress - true strain curves $\sigma_{x\ true} - \varepsilon_{x\ true}$ of the tested specimens. In these curves, three main zones can be qualitatively highlighted, as showed in Figure 4.35:

- Zone 1 is an initial region that characterizes the initial stiff response of the laminate. This zone includes the region in which the shear

modulus G_{12} has been previously calculated in $[+45, -45]_{2S}$ laminates.

- Zone 2 is an intermediate "softened" region, in which the laminate shows a response less stiff then the response in Zone 1. It extends for a wide range of strains with almost constant slope.
- Zone 3 is a final "strain hardening" region in which the laminate stiffness increases progressively up to failure.

To have a better perception of the variation of the slope of the $\sigma_{x\ true} - \varepsilon_{x\ true}$ curves, the tangent modulus E_t, has been calculated as the slope of each curve. The mean values of the tangent modulus E_t for each laminates type versus $\varepsilon_{x\ true}$ is showed in Figure 4.36a and b. All the laminates



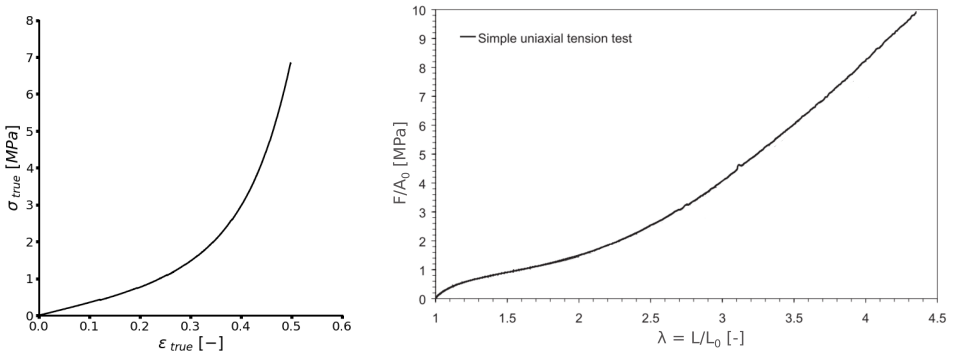
(a) (b)

Figure 4.36: (a) Tangent modulus E_t versus $\varepsilon_{x\ true}$ for $[+30, -30]_{2S}$ and $[+45, -45]_{2S}$ laminates. (b) Tangent modulus E_t versus $\varepsilon_{x\ true}$ for $[+60, -60]_{2S}$ and $[+75, -75]_{2S}$ laminates.

show an initial reduction of the tangent modulus, followed by a region in which the modulus remains constant. The further increase of stiffness at larger deformation can be seen only for $[+30, -30]_{2S}$, $[+45, -45]_{2S}$ and $[+60, -60]_{2S}$ laminates, while in $[+75, -75]_{2S}$ the specimens break during the second stage.

It is possible to notice some analogies between this behavior and the one showed by elastomers and elastomeric composites in general. First

of all, Figure 4.37a reports the true stress - true strain curve of the PDMS matrix under quasi-static tensile test. The typical behavior of a rubber-



(a) (b)

Figure 4.37: (a) True stress - strain curves $\sigma_{true} - \varepsilon_{true}$ of the PDMS Sylgard®184 during quasi-static tensile tests. Tests parameters are reported in A. (b) Stress - strain curve of carbon-black filled rubber under quasi-static uniaxial tensile test. Adapted from [67].

like material is showed with a first linear elastic response followed by an increase of stiffness due to stretching and realignment of the polymer chains of the rubber network [40]. Figure 4.37b shows the typical behavior of a rubber filled with carbon-black particles [67] subjected to uniaxial tension. A first initial stiff region is followed by a softening and then an hardening. The main physical interpretation of this behavior involves the presence of microstructural weak bonds at the rubber-particle interface that break if a strain is applied. This leads to the softening of the filled rubber at intermediate strains. Then, the polymer chains completely extended induce hardening [67]. The behavior of the symmetric-balanced laminates investigated in this work can be partially related with the behavior of filled rubber but the presence of long continuous fibers needs further considerations. For example, as already introduced in Section 4.4.3.2 the almost incompressible PDMS, when mechanically constrained between rigid fibers can shows a different response than that of unconstrained elastomer free to move.

Another aspect to be taken into account is the reorientation of the fibers of the laminate during loading. During loading the fibers tend to tilt toward the loading direction to accommodate the width contraction of the speci-

mens. This reorientation affects the mechanical response of the laminates, theoretically increasing the stiffness of the laminate as the angle between fibers and loading direction decreases. Applying the transformation rules introduced in Section 4.2.1 (Equation 4.15), knowing the properties of the lamina in principal directions, it is possible to predict the response of the lamina in any $x-y$ coordinate system. From the study of the properties of the single lamina showed in Section 4.4, the material constants of a single lamina of the symmetric laminates $[+\vartheta, -\vartheta]_{2S}$ with $v_f = 0.3$ can be calculated according to the equations summarized in Table 4.1.

Table 4.1: Equations employed to calculate the material constants in principal directions of a single lamina of the GF-PDMS composite with $v_f = 0.3$. The equations are based on the experimental study described in Section 4.4.

Material constant	Equation	Calculated value
E_1	$E_1 = E_f v_f + E_m v_m$ *	21602 MPa
E_2	$E_2 = \dfrac{E_f E_m (1 + A\ v_f{}^b)}{(1 - v_f) E_f + v_f E_m (1 + A\ v_f{}^b)}$ *	17.26 MPa
G_{12}	$G_{12} = G_m \dfrac{1 + \xi \eta v_f}{1 - \eta v_f}$ * **	19.53 MPa
ν_{12}	*constant*	2.16

* $E_f = 72000\ MPa$, $E_m = 3.3\ MPa$, $v_m = 1 - v_f$, $A = 54$, $b = 2.5$, $G_f = 30000\ MPa$, $G_m = 1.1\ MPa$, $\xi = 36.8$

** $\eta = \frac{(G_f/G_m)-1}{G_f/G_m+\xi}$

Starting from these material properties, the variation in a single lamina of the modulus E_x with ϑ has been calculated and is showed in Figure 4.38. Decreasing the angle ϑ between direction 1 and x, E_x increases, that is the response to a load in x direction is expected to be stiffer.

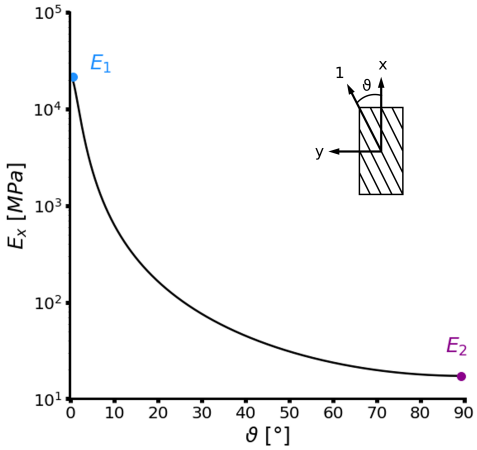


Figure 4.38: Variation of the modulus E_x versus the angle ϑ between direction x and direction 1. Note that y axis is in logarithmic scale.

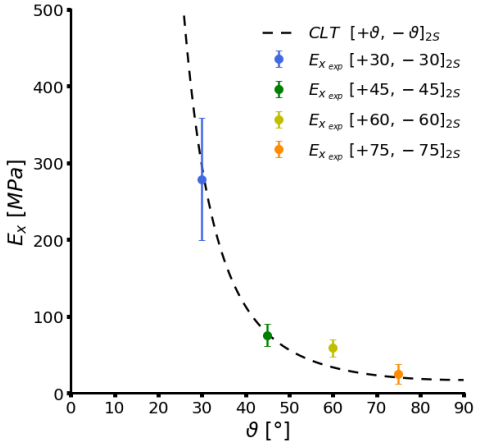


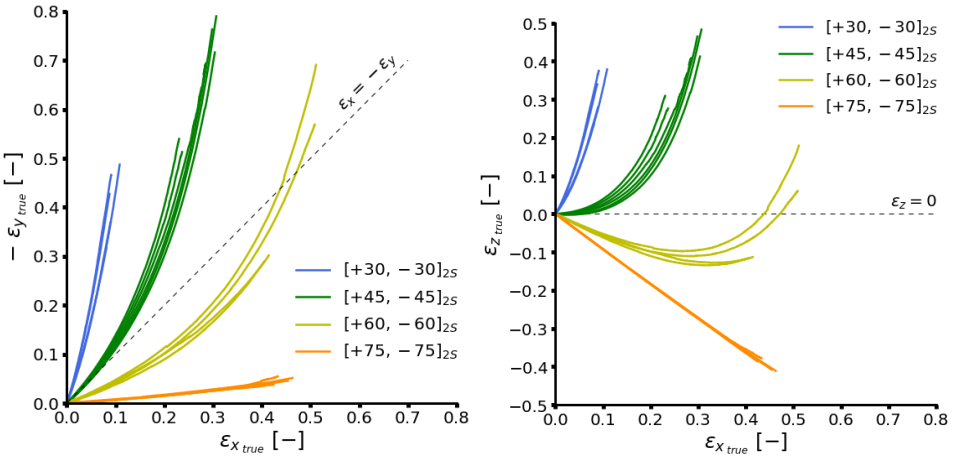
Figure 4.39: Variation of the modulus $E_{x\ \mathrm{CLT}}$ versus the fiber angle ϑ.

From the properties of the single lamina, it is also possible to predict the behavior of the laminate, by means of the Classical Lamination Theory (CLT), as described in Section 4.2.3. Calculated the ABD matrix from the properties of the lamina and the stacking sequence of the laminate, in order to predict its response in a uniaxial tensile test a force per unit width in x direction $N_x = 10\ N/mm$ has been assumed, and the response of the laminate in terms of strains can be calculated applying the inverse of Equation 4.44 and Equation 4.38. The modulus of the laminates $E_{x\ \mathrm{CLT}}$ can be than calculated as:

$$E_{x\ \mathrm{CLT}} = \frac{N_x/t}{\varepsilon_x} \tag{4.67}$$

where N_x is the force per unit width applied in x direction, t is the thickness of the specimen equal to 2 mm and ε_x is the strain of the laminate in x direction.

The modulus $E_{x\ \mathrm{CLT}}$ calculated for $[+\vartheta, -\vartheta]_{2S}$ with $0 < \vartheta < 90°$ is showed in Figure 4.39 (dashed line). The slope of the initial linear part of the stress - strain experimental curves respectively up to $\varepsilon_{x\ true} = 0.0025$ for $[+30, -30]_{2S}$ and $[+45, -45]_{2S}$ laminates and up to $\varepsilon_{x\ true} = 0.005$ for $[+60, -60]_{2S}$ and $[+75, -75]_{2S}$ has been calculated and compared with the theoretical prediction (dots in Figure 4.39). At such small strains, the prediction of the Classical Lamination Theory is close to the experimental values.



(a) (b)

Figure 4.40: (a) True strains in width direction $\varepsilon_{y\ true}$ versus true strain in longitudinal direction $\varepsilon_{x\ true}$. (b) True strains in thickness direction $\varepsilon_{z\ true}$ versus true strain in longitudinal direction $\varepsilon_{x\ true}$.

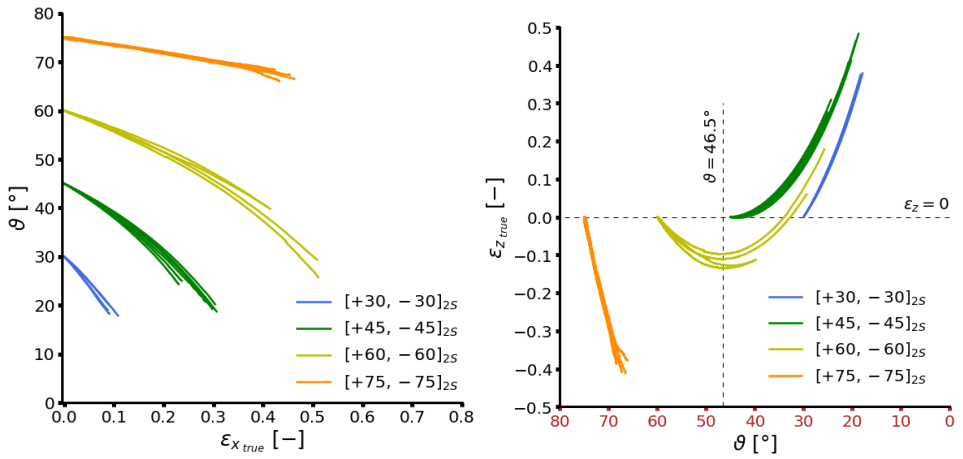
Considering higher deformations, the variation of true strains in y direction experimentally evaluated and the variation of true strains in z direction, calculated from ε_x and ε_y with Equation 4.65 for the different laminates are showed in Figure 4.40. Strains $\varepsilon_{y\ true}$ are always negative because they are associated to a width contraction: for the sake of simplicity, in the following considerations we will refer to $\varepsilon_{y\ true}$ as to its absolute value.

Strain $\varepsilon_{x\ true}$ coincides with $\varepsilon_{y\ true}$ at small strain in $[+45, -45]_{2S}$ laminate, as already showed in Section 4.4.5 in the discussion about the estimation of the shear modulus, then, $\varepsilon_{y\ true}$ became higher that $\varepsilon_{x\ true}$, which indicates that the width reduces more quickly at higher strains. In $[+30, -30]_{2S}$ laminates, $\varepsilon_{y\ true}$ is around three time higher that $\varepsilon_{x\ true}$, indicating a very quick width reduction. On the other hand, in $[+75, -75]_{2S}$ laminates, ε_y is lower than ε_x, indicating that for higher fibers angle the width reduction is less pronounced. In $[+60, -60]_{2S}$ laminates, initially $\varepsilon_{y\ true}$ in lower that $\varepsilon_{x\ true}$ and at high deformations increases to overcome it.

Strain $\varepsilon_{z\ true}$ shows a very peculiar behavior. In $[+30, -30]_{2S}$ and $[+45, -45]_{2S}$ laminates, $\varepsilon_{z\ true}$ is higher than zero, indicating that the thickness of the specimens increases during loading. A possible explanation is that the matrix is squeezed between the fibers and it is forced to expand in the z direction to maintain its volume. In $[+75, -75]_{2S}$ laminates, $\varepsilon_{z\ true}$ is always lower that zero, in this case the thickness decreases during loading as typically occurs in a tensile test on a elastomeric *isotropic* material. In $[+60, -60]_{2S}$ laminates $\varepsilon_{z\ true}$ initially decreases then increases and reaches values greater than zero: the thickness initially decreases, then starts to increase until the initial thickness of the specimen is exceeded. An experimental check of the observations was also carried out, and confirmed the reported observations. The experimental check is detailed in the work carried out by Magni [65].

During loading, as previously said, the fibers reorient. The fibers angle can be calculated through Equation 4.59 according to the approach explained in Section 4.4.5. Figure 4.41a, shows the evolution of the angle with $\varepsilon_{x\ true}$ for the different laminates. The angle varies considerably during loading and the rate at which decreases, increasing $\varepsilon_{x\ true}$, is greater for laminates with smaller initial angles. For $[+30, -30]_{2S}$ laminates, the fibers angle decreases on average of 1.2° for hundredth of $\varepsilon_{x\ true}$ with a maximum variation $\Delta\vartheta$ of 12°. For $[+45, -45]_{2S}$ laminates, the fibers angle decreases on average of 0.85° for hundredth of $\varepsilon_{x\ true}$ with a maximum variation $\Delta\vartheta$ of 26°. For $[+60, -60]_{2S}$ laminates, the fibers angle decreases on average of 0.56° for hundredth of $\varepsilon_{x\ true}$ with a maximum variation $\Delta\vartheta$ of 34°. For $[+75, -75]_{2S}$ laminates, the fibers angle decreases on average of 0.18° for hundredth of $\varepsilon_{x\ true}$ with a maximum variation $\Delta\vartheta$ of 9°.

It is interesting to correlate the behavior of $\varepsilon_{z\ true}$ with the variation of



(a) (b)

Figure 4.41: (a) Variation of fibers angle ϑ versus the strain in loading direction $\varepsilon_{x\ true}$. (b) Variation of $\varepsilon_{z\ true}$ versus ϑ. Note that ϑ varies from 80 to 0, to display the load increase during the test from left to right.

the fibers angle. In Figure 4.41b the evolution of $\varepsilon_{z\ true}$ versus ϑ is showed. ϑ is represented as decreasing from 80 to 0: the decreasing direction coincides with that of increasing $\varepsilon_{x\ true}$. A threshold beyond which the thickness of the specimens reverses its trend can be identified. For $\vartheta > 46.5°$ (identified as the point where the minimum of $\varepsilon_{z\ true}$ is located for laminates $[+60, -60]_{2S}$) the thickness of the specimens decreases during loading, for $\vartheta < 46.5°$ the thickness of the specimens increases during loading.

Further considerations can be done observing the tangent modulus E_t versus the fibers angle ϑ (Figure 4.42). The behavior at small strains is characteristic for each laminate, and it is close to the prediction of the CLT, than the composite becomes softer, even if the fibers are reorienting toward the loading direction (lower ϑ) which should theoretically contribute to increase the stiffness of the laminates (see Figure 4.38). The contribution of the elastomeric matrix at this stage is therefore predominant. The softening of the matrix can be assimilated to the typical behavior of filled rubbers, that shows a softening of the matrix when stretched, due to the breakage of the weak bonds created at the filler-rubber interface. This analogy will be also confirmed by the behavior of the laminates under cyclic loads that will be showed in Section 4.5.3. After the softening, $[+75, -75]_{2S}$ breaks, while the other three laminates exhibit an increase in stiffness that can be

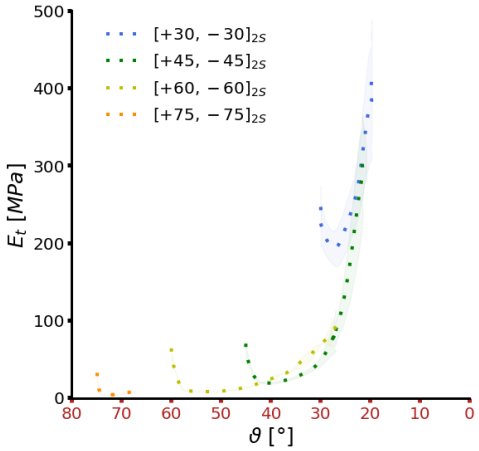


Figure 4.42: Tangent modulus E_t versus fibers angle ϑ of the different laminates.

related to both the hardening of the matrix and the fibers reorientation. In particular, $[+45, -45]_{2S}$ and $[+60, -60]_{2S}$ almost superimpose for $\vartheta < 40°$ and $[+30, -30]_{2S}$ superimposes $[+45, -45]_{2S}$ for $\vartheta < 25°$. Independently on the reached strain level, the laminates with the same actual fibers orientation exhibit the same stiffness, indicating that the contribution of the fibers orientation is now predominant.

In order to fully understand the behavior of these laminates it is thus fundamental consider both the contribution of the behavior of the matrix and the contribution of the fibers reorientation. With reference to Figure 4.35, we have showed that the contribution of the matrix is predominant in zone 2 while the contribution on the fibers reorientation is predominant in zone 3, but further investigation are needed to quantify the extent of the two contributions.

4.5.3 Cyclic load-unload quasi-static tensile tests

A further investigation in order to better understand the cause of the softening has been done performing some cyclic load-unload quasi-static tensile tests. The test set up is equivalent to that used for quasi-static tensile tests in Section 4.5.2. Tests have been performed on two rectangular specimens of $[+45, -45]_{2S}$ laminates with fiber-volume fraction $v_f = 0.24$, width $w_0 = 25\ mm$, thickness $t_0 = 2.5\ mm$ and a gauge length $L_0 = 210\ mm$. Tests have been performed at nominal strain rate of 0.12 $1/s$. For this

analysis only the engineering strains in x direction ε_x has been measured from the displacement ΔL of the crosshead as:

$$\varepsilon_x = \frac{\Delta L}{L_0} \tag{4.68}$$

Also the stress in x direction is the engineering one, calculated as:

$$\sigma_x = \frac{F}{w_0\, t_0} \tag{4.69}$$

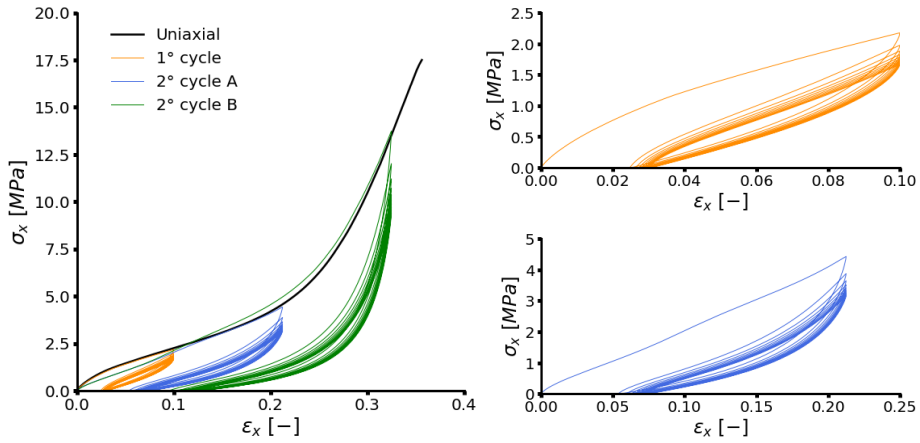


Figure 4.43: Engineering stress - strain curves for loading-unloading tests on $[+45, -45]_{2S}$ specimens. (a) Comparison of the three cyclic tests. (b) Up: Magnification of 1° cycle. Down: magnification of 2° cycle A.

Ten loading-unloading cycles were first performed up to $\varepsilon_x = 0.1$. The specimen was then removed from the clamping system and let to recovery at room temperature for 5 h. Then, ten further loading-unloading cycles were carried out up to $\varepsilon_x = 0.21$ in specimen A and up to $\varepsilon_x = 0.32$ in the second specimen B. Figure 4.43 shows the stress - strain curves for the first and the two second cycles compared to a monotonic tensile test of an identical specimen (afterwards called virgin specimen). The 1° cycle reaches a level of deformation that is just after the beginning of the zone with constant slope of the stress - strain curve of the virgin specimen (zone 2 in Figure 4.35). The 2° cycle A, blue cycles in Figure 4.43, reaches a deformation that corresponds to the zone in which the increase in slope of

the virgin specimen curve begins (beginning of zone 3 in Figure 4.35). The 2° cycle B, green cycles in Figure 4.43, reaches a strain which is in the final zone of the curve, close to the strain at break, in which the virgin specimen curve is very sharp.

At the end of the first loading-unloading cycle up to a deformation of 0.1, the laminate shows a residual deformation but at the following loading it responds by showing a behavior similar to the first loading and from the third to the tenth cycle the behavior does not differ much from the one observed during the second one. After the first series of loading-unloading cycles, the specimens are left free for 5 h and the deformation is recovered. During the second series of loading-unloading cycles, blue and green curves in Figure 4.43, the first load curve shows a lower slope than the initial one. The first zone of increased stiffness has disappeared. Both, after exceeding the maximum deformation of the 1° cycle follow a trend similar to that of the virgin specimen curve. After the first unloading also in this case a high residual strain is observed, which is greater for the cycle that reaches higher strains. The load curve of the following cycle shows slopes similar to the first load. From the third to the tenth cycle the behavior again does not differ much from that observed during the second loading-unloading cycle.

The behavior of these laminates when subjected to loading-unloading cycles is very similar to what can be observed in filled rubber [67]. In filled rubbers this behavior is usually called ”Mullins effect” and it is described as an appreciable stress-softening resulting from the first extension [67]. Specially at large strain, this behavior could be also related to a partial detachment of the fibers from the matrix but further analyzes are needed to fully understand the response of the material and to clarify the possible physical explanations.

4.5.4 Summary and conclusive remarks

In this section the behavior of symmetric-balanced laminates up to large deformations has been discussed. The GF-PDMS composites showed a highly non-linear response. The laminate responds with an initial stiff behavior followed by a softening and a further hardening at higher deformations. Two main contributions can be accounted to explain this behavior: fibers-matrix interactions at micro-scale and fibers reorientation. Fibers

reorientation toward the loading direction increases the stiffness of the laminate due to the increase in fibers contribution to the overall stiffness of the composite when the angle between fibers direction and loading direction decrease. The present study shows that the contribution of fibers orientation to laminate stiffening is not evident in the first stages of loading. The softened region can only be explained by considering other contributions, such as the Mullins effect or partial detachment between fibers and matrix. The presence of filler-rubber interactions was also supported by the behavior exhibited by the laminates subjected to cyclic loading. The subsequent hardening of the response of the laminates may instead be related mainly to fibers reorientation, because the response of the laminates becomes independent of the strain applied, when the softening region is exceeded. Looking at the composite kinematics, as increase in thickness, up to one and a half times the initial thickness of the laminates was observed when fibers angles less than 46° were reached.

The reported work can be considered as a great opening for further experimentation and investigations of the behavior of these particular composites that combines the field of laminates and that of elastomers.

4.6 Antisymmetric laminates: load coupling

4.6.1 Introduction

One of application to which fiber-reinforced elastomers are more promising is the soft robotics. Soft robots need to be able to perform wide motions triggered by inputs as simple as possible. Thanks to their anisotropy, and the consequent possibility to induce load coupling effects, combined with their deformability, fiber-reinforced elastomers have a huge potential for this type of applications. In this work extension-twist coupling will be investigated. Extension-twist coupling can be exhibited by antisymmetric laminates [1, 7]. A first preliminary theoretical study of the behavior of antisymmetric laminates with the Classical Lamination Theory (CLT) and numerical modeling with Finite Element Methods (FEM) will be followed by the description of the experimental campaign performed with a specifically designed experimental setup.

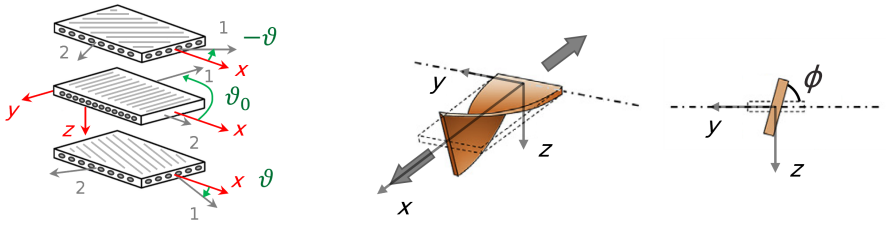
4.6.2 Preliminary study: CLT and FEM

A preliminary analysis has been carried out adopting the Classical Lamination Theory (CLT) to have a general overview of the behavior of an antisymmetric lamination sequence. The behavior of three-plies antisymmetric laminates with stacking sequence $[-\vartheta, 0, +\vartheta]$ and $[-\vartheta, 90, +\vartheta]$ has been investigated. As already discussed, the field of strains applied in the use of elastomer matrix composites can exceed the limit of linear elasticity, and thus CLT can be seen only as a simplified tool to tackle the problem of load coupling in this kind of composites. Nevertheless, this approach allows to get a first rough indication that can be refined in more complex analyzes. Further, it can give useful indications in the design of efficient experiments to investigate load coupling.

A theoretical GF-PDMS lamina with thickness $t_0 = 1\ mm$ and fiber-volume fraction $v_f = 0.42$ has been considered. Applying the equations listed in Table 4.1 the material constants of this lamina result $E_1 = 30242\ MPa$, $E_2 = 40.8\ MPa$, $G_{12} = 32.2\ MPa$ and $\nu_{12} = 2.16$. CLT can be applied to predict stresses and strains of the laminates, given forces and moments applied. Considering only a force applied in x direction $N_x \neq 0$, the inverse of Equation 4.44 in antisymmetric angle-ply laminates becomes:

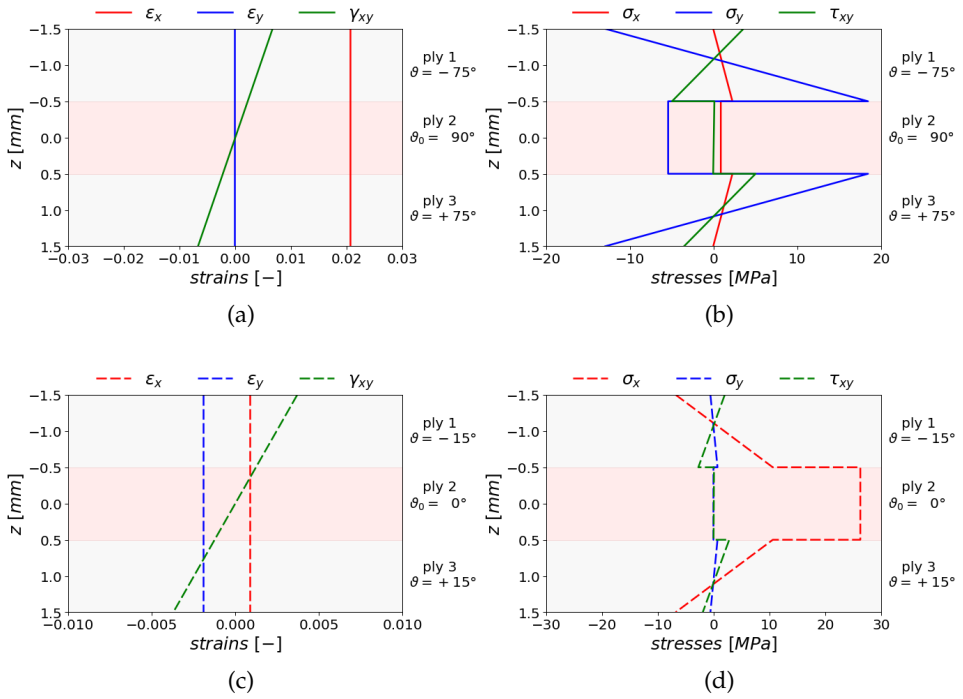
$$\begin{bmatrix} \varepsilon_x^o \\ \varepsilon_y^o \\ \gamma_{xy}^o \\ \kappa_x \\ \kappa_y \\ \kappa_{xy} \end{bmatrix} = \begin{bmatrix} A'_{11} & A'_{12} & 0 & 0 & 0 & B'_{16} \\ A'_{21} & A'_{22} & 0 & 0 & 0 & B'_{26} \\ 0 & 0 & A'_{66} & B'_{61} & B'_{62} & 0 \\ 0 & 0 & B'_{16} & D'_{11} & D'_{12} & 0 \\ 0 & 0 & B'_{26} & D'_{21} & D'_{22} & 0 \\ B'_{61} & B'_{62} & 0 & 0 & 0 & D'_{66} \end{bmatrix} \begin{bmatrix} N_x \\ 0 \\ 0 \\ 0 \\ 0 \\ 0 \end{bmatrix} \tag{4.70}$$

This implies that the shear strain in the middle surface γ_{xy}^o is null and between the curvatures, only κ_{xy}, the curvature along the $x-y$ plane, is not null, indicating that an extension-twist coupling is expected. An illustration of the expected extension-twist coupling along with a sketch of the antisymmetric lamination sequence adopted, oriented along the $x-y-z$ coordinates system is showed in Figure 4.44.



(a) (b)

Figure 4.44: (a) Sketch of the antisymmetric lamination sequence adopted, oriented along the $x-y-z$ coordinates system.(b) Sketch of the expected extension-twist coupling.



(a) (b)

(c) (d)

Figure 4.45: (a) Strains along the thickness (z coordinate) of a laminate with stacking sequence $[-75,90,+75]$ subjected to a force per unit width $N_x = 3\ N/mm$. (b) Stresses along the thickness (z coordinate) of a laminate with stacking sequence $[-75,90,+75]$ subjected to a force per unit width $N_x = 3\ N/mm$. (c) Strains along the thickness (z coordinate) of a laminate with stacking sequence $[-15,0,+15]$ subjected to a force per unit width $N_x = 30\ N/mm$. (d) Stresses along the thickness (z coordinate) of a laminate with stacking sequence $[-15,0,+15]$ subjected to a force per unit width $N_x = 30\ N/mm$.

Strains can be calculated with Equation 4.38 and stresses in each lamina can be calculated from Equation 4.41. Figure 4.45a and b show respectively strains and stresses along the thickness of a laminate with stacking sequence $[-75, 90, +75]$ subjected to a force per unit width $N_x = 3\ N/mm$. Figure 4.45c and d show respectively strains and stresses along the thickness of a laminate with stacking sequence $[-15, 0, +15]$ subjected to a force per unit width $N_x = 30\ N/mm$. As expected, strains are continuous along the thickness of the laminate, while stresses are not continuous among the plies. Since the laminate is antisymmetric, also strains and stresses are antisymmetric to the middle surface of the laminate ($z = 0$).

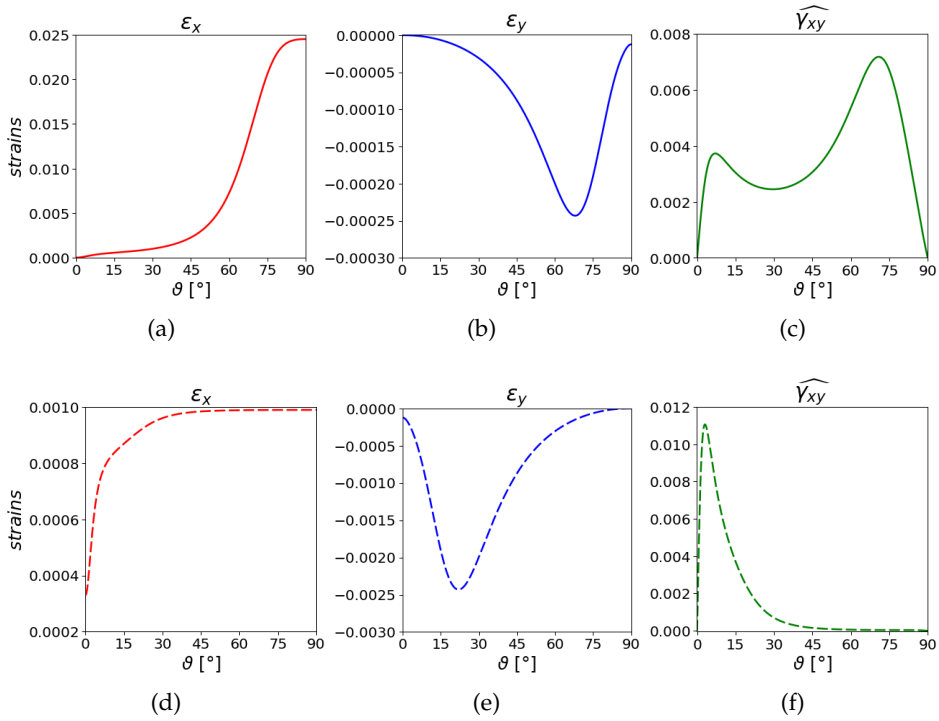
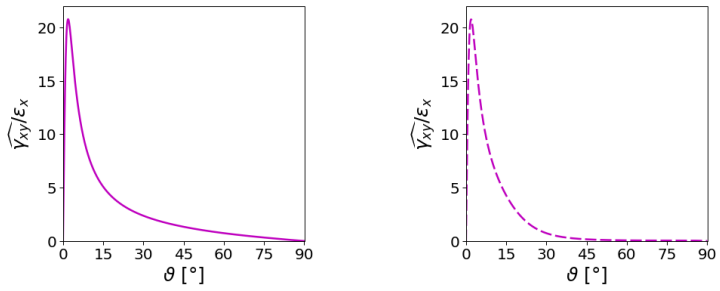


Figure 4.46: (a) ε_x (b) ε_y (c) $\widehat{\gamma_{xy}}$ versus ϑ for laminates $[-\vartheta, 90, +\vartheta]$ subjected to a force per unit width $N_x = 3\ N/mm$. (d) ε_x (e) ε_y (f) $\widehat{\gamma_{xy}}$ versus ϑ for laminates $[-\vartheta, 0, +\vartheta]$ subjected to a force per unit width $N_x = 30\ N/mm$.

Focusing on strains, ε_x and ε_y are constant along the thickness, while γ_{xy} is zero on the $z = 0$ surface of the laminate and then increases linearly, increasing $|z|$. In fact, $\gamma_{xy} = \gamma^o_{xy} + z\ \kappa_{xy}$. If the same calculation is done for any angle ϑ of the laminates $[-\vartheta, 90, +\vartheta]$ and $[-\vartheta, 0, +\vartheta]$ between 0° and 90° a change in the values of the stresses and strains is expected but

their trend in z is preserved. Therefore, if we call $\widehat{\gamma_{xy}}$ the value of the shear strain at $z = -1.5$ (its maximum value), ε_x, ε_y and $\widehat{\gamma_{xy}}$ can show the overall laminate behavior for any ϑ between $0°$ and $90°$. Figure 4.46a, b and c show respectively ε_x, ε_y and $\widehat{\gamma_{xy}}$ versus ϑ for the laminate $[-\vartheta, 90, +\vartheta]$. Figure 4.46d, e and f show respectively ε_x, ε_y and $\widehat{\gamma_{xy}}$ versus ϑ for the laminate $[-\vartheta, 0, +\vartheta]$.

Strains change considerably with ϑ. In particular, ϑ for which $\widehat{\gamma_{xy}}$ is maximum can be individuated. A laminate with that value of ϑ will show higher twisting, given the same force applied. In laminate $[-\vartheta, 90, +\vartheta]$ the maximum of $\widehat{\gamma_{xy}}$ corresponds to $\vartheta = 71°$, in laminate $[-\vartheta, 0, +\vartheta]$ the maximum of $\widehat{\gamma_{xy}}$ corresponds to $\vartheta = 3°$. In order to evaluated the configuration that theoretically will show the maximum extension-twist coupling the values of $\widehat{\gamma_{xy}}/\varepsilon_x$ has been evaluated and it is showed versus ϑ in Figure 4.47a and b respectively for laminates $[-\vartheta, 90, +\vartheta]$ and $[-\vartheta, 0, +\vartheta]$. The ratio between $\widehat{\gamma_{xy}}$ and ε_x shows a maximum for both the configurations at $\vartheta = 2°$. $[-\vartheta, 90, +\vartheta]$ laminates show higher twisting for ϑ around $70°$ but at this fibers orientation also ε_x is high.



(a) (b)

Figure 4.47: (a) $\widehat{\gamma_{xy}}/\varepsilon_x$ versus ϑ for laminates $[-\vartheta, 90, +\vartheta]$. (b) $\widehat{\gamma_{xy}}/\varepsilon_x$ versus ϑ for laminates $[-\vartheta, 0, +\vartheta]$.

According to the theoretical calculation with CLT, the larger extension-twist coupling will be exploited for antisymmetric laminates with the external layer oriented almost toward the loading direction. However other considerations has to be done regarding the load applied to reach a certain twisting. In some applications could be more important to obtain a twisting applying only small longitudinal loads, than applying small longitudinal deformations. The correlation between twisting and applied load will be

discussed in Section 4.6.4 when theoretical predictions and experimental measurements will be compared.

As part of the preliminary study, finite element simulations of selected antisymmetric configurations were also performed. The software used was Abaqus 2018. A rectangular shell planar part (element type: conventional shell) with width $w = 25\ mm$, length $l = 90\ mm$ were designed. A composite layup with 3 layers of thickness $t = 0.18\ mm$ was adopted and the rotation angle of the layers was defined according to the following stacking sequence: $[-15, 90, +15]$, $[-30, 90, +30]$, $[-45, 90, +45]$, $[-60, 90, +60]$, $[-75, 90, +75]$. Dimensions of the specimens and stacking sequence selected are the same also adopted in the experimental campaign. An elastic material (type: Engineering Constants) was defined with the material constants listed in Table 4.2.

Table 4.2: Material constants assigned for the finite element simulation of the laminate.

Material constant	Value
E_1	30242 MPa
E_2	40.8 MPa
E_3	40.8 MPa
ν_{12}	2.16
ν_{13}	2.16
ν_{23}	$-^*$
G_{12}	32.2 MPa
G_{13}	32.2 MPa
G_{23}	$-^*$

* ν_{23} and G_{23} are not showed because the simulation does not depend on the values of these two constants.

They are the material constants in principal directions of a single lamina of GF-PDMS composite with $v_f = 0.42$ (the fiber-volume fraction of the specimens employed also in the experimental campaign), calculated from the micromechanical models derived from the experimental study described in Section 4.4. Three studies with different boundary and loading conditions have been performed:

- Case A: no kinematic constrains, loads acting in x direction applied at the two opposite sides (Figure 4.48a);
- Case B: encastred on one side, load applied in x direction on the opposite side (Figure 4.48b);
- Case C: encastred on one side, constrained in y and z direction on the opposite side, load applied in x direction on the side not encastred (Figure 4.48c).

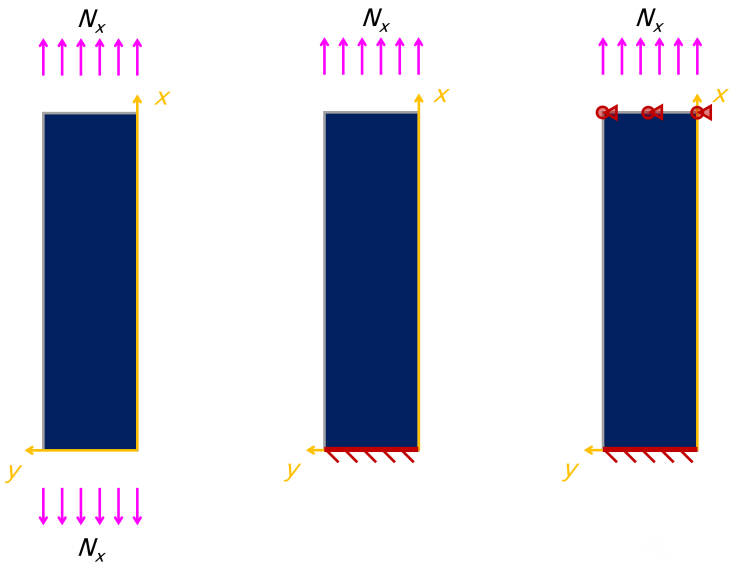


Figure 4.48: Boundary conditions and loads applied in the finite element models. (a) No kinematic constrains, loads acting in x direction applied at the two opposite sides. (b) Encastred on one side, load applied in x direction on the opposite side. (c) Encastred on one side, constrained in y and z direction on the opposite side, load applied in x direction on the side not encastred.

Case A simulates the configuration applied for the theoretical studied performed with the CLT. Case B and C simulate a configuration similar to the one employed in the experimental campaign which allowed to measure the twisting angle (Case B) and the torque applied by the specimen if the twisting is hindered (Case C). A rectangular mesh with quad-dominated S4R elements with seeds distance 0.5 mm has been applied for all the

simulations. Simulations with the non-linear effects of large deformations included (*Nlg ON*) or ignored (*Nlg OFF*) have been compared.

Figure 4.49 and Figure 4.50 show the displacement in z direction w_o obtained applying a force per unit width N_x of 2 N/mm for a $[-15, 90, +15]$ laminate in Case A and Case B with *Nlg OFF* and *Nlg ON*, respectively. The predicted displacement w_o is considerable. Case A (Figure 4.49) predicts a linear increase in the displacement along x and y, as predicted by the CLT. In Case B with *Nlg OFF* (Figure 4.50a and b) the displacement is concentrated on the free edge and the predicted w_o is almost double the one predicted on the edges of Case A. As the model neglects the non linear effects of large deformations, it predicts a clearly unreasonable change of the specimen width. In Case B with *Nlg ON* (Figure 4.50c and d) in which the non linear effects of large deformations is considered, more reasonable results are observed.



(a) (b)

Figure 4.49: FEM analysis of an antisymmetric laminate $[-15, 90, +15]$ subjected to boundary conditions and loads showed in Figure 4.48a. *Nlg OFF*. Distribution of the displacement in z direction w_o. (a) Frontal view. (b) Isometric view.

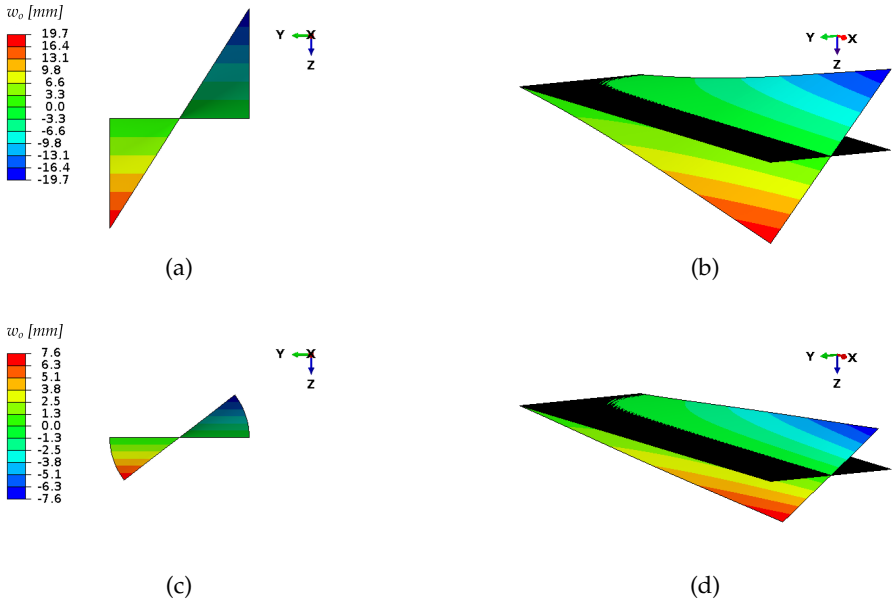


Figure 4.50: FEM analysis of an antisymmetric laminate $[-15, 90, +15]$ subjected to boundary conditions and loads showed in Figure 4.48b. Distribution of the displacement in z direction w_o. (a) *Nlg OFF*. Frontal view. (b) *Nlg OFF*. Isometric view. (c) *Nlg ON*. Frontal view. (d) *Nlg ON*. Isometric view.

In order to compare the results of the simulations of the different laminates the twisting angle ϕ has been calculated.
For Case A as:

$$\phi = arctan(2\,\frac{w_o}{w/2}) \tag{4.71}$$

For Case B with *Nlg OFF* as:

$$\phi = arctan(\frac{w_o}{w/2}) \tag{4.72}$$

For Case B with *Nlg ON* as:

$$\phi = arcsin(\frac{w_o}{w/2}) \tag{4.73}$$

where $w/2$ is 12.5 mm, that is half of the initial width of the specimen.

It is possible to derive the twisting angle ϕ of the antisymmetric laminates analyzed also from a pure analytical calculation based on CLT.

Remembering the definition of the curvature κ_{xy}:

$$\kappa_{xy} = -2\,\frac{\partial^2 w_o}{\partial x\,\partial y} \tag{4.74}$$

it is possible to determine the twisting angle ϕ at any point in the middle surface of the laminate by integration. w_o is the displacement in z direction and $tan(\phi) = \partial w_o/\partial y$. Since κ_{xy} is constant, $tan(\phi)$ is constant along y and increases linearly in x. Considering the reference system in Figure 4.51, in which the origin corresponds to the center of the laminate that is fixed, ϕ can be calculated as:

$$\phi = arctan\left(-\frac{\kappa_{xy}\ x}{2}\right) \tag{4.75}$$

The expected twisting angle ϕ at the edges of the laminates can be calculated at the coordinate corresponding to the edges, in the considered case $x = 45\ mm$, as the laminate length is $90\ mm$.

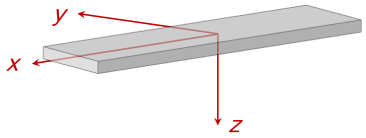


Figure 4.51: Reference system of the laminate.

Figure 4.52 shows the predicted twisting angle ϕ versus the applied force N_x, from CLT with Equation 4.75 and from the numerical simulation with Equations 4.71, 4.72 and 4.73. Laminates with stacking sequences $[-15,90,+15]$, $[-30,90,+30]$, $[-45,90,+45]$, $[-60,90,+60]$ and $[-75,90,+75]$ with width $w = 25\ mm$, length $l = 90\ mm$ and thickness $t = 0.54\ mm$ are considered.

Overall, the angles predicted are quite high and there is no large difference between the stacking sequences considered. The results of the numerical simulation in Case A predict twisting angles similar to the analytical solution with CLT. This is expected, as the finite element simulation assumes the Kirchhoff hypothesis to connect the layers of the composite layup as the CLT. The finite element simulation in Case B with *Nlg OFF*, predicts lower twisting angles than the CLT, and Case B with *Nlg ON* predicts even lower angles. The difference is higher for laminates with lower angle ϑ.

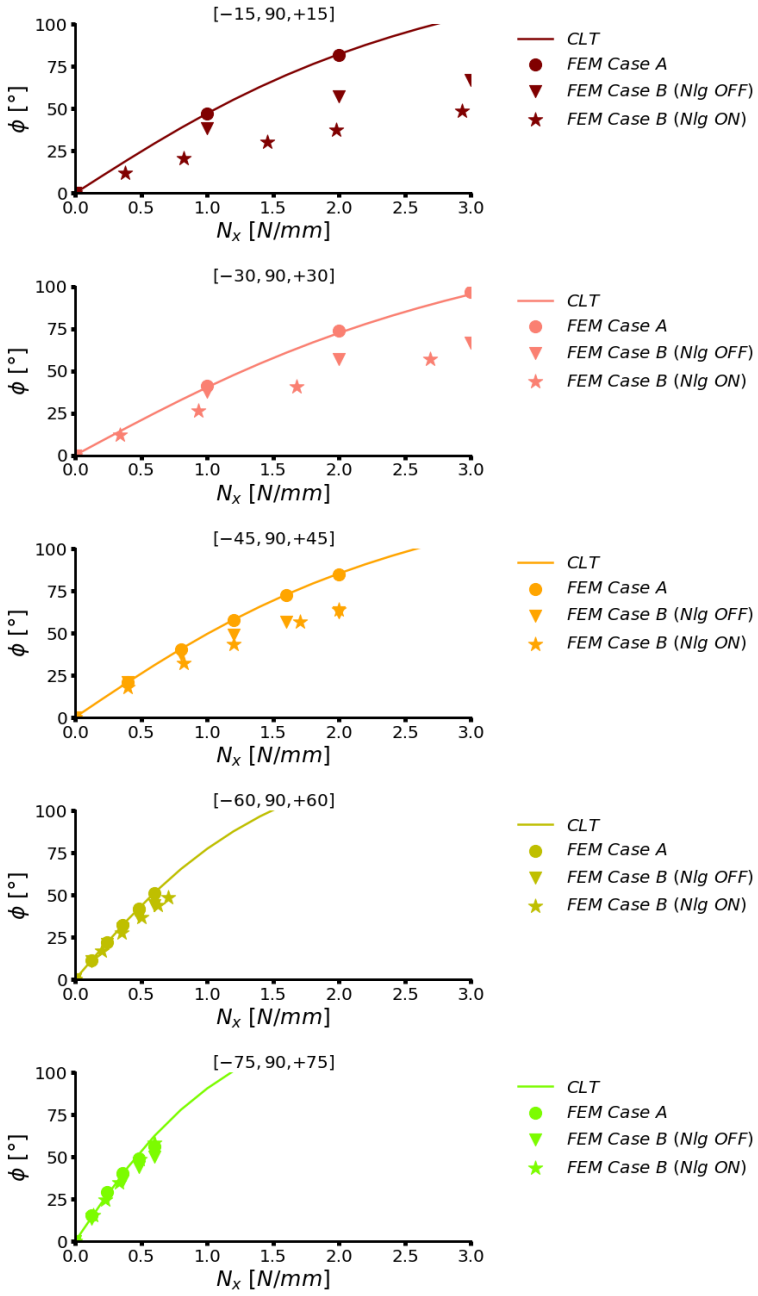
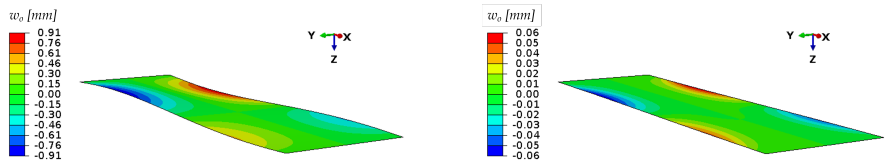


Figure 4.52: Expected twisting angle ϕ versus N_x, calculated from CLT with Equation 4.75 and from the numerical simulation with Equations 4.71 (FEM Case A), 4.72 (FEM Case B (*Nlg OFF*) and 4.73 (FEM Case B (*Nlg ON*) for laminates with stacking sequences $[-15, 90, +15]$, $[-30, 90, +30]$, $[-45, 90, +45]$, $[-60, 90, +60]$ and $[-75, 90, +75]$.

The simulation of Case C (Figure 4.48c) allows to predict the torque applied by the specimen if the twisting is hindered. Figure 4.53a and b show the results of the simulation of Case C respectively with *Nlg OFF* and *Nlg ON* on a $[-15, 90, +15]$ laminate subjected to a force per unit width $N_x = 4\ N/mm$. Both the edges of the specimen remain aligned in the plane $x - y$, but the central part of the specimen tends to twist. If the non linear effects of large deformation is not considered the displacements in z direction of the central part of the specimen are higher. The reaction momentum in x direction on the external side has been extracted. The values of the momentum extracted for the two simulations resulted to be equivalent, thus only one value will be showed for the simulation of the different laminates.



(a) (b)

Figure 4.53: FEM analysis of an antisymmetric laminate $[-15, 90, +15]$ subjected to boundary conditions and loads showed in Figure 4.48c. Isometric view. Distribution of the displacements in z direction w_o. (a) *Nlg OFF*. (b) *Nlg ON*.

To reproduce with CLT the same conditions as finite element simulation of Case C, in which the specimen is kept aligned along the $x - y$ plane, the momentum M_{xy} needed to have the curvature $\kappa_{xy} = 0$ can be calculated from the inverse of the ABD matrix (Equation 4.44). Considering a force applied in x direction N_x and a momentum M_{xy} in an antisymmetric laminate:

$$\begin{bmatrix} \varepsilon_x^o \\ \varepsilon_y^o \\ \gamma_{xy}^o \\ \kappa_x \\ \kappa_y \\ \kappa_{xy} \end{bmatrix} = \begin{bmatrix} A'_{11} & A'_{12} & 0 & 0 & 0 & B'_{16} \\ A'_{21} & A'_{22} & 0 & 0 & 0 & B'_{26} \\ 0 & 0 & A'_{66} & B'_{61} & B'_{62} & 0 \\ 0 & 0 & B'_{16} & D'_{11} & D'_{12} & 0 \\ 0 & 0 & B'_{26} & D'_{21} & D'_{22} & 0 \\ B'_{61} & B'_{62} & 0 & 0 & 0 & D'_{66} \end{bmatrix} \begin{bmatrix} N_x \\ 0 \\ 0 \\ 0 \\ 0 \\ M_{xy} \end{bmatrix} \tag{4.76}$$

thus,

$$\kappa_{xy} = B'_{61}\ N_x + D'_{66}\ M_{xy} = 0 \tag{4.77}$$

and

$$M_{xy} = -\frac{B'_{61}\ N_x}{D'_{66}} \tag{4.78}$$

M_{xy} is the momentum per unit width, thus the torque Γ can be calculated as:

$$\Gamma = M_{xy}\ w \tag{4.79}$$

where $w = 25\ mm$ is the width of the specimen considered.

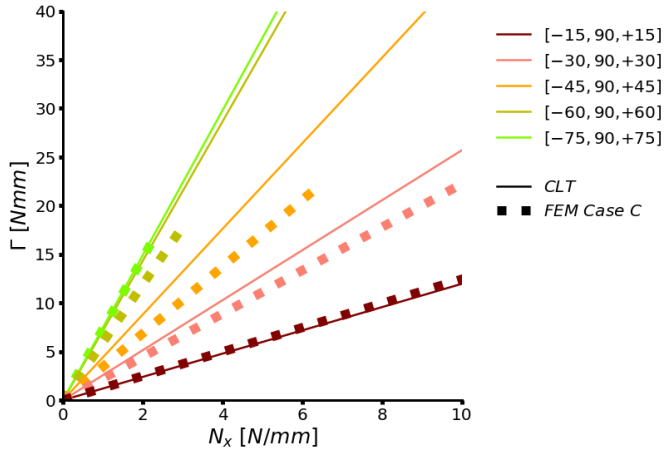


Figure 4.54: Torque Γ versus the applied force N_x, calculated from CLT with Equation 4.79 and from the numerical simulation, Case C, for laminates with stacking sequences $[-15, 90, +15]$, $[-30, 90, +30]$, $[-45, 90, +45]$, $[-60, 90, +60]$ and $[-75, 90, +75]$.

Figure 4.54 shows the expected torque Γ versus the applied force N_x, calculated from CLT with Equation 4.79 and from the numerical simulation, Case C, for the same laminates. Both the torque values calculated by CLT and by FEM increase linearly with the longitudinal force N_x applied and they are higher for laminates with higher angle ϑ. Further considerations of these results in comparison with experimental results will be given in Section 4.6.4.

4.6.3 Experimental

Experimental tests were performed with a setup specifically designed to study the effects of extension-twist coupling. The experimental setup was designed by Polymer Competence Center Leoben and the details of the design cannot be disclosed as they are currently in the patenting process. The clamps are mounted on a Z010 ZwickRoell universal testing machine. One clamp is fixed and works as a standard tensile clamp, the other clamp can operate in two modes:

- *No rotation* mode: in this mode the clamp is aligned with the other clamp and during the tensile test it allows the measurement of the torque Γ which hinders the rotation.
- *Free rotation* mode: in this mode the clamp can rotate around the x axis from $-60°$ to $+60°$ with respect to the zero position and allows the measurement of the twisting angle ϕ of the specimen with an accuracy of half a degree.

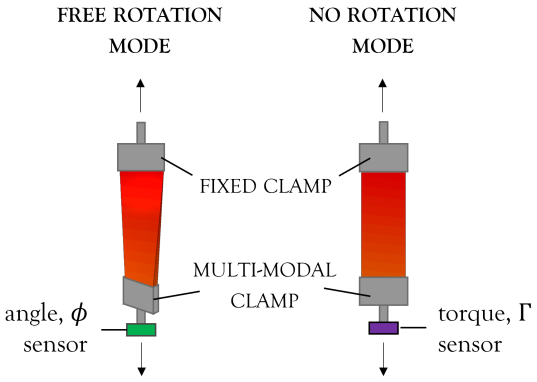


Figure 4.55: Sketch of *free rotation* mode (left) and *no rotation* mode (right) clamp operation.

Figure 4.55 shows a sketch of the two modes of clamp operation. Tests were performed in both modes, under displacement control, using a 10 kN load cell. Tests were carried out in a controlled environment at 23°C and 50% of relative humidity and at strain rate of 0.11 $1/s$. Four to eight specimens per laminate were tested. Strains have been measured locally, with a stereo digital image correlation (DIC) system. The tests were

recorded with two Prosilica GT 6600, Allied Vision Technologies cameras (sensor size 35 mm) and the images analyzed with Mercury^{RT} software. The distance between the cameras and the specimen was about 1 m. The distance between the two cameras was about 0.6 m. The specimens were obtained by cutting sheets produced by vacuum-assisted resin infusion technique described in Section 4.3.2. The stacking sequence of the laminates is $[-\vartheta, 90, +\vartheta]$ with $\vartheta = 15, 30, 45, 60, 75^\circ$. Laminates were produced with fiber-volume fraction $v_f = 0.42 \pm 0.02$. All the specimens have rectangular shape with $w_0 = 25\ mm$, $t_0 = 0.54 \pm 0.03\ mm$ and gauge length $L_0 = 90\ mm$. The specimens show a certain variability in thickness due to the production process employed.

As showed in Section 4.6.2, the stresses in x direction are not homogeneous along the thickness of the laminates, thus the overall behavior of the specimens will be showed in terms of force per unit width, N_x:

$$N_x = \frac{F}{w_0} \tag{4.80}$$

where F is the load measured by the load cell and w_0 the initial width of the specimen. Figure 4.56 shows the $N_x - \varepsilon_x$ curves in x direction for the five different laminates tested with clamps in both *no rotation* and *free rotation* mode. There is no difference in the $N_x - \varepsilon_x$ behavior in x direction for the two modes. Instead, the behavior of the laminates is very different depending on the fiber orientation of the external layers (see Figure 4.57). $[-75, 90, +75]$ laminates achieve strain levels up to about 0.06 and maximum N_x up to about 0.6 N/mm. $[-60, 90, +60]$ laminates achieve strain levels up to about 0.02 and maximum N_x up to about 2 N/mm. $[-45, 90, +45]$ laminates achieve strain levels up to about 0.008 and maximum N_x up to about 4.5 N/mm. $[-30, 90, +30]$ laminates achieve strain levels up to about 0.008 and maximum N_x up to about 12 N/mm. $[-15, 90, +15]$ laminates achieve strain levels up to about 0.006 and maximum N_x up to about 25 N/mm. With the same properties of the lamina, changing only the orientation of the fibers, it is possible to obtain composites with orders of magnitude of difference in their properties.

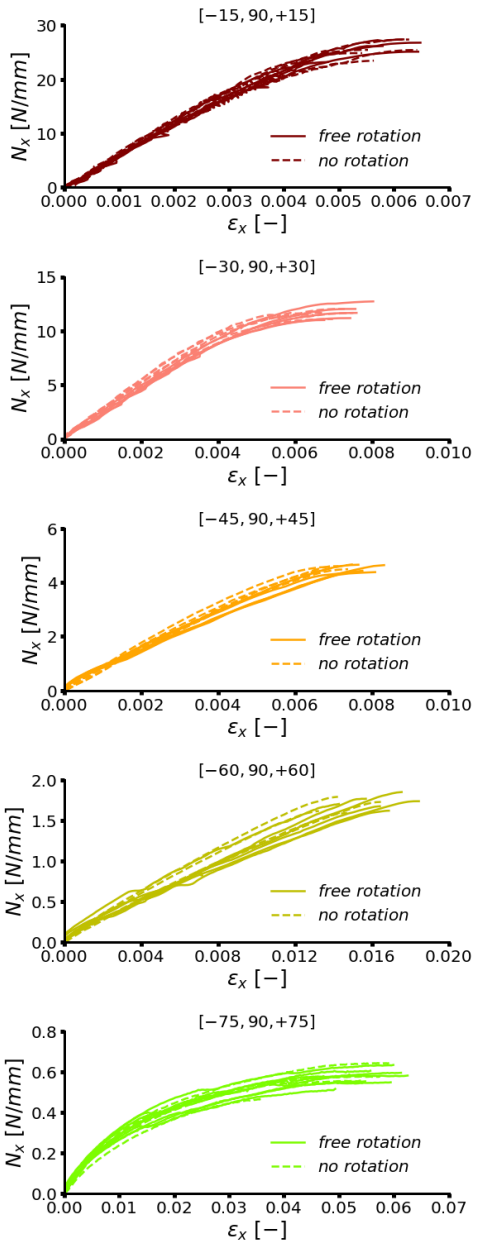


Figure 4.56: $N_x - \varepsilon_x$ curves in x direction for $[-15, 90, +15]$, $[-30, 90, +30]$, $[-45, 90, +45]$, $[-60, 90, +60]$ and $[-75, 90, +75]$ laminates tested with clamps in both *no rotation* and *free rotation* mode. N_x is reported with different ranges in order to allow the assessment of the effect of the clamping mode on the specimen mechanical behavior.

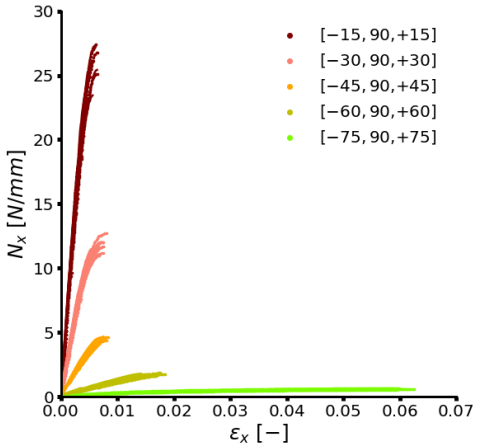
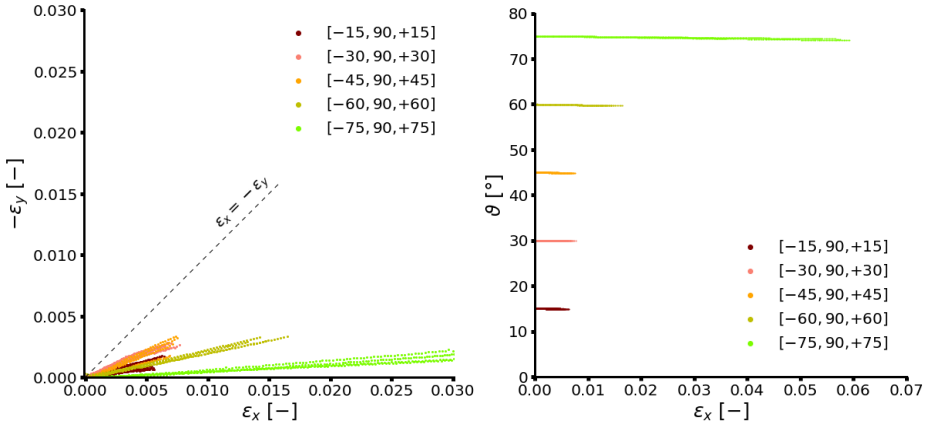


Figure 4.57: Comparison of $N_x - \varepsilon_x$ curves in x direction for $[-15, 90, +15]$, $[-30, 90, +30]$, $[-45, 90, +45]$, $[-60, 90, +60]$ and $[-75, 90, +75]$ laminates.

Differently from the symmetric-balanced laminates (Section 4.5) that showed a large fibers reorientation during loading, these laminates do not show fibers reorientation during loading. The presence of the inner layer oriented at 90° to the loading direction limits the deformations in y direction. In Figure 4.58a the strains in y directions of the specimens tested in *no rotation* mode are showed. $|\varepsilon_y|$ is always more then twice lower than ε_x. Figure 4.58b shows the corresponding variation of the fibers angles ϑ of the external layers versus ε_x calculated according to Equation 4.59. The angle variation in this case is always below 1°, thus can be considered negligible.

Figure 4.59a shows the twisting angle ϕ versus N_x for specimens tested in *free rotation* mode. Figure 4.59b shows the torque Γ versus N_x for specimens tested in *no rotation* mode. Higher twisting angles ϕ are reached with laminates with higher angle ϑ. $[-75, 90, +75]$ laminates reach twisting angles ϕ up to 35°, $[-60, 90, +60]$ laminates reach twisting angles ϕ up to 28°, $[-45, 90, +45]$ laminates reach twisting angles ϕ up to 12°, $[-30, 90, +30]$ laminates reach twisting angles ϕ up to 11° and $[-15, 90, +15]$ laminates reach twisting angles ϕ only up to 5°. On the other hand, higher torques are measured for laminates with lower angle ϑ. In $[-75, 90, +75]$ laminates, only torques Γ up to 13 Nmm are reached, in $[-60, 90, +60]$ laminates, torques Γ up to 25 Nmm are measured, in $[-45, 90, +45]$ laminates, torques Γ up to 43 Nmm are measured, in $[-30, 90, +30]$ laminates, torques Γ up

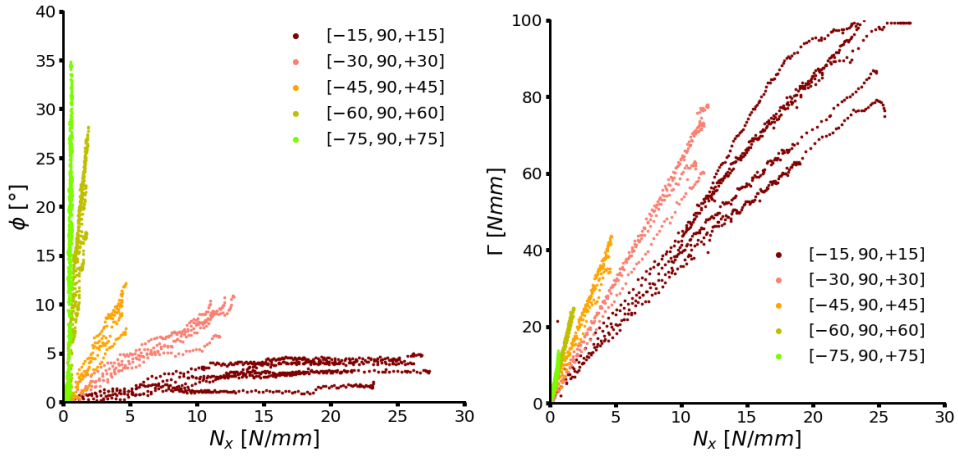


(a) (b)

Figure 4.58: (a) $-\varepsilon_y$ versus ε_x of specimens tested in *no rotation* mode. (b) Fibers angles ϑ of the external layers of the laminates versus ε_x of specimens tested in *no rotation* mode.

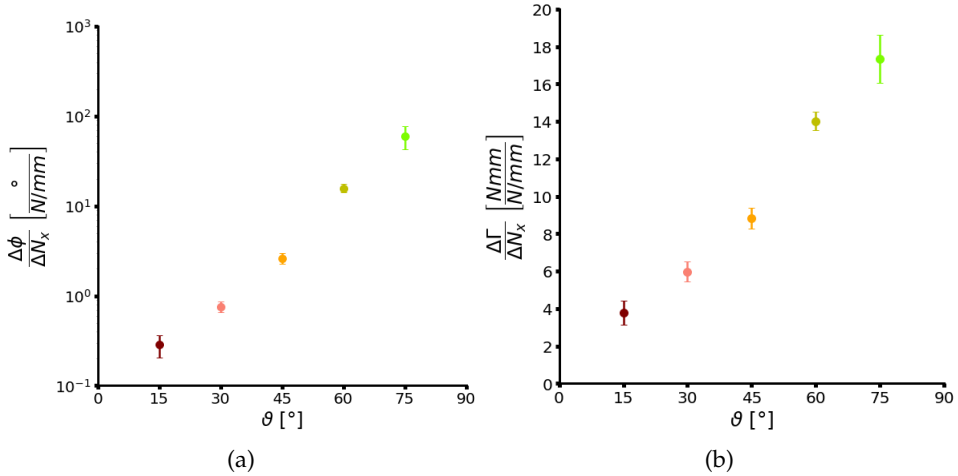
to 80 Nmm are measured and in $[-15, 90, +15]$ laminates, torques Γ up to 100 Nmm are measured. Twisting angle ϕ and torque Γ increase almost linearly with N_x and the slope of these curves is higher for laminates with higher angle ϑ (fibers orientation of the external layers).

In order to evaluate the tendency of the different laminates to twist, or respond in terms of torque if the twisting is prevented, under a given applied force, the average slope of the curves in Figure 4.59a and b has been calculated and it is shows respectively in Figure 4.60a and b versus the fibers orientation of the external layers ϑ (ϕ in $[-15, 90, +15]$ laminates deviate from linearity for high N_x, thus only the part of the curves up to 9 N/mm has been considered). Note that y axis in Figure 4.60a is in logarithmic scale in order to better visualize the differences between laminates. The higher ϑ, the greater the tendency of the laminate to twist or respond in terms of torque if the twisting is prevented, for a given applied force.



(a) (b)

Figure 4.59: (a) Twisting angle ϕ versus N_x of specimens tested in *free rotation* mode. (b) Torque Γ versus N_x of specimens tested in *no rotation* mode.



(a) (b)

Figure 4.60: (a) Slope of ϕ - N_x curves versus ϑ of laminates $[-\vartheta, 90, +\vartheta]$ tested in *free rotation* mode. (b) Slope of Γ - N_x curves versus ϑ of laminates $[-\vartheta, 90, +\vartheta]$ tested in *no rotation* mode.

4.6.4 Model to experimental curves comparison

In order to compare the experimental results with the model predictions, Figure 4.61 shows the N_x - ε_x experimental curves with those predicted by CLT. The values predicted by FEM are consistent with those of the CLT, thus are not reported. The model prediction is comparable with the experimental

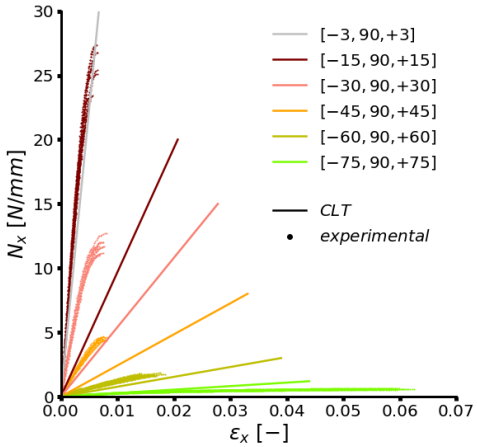
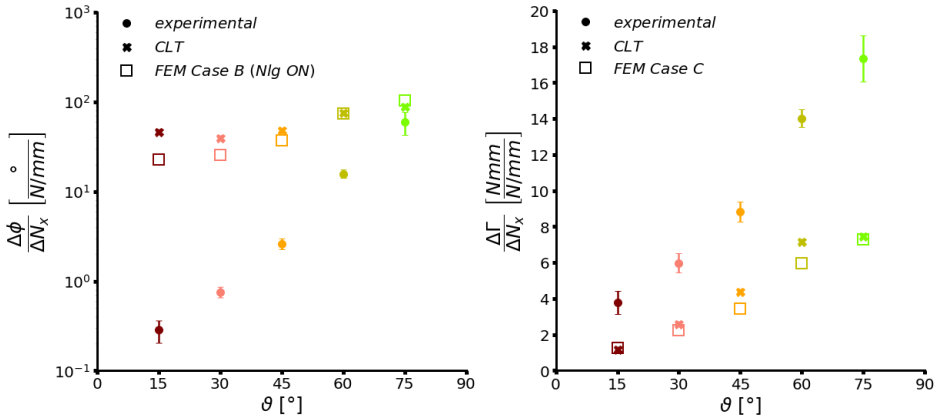


Figure 4.61: N_x - ε_x experimental curves and curves predicted by CLT.

results for $[-75, 90, +75]$ and $[-60, 90, +60]$ laminates, while for laminates with lower ϑ CLT predicts a response softer than the experimental one. The slope of the theoretical curve is lower than the slope of the experimental curve. To give an idea of the difference in stiffness, to reproduce a response similar to the response of the $[-15, 90, +15]$ laminate a theoretical laminate with $\vartheta = 3°$ has to be considered (gray line in Figure 4.61). As previously showed, these laminates do not show fibers reorientation during loading, thus the higher stiffness cannot to be related to fibers reorientation.

To compare the results about the twisting angle ϕ and the torque Γ, the slopes of the theoretical curves ϕ - N_x and Γ - N_x have been evaluated and are compared with the experimental results in Figure 4.62. The theoretical ϕ - N_x curves are not straight lines (See Figure 4.52) but since the difference between experimental results and theoretical prediction is big, a linear fit of the curves is still an acceptable approximation for the sake of comparison.

At the same longitudinal force applied, CLT and FEM predict extremely higher values of twisting angles. Only for $[-75, 90, +75]$ laminates the slopes are of the same order of magnitude, instead, when fibers are more aligned in the longitudinal direction, the predictions differ by orders of



(a) (b)

Figure 4.62: (a) Comparison of theoretical and experimental slope of ϕ - N_x curves for $[-\vartheta, 90, +\vartheta]$ laminates with $\vartheta = 15, 30, 45, 60, 75°$. Note that y axis is in logarithmic scale. (b) Comparison of theoretical and experimental slope of Γ - N_x curves for $[-\vartheta, 90, +\vartheta]$ laminates with $\vartheta = 15, 30, 45, 60, 75°$.

magnitude from the experimental results. On the contrary, the predicted Γ for the same longitudinal force applied, are lower than the measured experimental Γ for all the considered stacking sequences. The difference between experimental results and prediction is smaller, as both values are of the same order of magnitude. The predicted torque is almost half of the measured one.

As expected, this comparison confirms that the assumptions on which Classical Lamination Theory is based, are no longer valid for this highly *anisotropic* flexible composite: both the non-linear elasticity and the presence of interlaminar stresses and strains are no longer negligible.

4.6.5 Summary and conclusive remarks

In this section, the behavior of an antisymmetric laminate subjected to a uniaxial load was showed. The laminate responds with extension in the direction of the load but also with twisting. The type of motion is predictable by the Classical Lamination Theory but the magnitude of twisting is significantly different from the prediction of the CLT, even at small strains. Through this experimental campaign, the potential of this type of composite materials was showed. Given the elasticity, the high

deformability and the low modulus of the matrix they are made of, these composites show effects of load couplings on a macroscopic scale. It has been showed that with the appropriate lamination sequences it is possible to reach twisting angles up to 35° for an applied stress of less than 1.5 MPa. The comparison with the CLT showed the need to carry out further studies in order to be able to predict the behavior of the laminates and be able to design ad hoc systems. This study shows the limitations of simple theories and finite element modeling using the tools normally used for traditional composites.

4.7 Summary and conclusive remarks

In this chapter, the behavior of a new composite material was explored first at small strains and then at large strains. Following the approach typically used for laminates, the four elastic constants necessary for the characterization of the single lamina considered as a *transversely isotropic* material in a plane stress state were estimated. The methods employed to determine these properties have been illustrated, some of which have required special arrangements given the particularity of the composite material under consideration.

In particular, for the characterization of the modulus, due to the huge difference between fiber and matrix properties and therefore the relative properties in the longitudinal and transverse directions of the single lamina, it was necessary to introduce end-tabs with which it was possible to characterize the elastic modulus but it was not possible to achieve laminate failure. Concerning the tests carried out for the characterization of the modulus E_2, it was showed a material behavior linear at small deformations that then deviates from linearity at larger deformations. It was showed how the presence of inhomogeneities, i.e., more or less matrix-rich zones or the presence of stitches, leads to a composite material with significantly different behavior depending on the zone in which it is analyzed.

It was then showed that the simple *spring-in-parallel* model for the prediction of the modulus E_1 in the direction parallel to the fibers is valid also for this type of composites. On the contrary, the behavior of the composite in the direction perpendicular to the fibers is much stiffer than that of traditional composites, and the traditional micromechanical models

normally used, such as the Halpin Tsai model, are not able to predict the behavior of the composite. This stiffness increase can be related to the particular behavior of the elastomeric matrix. In particular, two main reasons can be mentioned. One is the "rubber confinement": if we consider a layer of rubber constrained between two rigid parts, the glass fibers in the present case, the rubber cannot contract during a tensile test as if it were unconstrained and, thus, it responds by acting as a much more rigid material. The second cause of stiffening can be attributed to the reduction in mobility of the rubber molecules that normally occurs when a rubber is filled. The rubber molecules in the proximity of the filler are less mobile so they exhibit stiffer behavior.

Concerning the Poisson's ratio, it has been showed that this type of composites can reach Poisson's ratios greater than two. These values may seem counter intuitive when compared to that of *isotropic* materials but they are more than reasonable if the large difference between the fiber modulus and the matrix modulus and, thus, the properties in the two principal directions of the lamina, is taken into account.

The shear modulus G_{12} showed a behavior similar to that obtained for the determination of the modulus E_2: it is much higher than that predicted by the micromechanical models normally used for the prediction of the behavior of traditional composites.

The investigation of the behavior of symmetric-balanced laminates has showed their highly non-linear behavior. Consequently, we are aware that the characterization of the laminate through the determination of its four material constant at small strains is not sufficient for a complete characterization of the laminate. The characterization at large strains of symmetric-balanced laminates has showed not only the importance of considering other factors such as fibers reorientation but also the importance of effects such as strain softening and residual stresses during loading-unloading cycles that are not normally present in traditional composites. This can lead to a different response of the laminate when stressed the first time or when stressed multiple times.

The following investigation of the extent of the load coupling effects that can be achieved with this type of composite materials was intended to illustrate the potential of this type of materials in different application fields such as flexible robotics or in biomimetic applications, for which objects

capable to show multiple complex deformations even when subjected to simple stimuli are needed. This work is clearly not exhaustive for the complete characterization of these composite materials but it is certainly a starting point from which further studies can be based.

Chapter 5

Conclusions and future developments

This work represents a step ahead in the understanding of the behavior of fiber-reinforced elastomers, FREs. In the first part of the work the crosslinking kinetics of PDMS Sylgard®184 and its influence on the final mechanical properties of the material have been investigated. This work might provide useful information to researcher employing PDMS Sylgard®184 as part of more complex structures. The crosslinking kinetics has been studied following the evolution of two material properties: the heat released during the reaction and the growth of the conservative component of the shear modulus. Through the kinetic model that describes the conversion related to the change in the mechanical properties it was possible to get relevant information fundamental for the production of PDMS items. Given the thermal history applied to the uncured material, the model allowed to predict the time in which the material is processable and the time needed to reach the completion of the reaction. Furthermore, the work showed how the elastic modulus at small strain changes depending on the thermal history applied during crosslinking and proposed an alternative method for the estimation of the elastic modulus at small strains by means of simple swelling measurements which allows the determination of the crosslinking degree to which the modulus is correlated. Swelling measurements are of interest as they can be performed on samples of any shape and dimension and require only a precision weighing scale balance.

In the second part of the work continuous glass fibers - PDMS laminates

have been studied. The typical approach for the production and the characterization of continuous fiber-reinforced composite materials has been employed and their advantages and limitations are discussed. The production method employed in this work is a "lab scale" technology. Of course, further studies could to done to improve this method in order to improve the homogeneity of the composite and the efficiency of the process. A classical approach for the characterization of the composite has been employed with the purpose to identify models to be used in the prediction of its properties. Laminae of GF-PDMS composite have been characterized in order to identify the four independent material constants necessary to describe a transversely isotropic material in a plane state of stress. The four properties have been measured at small strains and models able to predict E_1, E_2 and G_{12} for fiber volume fractions from 0.1 to 0.5 have been proposed.

A topic that has not been taken into consideration in this work is the adhesion between fiber and matrix. The adhesion properties between fiber and matrix can strongly influence the behavior of the composite. Future developments in this direction are fundamental for the full understanding of the behavior of the composite. Fibers bundle or single fibers pull-out tests on similar materials can be found in literature [68]. Studies on fibers modification to improve the adhesion properties are also found in literature [69]. It could be interesting to investigate the correlation between the adhesion and the mechanical properties of the composite.

Furthermore, selected stacking sequences have been characterized up to large strains. The peculiar behavior observed shows the potentiality of these composites. Further studies to fully characterize the behavior of the lamina up to large deformations are certainly necessary. From an experimental point of view, a novel clamping system should be developed to perform tensile tests up to failure for unidirectional elastomeric composites in fibers direction, or different testing procedures could be developed to measure the intra-laminar shear properties. Due to the huge difference in matrix and fiber moduli, a study of the inter-laminar shear properties could be also of great interest in FREs. Symmetric-balanced laminates showed a highly non-linear behavior already from small strains. The non-linear response has been related to a combination of the fibers reorientation during loading, fibers-elastomer interactions and elastomer confinement between stiff fibers.

Further studies are necessary to better understand the relative importance of these factors to the behavior of the composite. A better understanding of these aspects would help in predicting the behavior of FREs. Finally, antisymmetric laminates showed large load coupling effects. The load coupling has been observed and measured, showing the effects of different fibers orientations. The limitation of the classical lamination theory in the prediction of the behavior of these highly anisotropic composites has been clearly showed from the comparison of the model prediction with the experimental results. This study focused mainly on the experimental characterization of the material, while only a preliminary study has been done regarding the modeling of its behavior. The development of a non-linear approach, considering, for example, hyper-elastic models, is certainly necessary to predict the behavior of these composites.

Overall, the present work is a step in the direction of the understanding on the behavior of elastomeric laminates which can be taken as a solid foundation for a deeper characterization of FREs.

Appendix A

Quasi-static tensile tests on Sylgard®184

Quasi-static tensile tests were performed with an INSTRON 5967 universal testing machine equipped with a 2 kN load cell. Tests have been performed under displacement control at nominal strain rate of 0.12 $1/s$, in a controlled environment at 23°C and 50% of relative humidity. Engineering strains ε_x in loading direction have been measured locally, with a digital image correlation (DIC) system. The tensile tests were observed with a UI-5490SE camera and the images analyzed with VIC2D-2009 software.

Tests have been performed on four dumbbell specimens according to Standard BS ISO 37 [70] with length of narrow portion $L_0 = 25\ mm$, width of narrow portion $w_0 = 4\ mm$ and thickness $t_0 = 2\ mm$. PDMS plates 2 mm thick have been produced employing the small square mold 80 mm x 80 mm also employed for the production of the GF-PDMS composite according to the procedure described in Section 4.3.3 without adding the fibers in the mold. Dumbbell specimens have been obtained from the plates with a proper cutting die. Assuming the PDMS incompressible and isotropic, true stress $\sigma_{x\ true}$ and true strain $\varepsilon_{x\ true}$ in loading direction can be calculated as:

$$\begin{aligned} \varepsilon_{x\ true} &= ln(\varepsilon_x + 1) \\ \sigma_{x\ true} &= \frac{F}{w_0\ t_0}\ (\varepsilon_x + 1) \end{aligned} \tag{A.1}$$

where F is the load measured.

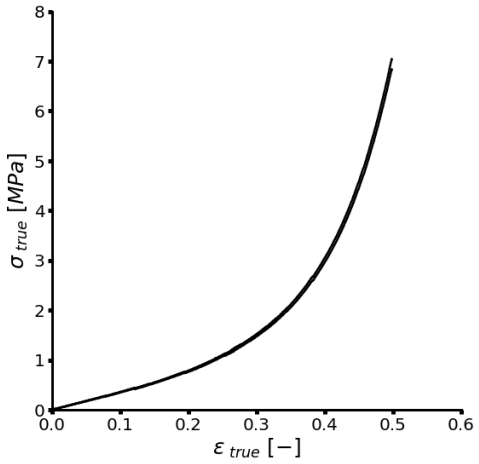


Figure A.1: True stress - strain curves $\sigma_{true} - \varepsilon_{true}$ of the PDMS Sylgard®184 during quasi-static tensile tests.

Figure A.1 shows the true stress - true strain curves $\sigma_{x\ true} - \varepsilon_{x\ true}$ of the tested specimens. The PDMS shows a linear behavior up to $\varepsilon_{x\ true} = 0.1$. The modulus at small strains of the PDMS has been calculated as the slope of the first part the curve up to $\varepsilon_{x\ true} = 0.1$ and was found to be $3.3 \pm 0.2\ MPa$.

Bibliography

[1] R. M. Jones, *Mechanics of Composite Materials*. New York: Taylor & Francis, 2. ed ed., 1999.

[2] J. Reddy, *Mechanics of Laminated Composite Plates and Shells*. USA: CRC PRESS, second ed., 2004.

[3] V. Slesarenko, K. Y. Volokh, J. Aboudi, and S. Rudykh, "Understanding the strength of bioinspired soft composites," *International Journal of Mechanical Sciences*, vol. 131–132, pp. 171–178, Oct. 2017.

[4] H.-J. Kim, S.-H. Song, and S.-H. Ahn, "A turtle-like swimming robot using a smart soft composite (SSC) structure," *Smart Materials and Structures*, vol. 22, no. 1, p. 014007, 2013.

[5] Y. Chen, X. Tan, D. Yan, Z. Zhang, and Y. Gong, "A Composite Fabric-Based Soft Rehabilitation Glove With Soft Joint for Dementia in Parkinson's Disease," *IEEE Journal of Translational Engineering in Health and Medicine*, vol. 8, pp. 1–10, 2020.

[6] Z. Yao, C. Linnenberg, A. Argubi-Wollesen, R. Weidner, and J. P. Wulfsberg, "Biomimetic design of an ultra-compact and light-weight soft muscle glove," *Production Engineering*, vol. 11, pp. 731–743, Dec. 2017.

[7] S.-H. Song, H. Lee, J.-G. Lee, J.-Y. Lee, M. Cho, and S.-H. Ahn, "Design and analysis of a smart soft composite structure for various modes of actuation," *Composites Part B: Engineering*, vol. 95, pp. 155–165, June 2016.

[8] H. Rodrigue, B. Bhandari, M.-W. Han, and S.-H. Ahn, "A shape memory alloy–based soft morphing actuator capable of pure twisting

motion," *Journal of Intelligent Material Systems and Structures*, vol. 26, pp. 1071–1078, June 2015.

[9] H. Rodrigue, W. Wang, B. Bhandari, M.-W. Han, and S.-H. Ahn, "Cross-shaped twisting structure using SMA-based smart soft composite," *International Journal of Precision Engineering and Manufacturing-Green Technology*, vol. 1, pp. 153–156, Apr. 2014.

[10] S.-H. Ahn, K.-T. Lee, H.-J. Kim, R. Wu, J.-S. Kim, and S.-H. Song, "Smart soft composite: An integrated 3D soft morphing structure using bend-twist coupling of anisotropic materials," *International Journal of Precision Engineering and Manufacturing*, vol. 13, pp. 631–634, Apr. 2012.

[11] J. Beter, B. Schrittesser, G. Meier, B. Lechner, M. Mansouri, P. F. Fuchs, and G. Pinter, "The Tension-Twist Coupling Mechanism in Flexible Composites: A Systematic Study Based on Tailored Laminate Structures Using a Novel Test Device," *Polymers*, vol. 12, p. 2780, Dec. 2020.

[12] M. R. Mansouri, P. F. Fuchs, J. C. Criscione, B. Schrittesser, and J. Beter, "The contribution of mechanical interactions to the constitutive modeling of fiber-reinforced elastomers," *European Journal of Mechanics - A/Solids*, vol. 85, p. 104081, Jan. 2021.

[13] S.-y. Luo, T.-w. Chou, and A. Kelly, "Finite deformation of flexible composites," *Proceedings of the Royal Society of London. A. Mathematical and Physical Sciences*, vol. 429, pp. 569–586, June 1990.

[14] T.-W. Chou, "Flexible composites," *Journal of Materials Science*, vol. 24, pp. 761–783, Mar. 1989.

[15] G. Koerner, *Silicones, Chemistry and Technology*. CRC Press, Mar. 1992.

[16] F. Schneider, T. Fellner, J. Wilde, and U. Wallrabe, "Mechanical properties of silicones for MEMS," *Journal of Micromechanics and Microengineering*, vol. 18, p. 065008, June 2008.

[17] F. Schneider, J. Draheim, R. Kamberger, and U. Wallrabe, "Process and material properties of polydimethylsiloxane (PDMS) for Optical MEMS," *Sensors and Actuators A: Physical*, vol. 151, pp. 95–99, Apr. 2009.

[18] A. Villanueva, C. Smith, and S. Priya, "A biomimetic robotic jellyfish (Robojelly) actuated by shape memory alloy composite actuators," *Bioinspiration & Biomimetics*, vol. 6, p. 036004, Aug. 2011.

[19] T. K. Kim, J. K. Kim, and O. C. Jeong, "Measurement of nonlinear mechanical properties of PDMS elastomer," *Microelectronic Engineering*, vol. 88, pp. 1982–1985, Aug. 2011.

[20] A. Colombo, H. Zahedmanesh, D. M. Toner, P. A. Cahill, and C. Lally, "A method to develop mock arteries suitable for cell seeding and in-vitro cell culture experiments," *Journal of the Mechanical Behavior of Biomedical Materials*, vol. 3, pp. 470–477, Aug. 2010.

[21] R. F. Shepherd, F. Ilievski, W. Choi, S. A. Morin, A. A. Stokes, A. D. Mazzeo, X. Chen, M. Wang, and G. M. Whitesides, "Multigait soft robot," *Proceedings of the National Academy of Sciences*, vol. 108, pp. 20400–20403, Dec. 2011.

[22] W. Wang, J.-Y. Lee, H. Rodrigue, S.-H. Song, W.-S. Chu, and S.-H. Ahn, "Locomotion of inchworm-inspired robot made of smart soft composite (SSC)," *Bioinspiration & Biomimetics*, vol. 9, p. 046006, Oct. 2014.

[23] J. S. Kee, D. P. Poenar, P. Neužil, L. Yobaş, and Y. Chen, "Design and fabrication of Poly(dimethylsiloxane) arrayed waveguide grating," *Optics Express*, vol. 18, pp. 21732–21742, Oct. 2010.

[24] D. Corning, "Product information sheet of Sylgard184," 2017.

[25] L. M. Lopez, A. B. Cosgrove, J. P. Hernandez-Ortiz, and T. A. Osswald, "Modeling the vulcanization reaction of silicone rubber," *Polymer Engineering & Science*, vol. 47, no. 5, pp. 675–683, 2007.

[26] A. Harkous, G. Colomines, E. Leroy, P. Mousseau, and R. Deterre, "The kinetic behavior of Liquid Silicone Rubber: A comparison between thermal and rheological approaches based on gel point determination," *Reactive and Functional Polymers*, vol. 101, pp. 20–27, Apr. 2016.

[27] I. D. Johnston, D. K. McCluskey, C. K. L. Tan, and M. C. Tracey, "Mechanical characterization of bulk Sylgard 184 for microfluidics

and microengineering," *Journal of Micromechanics and Microengineering*, vol. 24, no. 3, p. 035017, 2014.

[28] V. Placet and P. Delobelle, "Mechanical properties of bulk polydimethylsiloxane for microfluidics over a large range of frequencies and aging times," *Journal of Micromechanics and Microengineering*, vol. 25, p. 035009, Feb. 2015.

[29] S. Vyazovkin, A. K. Burnham, J. M. Criado, L. A. Pérez-Maqueda, C. Popescu, and N. Sbirrazzuoli, "ICTAC Kinetics Committee recommendations for performing kinetic computations on thermal analysis data," *Thermochimica Acta*, vol. 520, pp. 1–19, June 2011.

[30] R. J. Young and P. A. Lovell, *Introduction to Polymers, Third Edition*. Bosa Roca : CRC Press, 3rd ed ed., 2011.

[31] H. J. Borchardt and F. Daniels, "The Application of Differential Thermal Analysis to the Study of Reaction Kinetics," *Journal of the American Chemical Society*, vol. 79, pp. 41–46, Jan. 1957.

[32] C. W. Macosko, *Rheology: Principles Measurements and Applications*. U.S.A.: Wiley-VCH, 1994.

[33] G. W. H. Höhne, W. F. Hemminger, and H.-J. Flammersheim, *Differential Scanning Calorimetry*. Berlin, Heidelberg: Springer Berlin Heidelberg, 2003.

[34] S. Vyazovkin, K. Chrissafis, M. L. Di Lorenzo, N. Koga, M. Pijolat, B. Roduit, N. Sbirrazzuoli, and J. J. Suñol, "ICTAC Kinetics Committee recommendations for collecting experimental thermal analysis data for kinetic computations," *Thermochimica Acta*, vol. 590, pp. 1–23, Aug. 2014.

[35] J. C. Domínguez, M. V. Alonso, M. Oliet, E. Rojo, and F. Rodríguez, "Kinetic study of a phenolic-novolac resin curing process by rheological and DSC analysis," *Thermochimica Acta*, vol. 498, pp. 39–44, Jan. 2010.

[36] M. R. Kamal and S. Sourour, "Kinetics and thermal characterization of thermoset cure," *Polymer Engineering & Science*, vol. 13, no. 1, pp. 59–64, 1973.

[37] I.-K. Hong and S. Lee, "Cure kinetics and modeling the reaction of silicone rubber," *Journal of Industrial and Engineering Chemistry*, vol. 19, pp. 42–47, Jan. 2013.

[38] Q. Zhang, B. Song, S. Wang, L. Xu, and S. Liu, "Cure kinetics analysis and simulation of silicone adhesives," *2009 International Conference on Electronic Packaging Technology and High Density Packaging, ICEPT-HDP 2009*, Aug. 2009.

[39] U. W. Gedde, *Polymer Physics*. London, UK: Springer Netherlands, 1995.

[40] P. J. Flory, *Principles of Polymer Chemistry*. Ithaca, NY: Cornell University Press, 1953.

[41] J. N. Lee, C. Park, and G. M. Whitesides, "Solvent Compatibility of Poly(dimethylsiloxane)-Based Microfluidic Devices," *Analytical Chemistry*, vol. 75, pp. 6544–6554, Dec. 2003.

[42] A. M. Bueche, "Interaction of polydimethylsiloxanes with swelling agents," *Journal of Polymer Science*, vol. 15, no. 79, pp. 97–103, 1955.

[43] C. Robert, A. Crespy, S. Bastide, J.-M. Lopez-Cuesta, S. Kerboeuf, C. Artigue, and E. Grard, "Rheological properties of silicon polymer networks: The influence of the crosslink density," *Journal of Applied Polymer Science*, vol. 87, no. 7, pp. 1152–1160, 2003.

[44] P. J. Flory and J. Rehner, "Statistical Mechanics of Cross-Linked Polymer Networks II. Swelling," *The Journal of Chemical Physics*, vol. 11, pp. 521–526, Nov. 1943.

[45] N. Rennar and W. Oppermann, "Swelling behavior and mechanical properties of endlinked poly (dimethylsiloxane) networks and randomly crosslinked polyisoprene networks," *Colloid and Polymer Science*, vol. 270, pp. 527–536, June 1992.

[46] Sigma-Aldrich, "Toluene Safety Data Sheet," 2014.

[47] J. Brandrup, E. H. Immergut, and E. A. Grulke, eds., *Polymer Handbook*. New York: Wiley, 4th ed ed., 1999.

[48] A. C. C. Esteves, J. Brokken-Zijp, J. Laven, H. P. Huinink, N. J. W. Reuvers, M. P. Van, and G. de With, "Influence of cross-linker concentration on the cross-linking of PDMS and the network structures formed," *Polymer*, vol. 50, pp. 3955–3966, July 2009.

[49] J. E. Sheats, C. E. Carraher, C. U. Pittman, M. Zeldin, and B. M. Culbertson, "Inorganic and Organometallic Polymers — An Overview," in *Metal-Containing Polymeric Materials* (C. U. Pittman, C. E. Carraher, M. Zeldin, J. E. Sheats, and B. M. Culbertson, eds.), pp. 3–37, Boston, MA: Springer US, 1990.

[50] T. Bardelli, C. Marano, and F. Briatico Vangosa, "Polydimethylsiloxane crosslinking kinetics: A systematic study on Sylgard184 comparing rheological and thermal approaches," *Journal of Applied Polymer Science*, p. e51013, 2021.

[51] M. Liu, J. Sun, and Q. Chen, "Influences of heating temperature on mechanical properties of polydimethylsiloxane," *Sensors and Actuators A: Physical*, vol. 151, pp. 42–45, Apr. 2009.

[52] T. Bardelli, C. Marano, and F. Briatico Vangosa, "Influence of curing thermal history on cross-linking degree of a polydimethylsiloxane: Swelling and mechanical analyses," *Express Polymer Letters*, vol. 16, pp. 924–932, 2022.

[53] S. Vyazovkin, "On the phenomenon of variable activation energy for condensed phase reactions," *New Journal of Chemistry*, vol. 24, pp. 913–917, Jan. 2000.

[54] Y. Akagi, J. P. Gong, U.-i. Chung, and T. Sakai, "Transition between Phantom and Affine Network Model Observed in Polymer Gels with Controlled Network Structure," *Macromolecules*, vol. 46, pp. 1035–1040, Feb. 2013.

[55] R. B. Adusumalli, K. C. Venkateshan, C. Kunchi, and S. R. Vadlamani, "Tensile testing of single fibres," *Procedia Structural Integrity*, vol. 14, pp. 150–157, Jan. 2019.

[56] C28 Committee, "Test Method for Tensile Strength and Youngs Modulus of Fibers," tech. rep., ASTM International, 2020.

[57] B. M. Lempriere, "Poisson's ratio in orthotropic materials.," *AIAA Journal*, vol. 6, pp. 2226–2227, Nov. 1968.

[58] J. C. Halpin, "Effects Of Environmental Factors On Composite Materials:," tech. rep., Defense Technical Information Center, Fort Belvoir, VA, June 1969.

[59] A. Goren and C. Atas, "Manufacturing of polymer matrix composites using vacuum assisted resin infusion molding," *Archives of Materials Science and Engineering*, vol. 34, no. Vol. 234, nr 2, pp. 117–120, 2008.

[60] D30 Committee, "D3039/D3039M - 17: Test Method for Tensile Properties of Polymer Matrix Composite Materials," tech. rep., ASTM International, 2017.

[61] L. Pini, "Geometry optimization for biaxial testing of polydimethylsiloxane SYLGARD(R) 184 and finite element modelling," Master's thesis, Politecnico di Milano, 2020.

[62] A. N. Gent, "Engineering with Rubber," in *Engineering with Rubber* (A. N. Gent, ed.), pp. I–XVIII, Hanser, Jan. 2012.

[63] D20 Committee, "ASTM D638: Standard Test Method for Tensile Properties of Plastics," tech. rep., ASTM International, 1999.

[64] D30 Committee, "Test Method for In-Plane Shear Response of Polymer Matrix Composite Materials by Tensile Test of a 45 Laminate," tech. rep., ASTM International, 2018.

[65] D. Magni, "Mechanical characterization of fibres-reinforced elastomers: A study on continuous glass fibres-Sylgard 184 composite," Master's thesis, Politecnico di Milano, 2022.

[66] P. H. Petit, "A Simplified Method of Determining the Inplane Shear Stress-Strain Response of Unidirectional Composites," in *Composite Materials: Testing and Design* (S. Yurenka, ed.), pp. 83–83–11, 100 Barr Harbor Drive, PO Box C700, West Conshohocken, PA 19428-2959: ASTM International, Jan. 1969.

[67] J. Diani, B. Fayolle, and P. Gilormini, "A review on the Mullins effect," *European Polymer Journal*, vol. 45, pp. 601–612, Mar. 2009.

[68] J. Beter, B. Schrittesser, B. Maroh, E. Sarlin, P. F. Fuchs, and G. Pinter, "Comparison and Impact of Different Fiber Debond Techniques on Fiber Reinforced Flexible Composites," *Polymers*, vol. 12, p. 472, Feb. 2020.

[69] J. Beter, B. Maroh, B. Schrittesser, I. Mühlbacher, T. Griesser, S. Schlögl, P. F. Fuchs, and G. Pinter, "Tailored Interfaces in Fiber-Reinforced Elastomers: A Surface Treatment Study on Optimized Load Coupling via the Modified Fiber Bundle Debond Technique," *Polymers*, vol. 13, p. 36, Jan. 2021.

[70] I. Committee, "ISO 37: Rubber, vulcanized or thermoplastic — Determination of tensile stress-strain properties," tech. rep., ISO International, 2017.